$HH \to b\bar{b}b\bar{b}$ or How I Learned to Stop Worrying and Love the QCD Background

Sean Gasiorowski

A dissertation
submitted in partial fulfillment of the
requirements for the degree of

Doctor of Philosophy

University of Washington

2021

Reading Committee:

Anna Goussiou, Chair

Jason Detwiler

Shih-Chieh Hsu

David Kaplan

Henry Lubatti

Thomas Quinn

Gordon Watts

Program Authorized to Offer Degree:
Physics

University of Washington

Abstract

$HH \rightarrow b\bar{b}b\bar{b}$ or How I Learned to Stop Worrying and Love the QCD Background

Sean Gasiorowski

Chair of the Supervisory Committee:
Professor Anna Goussiou
Physics

Insert abstract here

TABLE OF CONTENTS

LIST OF FIGURES

GLOSSARY

ARGUMENT: replacement text which customizes a LaTeX macro for each particular usage.

ACKNOWLEDGMENTS

As anyone who has written a Ph.D. thesis will probably tell you, it's been a journey. We laughed, we cried, we bled occasionally (though nothing too serious). A pandemic happened, I learned how to make sourdough (see the appendix for more details). I learned how to ski, discovered a love for hiking, and ate large amounts of cheese. The list of people who I have met and shared deep and memorable experiences with is long – I fear to list you all here in case I miss someone! – but please do know that I treasure you. This is the beauty and tragedy of doing a Ph.D. half in Seattle, half at CERN: it allows you to build strong friendships with a large group of people, and then scatters you all across the globe. So to the Seattle friends, to the CERN friends, to the friends from undergrad, and high school, and even earlier, and to everyone in between, thank you for being a part of my life, and I hope to see you soon.

Of course, a thank you to my family for their continuing support, vacationing adventures, and for trying their best to learn physics along with me (my dad re: ATLAS – "This is pretty complicated isn't it?").

And finally a huge thank you to my group: Anna, for your guidance and support, and for always caring about me as a person in addition to me as a physicist. And Jana, for guidance and support, of course, but also for looking at/giving comments on almost literally every single one of my talks (even if you didn't always get my jokes).

DEDICATION

To family, both given and found

Chapter 1

THE STANDARD MODEL OF PARTICLE PHYSICS

"I may be bad, but I'm perfectly good at it" - Rihanna re: the Standard Model (SM), or so I've been told

The Standard Model of Particle Physics (SM) is a monumental historical achievement, providing a formalism with which one may describe everything from the physics of everyday experience to the physics that is studied at very high energies at the Large Hadron Collider (Chapter 3). In this chapter, we will provide a brief overview of the pieces that go into the construction of such a model. The primary focus of this thesis is searches for pair production of Higgs bosons decaying to four b-quarks. Consequently, we will pay particular attention to the relevant pieces of the Higgs Mechanism, as well as the theory behind searches at a hadronic collider.

1.1 Introduction: Particles and Fields

What is a particle? The Standard Model describes a set of fundamental, point-like, objects (shown in Figure SM FIGURE). These objects have distinguishing characteristics (e.g., mass and spin). These objects interact in very specific ways. The set of objects and their interactions result in a set of observable effects, and these effects are the basis of a field of experimental physics.

The effects of these objects and their interactions are familiar as fundamental forces: electromagnetism (photons, electrons), the strong interaction (quarks, gluons), the weak interaction (neutrinos, W and Z bosons). Gravity is not described in this model, as the

weakest, with effects most relevant on much larger distance scales than the rest. However, the description of these other three is powerful – verifying and searching for cracks in this description is a large effort, and the topic of this thesis.

The formalism for describing these particles and their interactions is that of quantum field theory. Classical field theory is most familiar in the context of, e.g., electromagnetism – an electric field exists in some region of space, and a charged point-particle experiences a force characterized by the charge of the point-particle and the magnitude of the field at the location of the point-particle in spacetime. The same language translates to quantum field theory. Here, particles are described in terms of quantum fields in some region of spacetime. These fields have associated charges which describe the forces they experience when interacting with other quantum fields. Most familiar is electric charge – however this applies to e.g., the strong interaction as well, where quantum fields have an associated *color charge* describing behavior under the strong force.

Particles are observed to behave in different ways under different forces. These behaviors respect certain *symmetries*, which are most naturally described in the language of group theory. The respective fields, charges, and generators of these symmetry groups are the basic pieces of the SM Lagrangian, which describes the full dynamics of the theory. In the following, we will build up the basic components of this Lagrangian.

1.2 Quantum Electrodynamics

Classical electrodynamics is familiar to the general physics audience: electric ($\vec{E}$) and magnetic ($\vec{B}$) fields are used to describe behavior of particles with charge q moving with velocity $\vec{v}$, with forces described as $\vec{F} = q\vec{E} + q\vec{v} \times \vec{B}$. Hints at some more fundamental properties of electric and magnetic fields come via a simple thought experiment: in a frame of reference moving along with the particle at velocity $\vec{v}$, the particle would appear to be standing still, and therefore have no magnetic force exerted. Therefore a *relativistic* formulation of the theory is required. This is most easily accomplished with a repackaging: the fundamental objects are

no longer classical fields but the electric and magnetic *potentials*: ϕ and $\vec{A}$ respectively, with

$$\vec{E} = -\boldsymbol{\nabla}\phi - \frac{\partial \vec{A}}{\partial t} \tag{1.1}$$

$$\vec{B} = \boldsymbol{\nabla} \times \vec{A} \tag{1.2}$$

It is then natural to fully repackage into a relativistic *four-vector*: $A_\mu = (\phi, \vec{A})$. Considering $\partial^\mu = (\frac{\partial}{\partial t}, \boldsymbol{\nabla})$, the x components of these above two equations become: *TODO: Check signs and units!! Add Jackson reference?*

$$E_x = -\frac{\partial \phi}{\partial x} + \frac{\partial A_x}{\partial t} = (\partial^0 A^1 - \partial^1 A^0) \tag{1.3}$$

$$B_x = \frac{\partial A_z}{\partial y} - \frac{\partial A_y}{\partial z} = (\partial^2 A^3 - \partial^3 A^2) \tag{1.4}$$

This is naturally suggestive of a second rank, antisymmetric tensor to describe both the electric and magnetic fields (the *field strength tensor*), defined as:

$$F^{\alpha\beta} = \partial^\alpha A^\beta - \partial^\beta A^\alpha \tag{1.5}$$

Defining a four-current as $J_\mu = (q, \vec{J})$, with q standard electric charge, $\vec{J}$ standard electric current, conservation of charge may be expressed via the continuity equation

$$\partial_\mu J^\mu = 0 \tag{1.6}$$

and all of classical electromagnetism may be packaged into the Lagrangian density:

$$\mathcal{L} = -\frac{1}{4}F_{\mu\nu}F^{\mu\nu} - J^\mu A_\mu. \tag{1.7}$$

This gets us partway to our goal, but is entirely classical - the description is of classical fields and point charges, not of quantum fields and particles. To reframe this, let us go back to the zoomed out view of the particles of the Standard Model. Two of the most familiar objects associated with electromagnetism are electrons: spin-1/2 particles with charge e, mass m, and photons: massless spin-1 particles which are the "pieces" of electromagnetic radiation.

We know that electrons experience electromagnetic interactions with other objects. Given this, and the fact that such interactions must be transmitted *somehow* between e.g. two

electrons, it seems natural that these interactions are facilitated by electromagnetic radiation. More specifically, we may think of photons as *mediators* of the electromagnetic force. It follows, then, that a description of electromagnetism on the level of particles must involve a description of both the "source" particles (e.g. electrons), the mediators (photons), and their interactions. Further, this description must be (1) relativistic and (2) consistent with the classically derived dynamics described above.

The beginnings of a relativistic description of spin-1/2 particles is due to Paul Dirac, with the famous Dirac equation:

$$(i\gamma^\mu \partial_\mu - m)\psi = 0 \tag{1.8}$$

where ∂_μ is as defined above, ψ is a Dirac *spinor*, i.e. a four-component wavefunction, m is the mass of the particle, and γ^μ are the Dirac gamma matrices, which define the algebraic structure of the theory.

TODO: Add some stuff about the conjugate?

The Dirac equation is the dynamical equation for spin-1/2, but we'd like to express these dynamics via a Lagrangian density. Further, to have a relativistic description, we'd like to have this be density be Lorentz invariant. These constraints lead to a Lagrangian of the form

$$\mathcal{L} = \bar{\psi}(i\gamma^\mu \partial_\mu - m)\psi \tag{1.9}$$

where the Euler-Lagrange equation exactly recovers the Dirac equation.

The question now becomes how to marry the two Lagrangian descriptions that we have developed. Returning for a moment to classical electrodynamics, we know that the Hamiltonian for a charged particle in an electromagnetic field is described by

$$H = \frac{1}{2m}(\vec{p} - q\vec{A})^2 + q\phi. \tag{1.10}$$

Comparing this to the Hamiltonian for a free particle, we see that the modifications required are $\vec{p} \to \vec{p} - q\vec{A}$ and $E \to E - q\phi$. Using the canonical quantization trick of identifying $\vec{p}$ with operator $-i\boldsymbol{\nabla}$ and E with operator $i\frac{\partial}{\partial t}$, this identification becomes

$$i\partial_\mu \to i\partial_\mu - qA_\mu \tag{1.11}$$

Allowing for the naive substitution in the Dirac Lagrangian *TODO: Source term?*:

$$\mathcal{L} = \bar{\psi}(i\gamma^\mu(\partial_\mu + iqA_\mu) - m)\psi - \frac{1}{4}F_{\mu\nu}F^{\mu\nu}. \tag{1.12}$$

Setting $q = e$ here (as appropriate for the case of an electron), and defining $D_\mu \equiv \partial_\mu + ieA_\mu$, this may then be written in the form

$$\mathcal{L} = \bar{\psi}(i\gamma^\mu D_\mu - m)\psi - \frac{1}{4}F_{\mu\nu}F^{\mu\nu}. \tag{1.13}$$

which is exactly the quantum electrodynamics Lagrangian.

We have swept a few things under the rug here, however. Recall that the general form of a Lagrangian is conventionally $\mathcal{L} = T - V$, where T is the kinetic term, and thus ought to contain a derivative with respect to time (c.f. the standard $\frac{1}{2}m\frac{\partial x}{\partial t}$ familiar from basic kinematics). More particularly, given the definition of conjugate momentum as $\partial\mathcal{L}/\partial\dot{q}$ for $\mathcal{L}(q, \dot{q}, t)$ and $\dot{q} = \frac{\partial q}{\partial t}$, any field q which has no time derivative in the Lagrangian has 0 conjugate momentum, and thus no dynamics.

Looking at this final form, there is an easily identifiable kinetic term for the spinor fields (just applying the D_μ operator). However trying to identify something similar for the A fields, one comes up short – the antisymmetric nature of $F^{\mu\nu}$ term means that there is no time derivative applied to A^0.

What does this mean? A^μ is a four component object, but it would appear that only three of the components have dynamics: we have too many degrees of freedom in the theory. This is the principle behind *gauge symmetry* – an extra constraint on A^μ (a *gauge condition*) must be defined such that a unique A^μ defines the theory and satisfies the condition. However, we are free to choose this extra condition – the physics content of the theory should be independent of this choice (that is, it should be *gauge invariant*).

To ground this a bit, let us return to basic electric and magnetic fields. These are physical quantities that can be measured, and are defined in terms of potentials as

$$\vec{E} = -\boldsymbol{\nabla}\phi - \frac{\partial\vec{A}}{\partial t} \tag{1.14}$$

$$\vec{B} = \boldsymbol{\nabla} \times \vec{A}. \tag{1.15}$$

It is easy to show, for any scalar function λ, that $\boldsymbol{\nabla} \times \boldsymbol{\nabla}\lambda = 0$. This implies that the physical $\vec{B}$ field is invariant under the transformation $\vec{A} \to \vec{A} + \boldsymbol{\nabla}\lambda$ for any scalar function λ.

Under the same transformation of $\vec{A}$, the electric field $\vec{E}$ becomes $-\boldsymbol{\nabla}\phi - \frac{\partial \vec{A}}{\partial t} - \frac{\partial \boldsymbol{\nabla}\lambda}{\partial t} = -\boldsymbol{\nabla}\left(\phi + \frac{\partial \lambda}{\partial t}\right) - \frac{\partial \vec{A}}{\partial t}$, such that, for the $\vec{E}$ field to be unchanged, we must additionally apply the transformation $\phi \to \phi - \frac{\partial \lambda}{\partial t}$.

TODO: Check signs here too! This is set of transformations to the potentials that leave the physical degrees of freedom invariant is expressed in our four vector notation naturally as

$$A_\mu \to A_\mu - \partial_\mu \lambda \tag{1.16}$$

where $A_\mu = (\phi, -\vec{A})$ with our sign convention. It should be noted that this function λ is an arbitrary function of *local* spacetime, and thus expresses invariance of the physics content under a local transformation.

Let us return to the Lagrangian for QED. In particular, focusing on the free Dirac piece

$$\mathcal{L} = \bar{\psi}(i\gamma^\mu \partial_\mu - m)\psi \tag{1.17}$$

we note that if we apply a local transformation of the form $\psi \to e^{iq\lambda(x)}\psi$ (and correspondingly $\bar{\psi} \to \bar{\psi}e^{-iq\lambda(x)}$, by definition), the Lagrangian becomes

$$\bar{\psi}e^{-iq\lambda(x)}(i\gamma^\mu \partial_\mu - m)e^{iq\lambda(x)}\psi = \bar{\psi}e^{-iq\lambda(x)}(i\gamma^\mu \partial_\mu)e^{iq\lambda(x)}\psi - m\bar{\psi}\psi. \tag{1.18}$$

As $\partial_\mu(e^{iq\lambda(x)}\psi) = iqe^{iq\lambda(x)}(\partial_\mu \lambda(x))\psi + e^{iq\lambda(x)}\partial_\mu \psi$, this becomes

$$\bar{\psi}(i\gamma^\mu(\partial_\mu + iq\partial_\mu \lambda(x)) - m)\psi. \tag{1.19}$$

Thus, the free Dirac Lagrangian on its own is not invariant under this transformation. We may note, however, that on interaction with an electromagntic field, as described above, this transformed Lagrangian may be packaged as:

$$\bar{\psi}(i\gamma^\mu(\partial_\mu + iq\partial_\mu \lambda(x) + iqA_\mu) - m)\psi = \bar{\psi}(i\gamma^\mu(\partial_\mu + iq(A_\mu + \partial_\mu \lambda(x)) - m)\psi. \tag{1.20}$$

since by the arguments above, the physics content of the Lagrangian is invariant under the transformation $A_\mu \to A_\mu - \partial_\mu \lambda$, we may directly make this transformation, and remove this

extra $\partial_\mu \lambda(x)$ term. It is straightforward to verify that the $\frac{1}{4} F_{\mu\nu} F^{\mu\nu}$ term is invariant under this same transformation of A_μ, so we may say that the QED Lagrangian is invariant under local transformations of the form $\psi \rightarrow e^{iq\lambda(x)} \psi$.

These arguments illuminate some important concepts which will serve us well going forward. First, while we have remained grounded in the "familiar" physics of electromagnetism for the above, arguments of the "top down" variety would lead us to the exact same conclusions. That is, suppose we wanted to construct a theory of spin-1/2 particles that was invariant under local transformations of the form $\psi \rightarrow e^{iq\lambda(x)} \psi$. More broadly, we could say that we desire this theory to be invariant under local $U(1)$ transformations, where $U(1)$ is exactly this group, under multiplication, of complex numbers with absolute value 1. By very similar arguments as above, we would see that, to achieve invariance, this theory would necessitate an additional degree of freedom, A_μ, with the exact properties that are familiar to us from electrodynamics. These arguments based on symmetries are extremely powerful in building theories with a less familiar grounding, as we will see in the following.

Second, we defined this quantity $D_\mu \equiv \partial_\mu + ieA_\mu$ above, seemingly as a matter of notational convenience. However, from the latter set of arguments, such a packaging takes on a new power: by explicitly including this gauge field A_μ which transforms in such a way as to keep invariance under a given transformation, the invariance is immediately more manifest. That is, to pose the $U(1)$ invariance in a more zoomed out way, under the transformation $\psi \rightarrow e^{iq\lambda(x)} \psi$, while

$$\bar{\psi} \partial_\mu \psi \rightarrow \bar{\psi} (\partial_\mu + iq\partial_\mu \lambda(x)) \psi \tag{1.21}$$

with the extra term that gets canceled out by the gauge transformation of A_μ,

$$\bar{\psi} D_\mu \psi \rightarrow \bar{\psi} D_\mu \psi \tag{1.22}$$

where this transformation is already folded in. This repackaging, called a *gauge covariant derivative* is much more immediately expressive of the symmetries of the theory.

Finally, to emphasize how fundamental these gauge symmetries are to the corresponding theory, let us examine the additional term needed for $U(1)$ invariance, $q\bar{\psi} \gamma^\mu A_\mu \psi$. While a

first principles examination of Feynman rules is beyond the scope of this thesis, it is powerful to note that this is expressive of a QED vertex: the $U(1)$ invariance of the theory and the interaction between photons and electrons are inextricably tied together.

1.3   An Aside on Group Theory

TODO: word on exponential representation? Quantum electrodynamics is very familiar and well covered, and provides (both historically and in this thesis) a nice bridge between "standard" physics and the language of symmetries and quantum field theory. However, now that we are acquainted with the language, we may set up to dive a bit deeper. To begin, let us look again at the $U(1)$ group that is so fundamental to QED. We have expressed this via a set of transformations on our Dirac spinor objects, ψ, of the form $e^{iq\lambda(x)}$. Note that such transformations, though they are local (i.e. a function of spacetime) are purely *phase* transformations. Relatedly, $U(1)$ is an Abelian group, meaning that group elements commute.

To set up language to generalize beyond $U(1)$, note that we may equivalently write $U(1)$ elements as $e^{ig\vec{\alpha}(x)\cdot\vec{T}}$, $\vec{\alpha}(x)$ and $\vec{T}$ and are vectors in the space of *generators* of the group, with each $\alpha^a(x)$ an associated scalar function to generator t^a, and g is some scalar strength parameter. Of course this is a bit silly for $U(1)$, which has a single generator, and thus reduces to the transformation we discussed above. However, this becomes much more useful for groups of higher degree, with more generators and degrees of freedom.

To discuss these groups in a bit more detail, note that $U(n)$ is the unitary group of degree n, and corresponds to the group of $n \times n$ unitary matrices (that is, $U^\dagger U = UU^\dagger = 1$). Given that group elements are $n \times n$, this means that there are n^2 degrees of freedom: n^2 generators are needed to characterize the group.

For $U(1)$, this is all consistent with what we have said above – the group of 1×1 unitary matrices have a single generator, and the phases we identify above clearly satisfy unitarity. Note that these degrees of freedom for the gauge group also characterize the number of gauge bosons we need to satisfy the local symmetry: for $U(1)$, we need one gauge boson, the photon.

Of relevance for the Standard Model are also the special unitary groups $SU(n)$. These

are defined similarly to the unitary groups, with the additional requirement that group elements have determinant 1. This extra constraint removes 1 degree of freedom: groups are characterized by $n^2 - 1$ generators.

In particular, we will examine the groups $SU(2)$ in the context of the weak interaction, with an associated $2^2 - 1 = 3$ gauge bosons (cf. the $W^\pm$ and Z bosons), and $SU(3)$, with an associated $3^2 - 1 = 8$ gauge bosons (cf. gluons of different flavors). Note that these groups are non-Abelian (2×2 or 3×3 matrices do not, in general, commute), leading to a variety of complications. However, both of these theories feature interactions with spin-1/2 particles, with transformations of a very similar form: $\psi \to e^{ig\vec{\alpha}(x)\cdot\vec{T}}\psi$, and the general framing of the arguments for QED will serve us well in the following.

1.4 Quantum Chromodynamics

In some sense, the simplest extension the development of QED is quantum chromodynamics (QCD). QCD is a theory in which, once the basic dynamics are framed (a non-trivial task!) the group structure becomes apparent. The quark model, developed by Murray Gell-Mann and George Zweig *TODO: cite*, provided the fundamental particles involved in the theory, and had great success in explaining the expanding zoo of experimentally observed hadronic states.

Some puzzles were still apparent – the Δ^{++} baryon, e.g., is composed of three up quarks, u, with aligned spins. As quarks are fermions, such a state should not be allowed by the Pauli exclusion principle. The existence of such a state in nature implies the existence of another quantum number, and a triplet of values, called *color charge* was proposed by Oscar Greenburg *TODO: cite*. With these pieces in place, the structure becomes more apparent, as elucidated by Han and Nambu *TODO: cite: https://digital.library.unt.edu/ark:/67531/metadc1031342/m1/6/*.

Let us reason our way to the symmetries using color charge. Experimentally, we know that there is this triplet of color charge values r, g, b (the "plus" values, cf. electric charge) and correspondingly anti-color charge $\bar{r}, \bar{g}, \bar{b}$ (the "minus" values). Supposing that the force behind QCD (the *strong force*) is, similar to QED, interactions between fermions mediated by gauge bosons (quarks and gluons respectively), we can start to line up the pieces.

What color charge does a gluon have? Similarly to electric charge, we may associate particles with color charge, anti-particles with anti-color charge. Notably, free particles observed experimentally are colorless (have no color charge). Thus, in order for charge to be conserved throughout such processes, this already implies that there are charged gluons. Further, examining color flow diagrams such as *TODO: insert*, it is apparent first that a gluon has not one but two associated color charges and second that these two must be one color charge and one anti-color charge.

Counting up the available types of gluons, then, we come up with nine. Six of mixed color type: $r\bar{b}, r\bar{g}, b\bar{r}, b\bar{g}, g\bar{b}$, and $g\bar{r}$, and three of same color type: $r\bar{r}$, $g\bar{g}$, and $b\bar{b}$. In practice, however, these latter three are a bit redundant: all express a colorless gluon, which, if we could observe this as a free particle, would be indistinguishable from each other. The *color singlet* state is then a mix of these, $\frac{1}{\sqrt{3}}(r\bar{r} + g\bar{g} + b\bar{b})$, leaving two unclaimed degrees of freedom, which may be satisfied by the linearly independent combinations $\frac{1}{\sqrt{2}}(r\bar{r} - g\bar{g})$ and $\frac{1}{\sqrt{6}}(r\bar{r} + g\bar{g} - 2b\bar{b})$.

We thus have an octet of color states plus a colorless singlet state. If this colorless singlet state existed, however, we would be able to observe it, not only via interactions with quarks, but as a free particle. Since do not observe this in nature, this restricts us to 8 gluons. The simplest group with a corresponding 8 generators is $SU(3)$. Under the assumption that $SU(3)$ is the local gauge symmetry of the strong interaction, we may proceed in a similar way as we did for QED. The gauge transformation is $\psi \to e^{ig_S \vec{\alpha}(x) \cdot \vec{T}}\psi$, where $\vec{T}$ is an eight component vector of the generators of $SU(3)$, often expressed via the Gell-Mann matrices, λ^a, as $t^a = \frac{1}{2}\lambda^a$, and the spinor ψ represents the fields corresponding to quarks.

This $SU(3)$ symmetry exactly expresses the color structure elucidated above – the Gell-Mann matrices are an equivalent presentation of the color combinations described above. Proceeding by analogy to QED, gauge invariance is achieved by introducing eight new degrees of freedom, G_μ^a, which are the gauge fields corresponding to the gluons, with the gauge covariant derivative then analogously taking the form $D_\mu \equiv \partial_\mu + ig_S G_\mu^a t^a$.

Recall from the QED derivation that the field strength tensor, $F^{\mu\nu}$ is a rank two antisym-

metric tensor which is manifestly gauge invariant and which describes the physical dynamics of the A_μ field. We would like to analogously define a term for the gluon fields. Repackaging this QED tensor, it is apparent that

$$[D_\mu, D_\nu] = D_\mu D_\nu - D_\nu D_\mu \tag{1.23}$$

$$= (\partial_\mu + iqA_\mu)(\partial_\nu + iqA_\nu) - (\partial_\nu + iqA_\nu)(\partial_\mu + iqA_\mu) \tag{1.24}$$

$$= \partial_\mu \partial_\nu + iq\partial_\mu A_\nu + iqA_\mu \partial_\nu + (iq)^2 A_\mu A_\nu - (\partial_\nu \partial_\mu + iq\partial_\nu A_\mu + iqA_\nu \partial_\mu + (iq)^2 A_\nu A_\mu) \tag{1.25}$$

$$= iq(\partial_\mu A_\nu - \partial_\nu A_\mu) + (iq)^2 (A_\mu A_\nu - A_\nu A_\mu) \tag{1.26}$$

$$= iq(\partial_\mu A_\nu - \partial_\nu A_\mu) + (iq)^2 [A_\mu, A_\nu]. \tag{1.27}$$

We proceed through this derivation to highlight that, in the specific case of QED, with its Abelian $U(1)$ gauge symmetry, the field commutator vanishes, leaving exactly the definition of $F_{\mu\nu}$ as described above, i.e.,

$$F_{\mu\nu} = \frac{1}{iq}[D_\mu, D_\nu]. \tag{1.28}$$

We may proceed to define an analagous field strength term for G_μ^a in a similar way:

$$G_{\mu\nu} = \frac{1}{ig_S}[D_\mu, D_\nu] \tag{1.29}$$

This has an extremely nice correspondence, but is complicated by the non-Abelian nature of $SU(3)$, with

$$G_{\mu\nu} = \partial_\mu(G_\nu^a t^a) - \partial_\nu(G_\mu^a t^a) + ig_s[G_\mu^a t^a, G_\nu^a t^a]. \tag{1.30}$$

in which the field commutator term is non-zero. In particular (since each term is summing over a, so we may relabel) as

$$[G_\mu^a t^a, G_\nu^b t^b] = [t^a, t^b] G_\mu^a G_\nu^b \tag{1.31}$$

and as $[t^a, t^b] = if^{abc}t^c$ for the Gell-Mann matrices, where f^{abc} are the structure constants of

$SU(3)$, we have

$$G_{\mu\nu} = \partial_\mu(G_\nu^a t^a) - \partial_\nu(G_\mu^a t^a) - g_s f^{abc} t^c G_\mu^a G_\nu^b \tag{1.32}$$

$$= t^a(\partial_\mu G_\nu^a - \partial_\nu G_\mu^a - f^{bca} G_\mu^b G_\nu^c) \tag{1.33}$$

$$= t^a G_{\mu\nu}^a \tag{1.34}$$

for $G_{\mu\nu}^a = \partial_\mu G_\nu^a - \partial_\nu G_\mu^a - f^{abc} G_\mu^b G_\nu^c$.

This gives the component of the field strength corresponding to a particular gauge field a, where the first two terms have the familiar form of the QED field strength, while the last term is new, and explicitly related to the group structure via the f^{abc} constants. In terms of the physics content of the theory, this latter term gives rise to a gluon *self-interaction*, a distinguishing feature of QCD.

Similarly as in QED, a Lorentz invariant combination of field strength tensors may be made as $G_{\mu\nu}G^{\mu\nu}$. However, this is not manifestly gauge invariant. Under a gauge transformation U, the covariant derivative behaves as $D^\mu \to U D^\mu U^{-1}$, corresponding to $G^{\mu\nu} \to U G^{\mu\nu} U^{-1}$. The cyclic property of the trace thus ensures the gauge invariance of $\mathrm{tr}(G_{\mu\nu}G^{\mu\nu})$, which we will write as $G_{\mu\nu}^a G_a^{\mu\nu}$ with the implied sum over generators a.

Packaging up the theory, it is tempting to copy the form of the QED Lagrangian, with the identifications we have made above:

$$\mathcal{L} = \bar{\psi}(i\gamma^\mu D_\mu - m)\psi - \frac{1}{4}G_{\mu\nu}^a G_a^{\mu\nu}. \tag{1.35}$$

However this is not quite correct due to the $SU(3)$ nature of the theory. In terms of the physics, the Dirac fields ψ have associated color charge, which must interact appropriately with the G_μ fields. Mathematically, the generators t^a are 3×3 matrices, while the ψ are four component spinors. Adding a color index to the Dirac fields, i.e., ψ_i where i runs over the three color charges, and similarly indexing the generators t_{ij}^a, we may then express the $SU(3)$ gauge covariant derivative component-wise as

$$(D_\mu)_{ij} = \partial_\mu \delta_{ij} + i g_S G_\mu^a t_{ij}^a \tag{1.36}$$

where δ_{ij} is the Kronecker delta, as ∂_μ does not participate in the $SU(3)$ structure.

The Lagrangian then becomes

$$\mathcal{L} = \bar{\psi}_i(i(\gamma^\mu D_\mu)_{ij} - m\delta_{ij})\psi_j - \frac{1}{4}G^a_{\mu\nu}G^{\mu\nu}_a. \tag{1.37}$$

and we have constructed QCD.

1.5 The Weak Interaction

One of the first theories of the weak interaction was from Enrico Fermi *TODO: cite*, in an effort to explain beta decay, a process in which an electron or positron is emitted from an atomic nucleus, resulting in the conversion of a neutron to a proton or proton to a neutron respectively. Fermi's hypothesis was of a direct interaction between four fermions. However, in the advent of QED, it is natural to wonder if a theory of based on mediator particles and gauge symmetries applies to the weak force as well. The modern formulation of such a theory is due to Sheldon Glashow, Steven Weinberg, and Abdus Salam *TODO: cite*, and is what we will describe in the following.

Considering emission of an electron, Fermi's theory involves an initial state neutron that transitions to a proton with the emission of an electron and a neutrino. Schematically *TODO: include figure*. This transition gives a hint that something slightly more complicated is happening than in QED: there is an apparent mixing between particle types.

Now, with the assumption there are mediators for such an interaction, we further know from beta decay and charge conservation that there must be at least two such degrees of freedom: e.g. one that decays to an electron and neutrino (W^-) and one that decays to a positron and neutrino (W^+). *TODO: Motivation for Z boson - grab Thomson 15.1.2.*

This leads to three degrees of freedom for the gauge symmetry of the weak interactions, so we thus need a theory which is locally invariant under transformations of a group with three generators. The simplest such choice is $SU(2)$. We may follow a very similar prescription as for QED and QCD: $SU(2)$ has three generators, which implies the existence of three gauge bosons, call them W^k_μ. The gauge transformation may be expressed as $\psi \to e^{ig_W \vec{\alpha}(x)\cdot\vec{T}}\psi$, where

in this case the generators are for $SU(2)$, which may be written in terms of the familiar Pauli matrices: $\vec{T} = \frac{1}{2}\vec{\sigma}$. The structure constants for $SU(2)$ are the antisymmetric Levi-Civita tensor, so the corresponding gauge covariant derivative is $D_\mu \equiv \partial_\mu + ig_W W_\mu^k t^k$, and the field strength tensor is $W_{\mu\nu}^k = \partial_\mu W_\nu^k - \partial_\nu W_\mu^k - \epsilon^{ijk} W_\mu^k W_\nu^k$.

The corresponding Lagrangian would thus be

$$\mathcal{L} = \bar{\psi}_i(i(\gamma^\mu D_\mu)_{ij} - m\delta_{ij})\psi_j - \frac{1}{4}W_{\mu\nu}^k W_k^{\mu\nu} \tag{1.38}$$

where indices i and j run over $SU(2)$ charges.

On considering some of the details, the universe unfortunately turns out to be a bit more complicated. However, this still provides a useful starting place for elucidating the theory of weak interactions. First off, let us consider the particle content, namely, what do the Dirac fields correspond to? This is still a theory of fermionic interactions with gauge bosons. However, we might notice that the fermion content of this theory is both a) broader than QCD, as we know experimentally (cf. beta decay) that both quarks and leptons (e.g. electrons) participate in the weak interaction and b) this fermion content seemingly has a large overlap with QED. In terms of the gauge bosons, we know that at both W^+ and W^- are electrically charged – this means that we expect some interaction of the weak theory with electromagnetism.

However, before diving deeper into this apparent connection between the weak interaction and QED, let us focus on the gauge symmetry. In QCD, the $SU(3)$ content of the theory is expressed via a contraction of color indices – the theory allows for transitions between quarks of one color and quarks of another. Thinking similarly in terms of $SU(2)$ transitions, the beta decay example is already fruitful – there is a transition between an electron and its corresponding neutrino, as well as between two types of quark. In particular, for the case of neutron (with quark content udd) and proton (with quark content udu), the weak interaction provides for a transtion from down to up quark.

Such $SU(2)$ dynamics are described via a quantity called *weak isospin*, denoted I_W with third component $I_W^{(3)}$, and can be thought of in a very similar way as color charge in QCD

(i.e. as the charge corresponding to the weak interaction). Since $SU(2)$ is 2×2, there are two such charge states for the fermions, denoted as $I_W^{(3)} = \pm\frac{1}{2}$. This means that the bosons must have $I_W = 1$ such that, by sign convention corresponding to electric charge, the W^+ boson has $I_W^{(3)} = +1$, the Z boson has $I_W^{(3)} = 0$, and the W^- boson has $I_W^{(3)} = -1$.

From conservation of electric charge, this means that transitions involving a $W^{\pm}$ are between particles that differ by ± 1 in both weak isospin $I_W^{(3)}$ and electric charge. We may thus line up all such doublets as:

$$\begin{pmatrix} \nu_e \\ e^- \end{pmatrix}, \begin{pmatrix} \nu_\mu \\ \mu^- \end{pmatrix}, \begin{pmatrix} \nu_\tau \\ \tau^- \end{pmatrix}, \begin{pmatrix} u \\ d' \end{pmatrix}, \begin{pmatrix} c \\ s' \end{pmatrix}, \begin{pmatrix} t \\ b' \end{pmatrix} \tag{1.39}$$

with the top corresponding to the lower weak isospin and electric charge particles, and the lower quark entries (d', etc) corresponding to the weak quark eigenstates (which are related to the mass eigenstates by the CKM matrix *TODO: more detail*). Similar doublets may be constructed for the corresponding anti-particles.

The fundamental structuring of these transitions around both electric and weak charge is again indicative of a natural connection. However, nature is again a bit more complicated than we have described. This is because the weak interaction is a *chiral* theory. For massless particles, chirality is the same as the perhaps more intuitive *helicity*. This describes the relationship between a particle's spin and momentum: if the spin vector points in the same direction as the momentum vector, helicity is positive (the particle is "right-handed"), and if the two point in opposite directions, the helicity is negative (the particle is "left-handed"). More concretely:

$$H = \frac{\vec{s} \cdot \vec{p}}{|\vec{s} \cdot \vec{p}|}. \tag{1.40}$$

For massive particles, this generalizes a bit – in the language of Dirac fermions that we have developed, we define projection operators

$$P_R = \frac{1}{2}(1 + \gamma^5) \quad \text{and} \quad P_L = \frac{1}{2}(1 - \gamma^5) \tag{1.41}$$

for right and left-handed chiralities respectively – acting on a Dirac field with such operators projects the field onto the corresponding chiral state.

Experimentally, this pops up via parity violation and the famous $V - A$ theory *TODO: more detail?*. For the scope of this thesis, it is sufficient to say that the weak interaction is only observed to take place for left-handed particles (and correspondingly, right-handed anti-particles). We therefore modify the theory stated above by projecting all fermions participating in the weak interaction onto respective chiral states – in particular, the $SU(2)$ gauge symmetry only acts on left-handed particles and right-handed anti-particles. We therefore modify the theory appropriately, denoting the chiral projected gauge symmetry as $SU(2)_L$, and similarly for the Dirac fields. In particular, the weak isospin doublets listed above must now be left-handed:

$$\begin{pmatrix} \nu_e \\ e^- \end{pmatrix}_L, \begin{pmatrix} \nu_\mu \\ \mu^- \end{pmatrix}_L, \begin{pmatrix} \nu_\tau \\ \tau^- \end{pmatrix}_L, \begin{pmatrix} u \\ d' \end{pmatrix}_L, \begin{pmatrix} c \\ s' \end{pmatrix}_L, \begin{pmatrix} t \\ b' \end{pmatrix}_L \tag{1.42}$$

and right-handed particle states are placed in singlets and assigned 0 charge under $SU(2)_L$ ($I_W = I_W^{(3)} = 0$).

With all of these assignments, let us revisit our guess at the form of the weak interaction Lagrangian. First, dwelling on the kinetic term $\bar{\psi}_i(i(\gamma^\mu D_\mu)_{ij}\psi_j$, we note that the assigning of left-handed fermions to isospin doublets and right-handed fermions to isospin singlets allows us to remove explicit $SU(2)$ indices by treating these as the fundamental objects, that is, for a single *generation* of fermions, we may write:

$$\bar{Q}i\gamma^\mu D_\mu Q + \bar{u}i\gamma^\mu D_\mu u + \bar{d}i\gamma^\mu D_\mu d + \bar{L}i\gamma^\mu D_\mu L + \bar{e}i\gamma^\mu D_\mu e \tag{1.43}$$

for left-handed doublets Q and L for quarks and electron fields respectively and right handed singlets u and d for up and down quark fields and e for electrons.

More concisely, and summing over the three generations of fermions, we may write

$$\sum_f \bar{f}i\gamma^\mu D_\mu f \tag{1.44}$$

where the f are understood to run over the fermion chiral doublets and singlets as above.

This then leaves our Lagrangian as

$$\mathcal{L} = \sum_f \bar{f} i \gamma^\mu D_\mu f - \frac{1}{4} W^k_{\mu\nu} W^{\mu\nu}_k \tag{1.45}$$

$$= \sum_f \bar{f} \gamma^\mu (i\partial_\mu - \frac{1}{2} g_W W^k_\mu \sigma_k) f - \frac{1}{4} W^k_{\mu\nu} W^{\mu\nu}_k, \tag{1.46}$$

where we have expanded the covariant derivative for clarity. You may note that we have dropped the mass term in the equation above – we will discuss this in detail in just a moment.

TODO: Add in stuff about physical bosons

First, however, we return to the above comment about fermion content – we neglected to include the sum over fermions in our QED derivation for simplicity. However, all of the fermions considered in the discussion of the weak interaction have an electric charge (except for the neutrinos). It would be nice to repackage the theory into a coherent *electroweak* theory. This is fairly straightforward when considering the gauge approach – from the discussion above we should expect the electroweak gauge group to be something like $SU(2) \times U(1)$, with four corresponding gauge bosons. Consider a gauge theory with group $SU(2)_L \times U(1)_Y$ – that is, the same weak interaction as discussed previously, but a new $U(1)_Y$ gauge group for electromagnetism, with transformations defined as

$$\psi \to e^{ig'\frac{Y}{2}\lambda(x)} \psi \tag{1.47}$$

with *weak hypercharge* Y.

Similarly to our discussion of QED, we may write the $U(1)_Y$ gauge field as B_μ, and interactions with the Dirac fields take the form $g'\frac{Y}{2}\gamma^\mu B_\mu \psi$. The relationship between this hypercharge and new B_μ field and classical electrodynamics is not so obvious – however it is convenient to parametrize as

$$\begin{pmatrix} A_\mu \\ Z_\mu \end{pmatrix} = \begin{pmatrix} \cos\theta_W & \sin\theta_W \\ -\sin\theta_W & \cos\theta_W \end{pmatrix} \begin{pmatrix} B_\mu \\ W^3_\mu \end{pmatrix} \tag{1.48}$$

where A_μ and Z_μ are the physical fields, and we pick W^3_μ as the neutral weak boson.

Note that in the $SU(2)_L \times U(1)_Y$ theory, the Lagrangian must be invariant under all of the local gauge transformations. In particular, this means that the hypercharge must be the same for fermion fields in each weak doublet to preserve $U(1)_Y$ invariance. This gives insight into the relation between the charges of $SU(2)_L \times U(1)_Y$ and electric charge. In particular we know that the hypercharge, Y, of e^- ($I_W^{(3)} = -\frac{1}{2}$) and ν_e ($I_W^{(3)} = +\frac{1}{2}$) is the same.

Supposing that $Y = \alpha I_W^{(3)} + \beta Q$ *TODO: why this form?*, we must have $-\alpha\frac{1}{2} - \beta = \alpha\frac{1}{2} \implies \beta = -\alpha$. Therefore, choosing an overall scaling from convention,

$$Y = 2(Q - I_W^{(3)}). \tag{1.49}$$

TODO: Weinberg things

1.6 The Higgs Potential and the SM

In the above, we have neglected a discussion of masses. However there are several things to sort out here. In the first place, we know experimentally that the weak interactions occur over very short ranges at low energies (e.g., why Fermi's effective four fermion interaction was such a good description). This is consistent with massive $W^\pm$ and Z bosons (and indeed, this is seen experimentally). However, requiring local gauge invariance forbids mass terms in the Lagrangian. In the simple $U(1)$ QED example, such a term would have the form $\frac{1}{2}m_\gamma^2 A_\mu A^\mu$, which is not invariant under the transformation $A_\mu \to A_\mu - \partial_\mu \lambda$, and similar arguments hold for gauge bosons in the electroweak theory and QCD.

Similar issues are encountered with fermions – in the electroweak theory above, the gauge symmetries are separated into left and right haned chirality via doublet and singlet states. This means that a mass term would need to be separated as well. Such a term would have the form:

$$m\bar{f}f = m(\bar{f}_L + \bar{f}_R)(f_L + f_R) \tag{1.50}$$

$$= m(\bar{f}_L f_L + \bar{f}_L f_R + \bar{f}_R f_L + \bar{f}_R f_R) \tag{1.51}$$

$$= m(\bar{f}_L f_R + \bar{f}_R f_L) \tag{1.52}$$

where we have used that $f_{L,R} = P_{L,R}f$, $\bar{f}_{L,R} = \bar{f}P_{R,L}$, and $P_R P_L = P_L P_R = 0$. As left and right-handed particles transform differently under $SU(2)_L$, this is manifestly not gauge invariant.

The question then becomes: how do we include particle masses while preserving the gauge properties of our theory? The answer, due to Higgs, Englert *TODO: cite*, comes via the Higgs mechanism, which we will describe in the following. In particular, we focus first on generating masses for the electroweak gauge bosons.

Consider adding two complex scalar fields ϕ^+ and ϕ^0 to the Standard Model embedded in a weak isospin doublet ϕ. We may write the doublet as

$$\phi = \begin{pmatrix} \phi^+ \\ \phi^0 \end{pmatrix} = \frac{1}{\sqrt{2}} \begin{pmatrix} \phi_1 + i\phi_2 \\ \phi_3 + i\phi_4 \end{pmatrix} \tag{1.53}$$

where we explicitly note the four available degrees of freedom.

The Lagrangian for such a doublet takes the form

$$\mathcal{L} = (\partial_\mu \phi)^\dagger (\partial^\mu \phi) - V(\phi) \tag{1.54}$$

where V is the corresponding potential. Considering the particular form

$$V(\phi) = \mu^2 \phi^\dagger \phi + \lambda (\phi^\dagger \phi)^2 \tag{1.55}$$

we may notice that this has some interesting properties. Considering, as illustration, a similar potential for a real scalar field, $\mu^2 \chi^2 + \lambda \chi^4$, taking the derivative and setting it equal to 0 yields extrema when $\chi = 0$ and $(\mu^2 + 2\lambda\chi^2) = 0 \implies \chi^2 = -\frac{\mu^2}{2\lambda}$. For $\mu^2 > 0$, there is a unique minimum at $\chi = 0$, and for $\mu^2 < 0$ there are degenerate minima at $\chi = \pm\sqrt{-\frac{\mu^2}{2\lambda}}$. Note that we take $\lambda > 0$, otherwise the only minima in the theory are trivial.

The same simple calculus for the complex Higgs doublet above yields degenerate minima for $\mu^2 < 0$ at

$$\phi^\dagger \phi = \frac{1}{2}(\phi_1^2 + \phi_2^2 + \phi_3^2 + \phi_4^2) = \frac{v}{2} = -\frac{\mu^2}{2\lambda} \tag{1.56}$$

However, though there is this degenerate set of minima, there can only be a single *physical* vacuum state (we say that the symmetry is *spontaneously broken*). Without loss of generality,

we may align our axes such that the physical vacuum state is at

$$\langle 0 | \phi | 0 \rangle = \frac{1}{\sqrt{2}} \begin{pmatrix} 0 \\ v \end{pmatrix} \tag{1.57}$$

where we have explicitly chosen a real, non-zero vacuum expectation value for the neutral component of the Higgs doublet to maintain a massless photon, as we shall see. Physically, however, this makes sense - the vacuum is not electrically charged.

The vacuum is a classical state – we want a quantum one. We may express fluctuations about this nonzero expectation value via an expansion as $v + \eta(x) + i\xi(x)$. However, renaming of fields is only meaningful for the non-zero vacuum component - we thus have:

$$\phi = \frac{1}{\sqrt{2}} \begin{pmatrix} \phi_1 + i\phi_2 \\ v + \eta(x) + i\phi_4 \end{pmatrix}. \tag{1.58}$$

where we may expand the Lagrangian listed above:

$$\mathcal{L} = (\partial_\mu \phi)^\dagger (\partial^\mu \phi) - \mu^2 \phi^\dagger \phi - \lambda (\phi^\dagger \phi)^2. \tag{1.59}$$

It is an exercise in algebra to plug in the expansion about v into this Lagrangian: first expanding the potential

$$V(\phi) = \mu^2 \phi^\dagger \phi + \lambda (\phi^\dagger \phi)^2 \tag{1.60}$$

$$= \mu^2 \left(\sum_i \phi_i(x)^2 + (v + \eta(x))^2 \right) + \lambda \left(\sum_i \phi_i(x)^2 + (v + \eta(x))^2 \right) \tag{1.61}$$

$$= -\frac{1}{4} \lambda v^4 + \lambda v^2 \eta^2 + \lambda v \eta^3 + \frac{1}{4} \lambda \eta^4 \tag{1.62}$$

$$+ \frac{1}{2} \lambda \sum_{i \neq j} \phi_i^2 \phi_j^2 + \lambda v \eta \sum_i \phi_i(x)^2 + \frac{1}{2} \lambda \eta^2 \sum_i \phi_i(x)^2 + \frac{1}{4} \sum_i \phi_i(x)^4 \tag{1.63}$$

where the sums are over the $i \in 1, 2, 4$, that is, the fields with 0 vacuum expectation, and we have used the definition $\mu^2 = -\lambda v^2$.

Within this potential, we note a quadratic term in $\eta(x)$ which we may identify with a mass, namely $m_\eta = \sqrt{2\lambda v^2}$, whereas the ϕ_i are massless. These ϕ_i are known as *Goldstone bosons*, and correspond to quantum fluctuations along the minimum of the potential. Of

particular note for this thesis are the interaction terms $\lambda v \eta^3$ and $\frac{1}{4}\lambda\eta^4$, expressing trilinear and quartic self-interactions of the η field.

Expanding the kinetic term

$$(\partial_\mu \phi)^\dagger (\partial^\mu \phi) = \frac{1}{2}\sum_i (\partial_\mu \phi_i)(\partial^\mu \phi_i) + \frac{1}{2}(\partial_\mu (v + \eta(x)))(\partial^\mu (v + \eta(x))) \qquad (1.64)$$

$$= \frac{1}{2}\sum_i (\partial_\mu \phi_i)(\partial^\mu \phi_i) + \frac{1}{2}(\partial_\mu \eta)(\partial^\mu \eta) \qquad (1.65)$$

in a similar way, completing the story of three massless degrees of freedom (Goldstone bosons) and one massive one.

Now, this doublet is embedded in an $SU(2)_L \times U(1)$ theory, so we would like to preserve that gauge invariance. This is achieved in the same way as for the Dirac fields, with the introduction of the electroweak gauge covariant derivative such that the Lagrangian for the Higgs doublet and the electroweak bosons is just

$$\mathcal{L} = (D_\mu \phi)^\dagger (D^\mu \phi) - \mu^2 \phi^\dagger \phi - \lambda(\phi^\dagger \phi)^2 - \frac{1}{4}W_{\mu\nu}^k W_k^{\mu\nu} - \frac{1}{4}F_{\mu\nu}F^{\mu\nu} \qquad (1.66)$$

with $D_\mu = \partial_\mu + ig_W W_\mu^k t^k + ig' \frac{Y}{2} B_\mu$.

We note that it is convenient *TODO: maybe more detail?* to pick a gauge such that the Goldstone fields do not appear in the Lagrangian, upon which we may identify the field $\eta(x)$ with the physical Higgs field, $h(x)$. The field mass terms then very apparently come via the covariant derivative, namely, as

$$W_\mu^k \sigma^k + B_\mu = \begin{pmatrix} W_\mu^3 + B_\mu & W_\mu^1 - iW_\mu^2 \\ W_\mu^1 + iW_\mu^2 & -W_\mu^3 + B_\mu \end{pmatrix} \qquad (1.67)$$

we may then write

$$D_\mu \phi = \frac{1}{2\sqrt{2}} \begin{pmatrix} 2\partial_\mu + ig_W W_\mu^3 + ig'Y B_\mu & ig_W W_\mu^1 + \frac{1}{2}g_W W_\mu^2 \\ ig_W W_\mu^1 - g_W W_\mu^2 & 2\partial_\mu - ig_W W_\mu^3 + ig'Y B_\mu \end{pmatrix} \begin{pmatrix} 0 \\ v + h \end{pmatrix} \qquad (1.68)$$

$$= \frac{1}{2\sqrt{2}} \begin{pmatrix} ig_W(W_\mu^1 - iW_\mu^2)(v + h) \\ (2\partial_\mu - ig_W W_\mu^3 + ig'Y B_\mu)(v + h) \end{pmatrix} \qquad (1.69)$$

As identified above, $Y = 2(Q - I_W^{(3)})$. The Higgs has 0 electric charge, and the lower doublet component has $I_W^{(3)} = -\frac{1}{2}$, yielding $Y = 1$.

Computing $(D_\mu \phi)^\dagger (D^\mu \phi)$, then, yields

$$\frac{1}{8}g_W^2(W_\mu^1 + iW_\mu^2)(W^{\mu 1} - iW^{\mu 2})(v+h)^2 + \frac{1}{8}(2\partial_\mu + ig_W W_{\mu 3} - ig'B_\mu)(2\partial^\mu - ig_W W^{\mu 3} + ig'B^\mu)(v+h)^2 \tag{1.70}$$

and extracting terms quadratic in the fields gives

$$\frac{1}{8}g_W^2 v^2(W_{\mu 1}W^{\mu 1} + W_{\mu 2}W^{\mu 2}) + \frac{1}{8}v^2(g_W W_\mu^3 - g'B_\mu)(g_W W^{\mu 3} - g'B^\mu) \tag{1.71}$$

meaning that W_μ^1 and W_μ^2 have masses $m_W = \frac{1}{2}g_W v$. The neutral boson case is a bit more complicated. Writing the corresponding term as

$$\frac{1}{8}v^2 \begin{pmatrix} W_\mu^3 & B_\mu \end{pmatrix} \begin{pmatrix} g_W^2 & -g_W g' \\ -g_W g' & g'^2 \end{pmatrix} \begin{pmatrix} W^{\mu 3} \\ B^\mu \end{pmatrix} \tag{1.72}$$

we note that we must diagonalize this mass matrix to get the physical mass eigenstates. Doing so in the usual way yields eigenvalues 0, $g'^2 + g_W^2$, thus corresponding to $m_\gamma = 0$ and $m_Z = \frac{1}{2}v\sqrt{g'^2 + g_W^2}$, and eigenvectors *TODO: insert physical field/Weinberg*

TODO: yukawa things

1.7   The Standard Model: A Summary

After all of the above, we may write the Standard Model as a theory with a local $SU(3) \times SU(2)_L \times U(1)_Y$ gauge symmetry, described by the Lagrangian

$$\mathcal{L} = \sum_f \bar{f} i\gamma^\mu D_\mu f - \frac{1}{4} \sum_{gauges} F_{\mu\nu}F^{\mu\nu} + (D_\mu \phi)^\dagger(D^\mu \phi) - \mu^2 \phi^\dagger \phi - \lambda(\phi^\dagger \phi)^2 \tag{1.73}$$

where $D_\mu = \partial_\mu + ig_W W_\mu^k t^k + ig'\frac{Y}{2}B_\mu + ig_S G_\mu^a t^a$.

The $SU(2)_L \times U(1)_Y$ subgroup is spontaneously broken to a $U(1)$ symmetry, lending mass to the associated gauge bosons and associated fermions. Of relevance for this thesis is the resulting physical Higgs field, with a predicted trilinear self-interaction and associated coupling λv, related to the experimentally observed Higgs boson mass by *TODO: insert*

The Standard Model has been monumentally successful, with predictions consistent across many varied experimental cross-checks. This thesis participates in one such cross check. However, the Standard Model is notably not a complete theory of the universe – there is no inclusion of gravity, for instance, though a consistent description may be provided with the introduction of a spin-2 particle. Further, neutrinos are massless in the Standard Model, but are observed via neturino oscillations *TODO: cite* to be massive. No explanation is provided in the Standard *TODO: more things*.

This thesis therefore also participates in searches for physics beyond the Standard Model. We will provide a sketch of the relevant theories in the following chapter, though a detailed theoretical discussion is beyond the scope of this work.

Chapter 2

DI-HIGGS PHENOMENOLOGY AND PHYSICS BEYOND THE STANDARD MODEL

This thesis focuses on searches for di-Higgs production in the $b\bar{b}b\bar{b}$ final state. In this chapter, we will provide a brief overview of the practical theoretical information motivating such searches. Though the searches test for physics beyond the Standard Model, particularly in the search for resonances, the goal of the experimental results is to be somewhat agnostic to particular theoretical frameworks. An in depth treatment of such models is therefore beyond the scope of this thesis, though we will attempt to provide a grounding for the models that we consider.

2.1 Intro to Di-Higgs

Di-Higgs searches can be split into two major theoretical categories: *resonant searches*, in which a physical resonance is produced that subsequently decays into two Higgs bosons, and a *non-resonant searches* in which no physical resonance is produced, but where the HH production cross section has a contribution from an exchange of a *virtual* or *off-shell* particle.

The focus of this thesis is gluon initiated processes – in the case of di-Higgs this is termed gluon-glon fusion (ggF). HH production may also occur via vector boson fusion *TODO: cite https://atlas.web.cern.ch/Atlas/GROUPS/PHYSICS/PAPERS/HDBS-2018-18/*. However the cross section for such production is significantly smaller. Representative Feynman diagrams are shown in *TODO: add diagrams*.

TODO: show heavier couples more strongly to Higgs - just fill in Yukawa above. However, the top quark has a mass of $173\,\mathrm{GeV}$, whereas the H has a mass of $125\,\mathrm{GeV}$, such that $H \to t\bar{t}$ is kinematically disfavored. $H \to b\bar{b}$ is therefore the dominant fermionic Higgs decay

mode, and, in fact, the dominant overall decay mode, with a branching fraction of around 58 %. The dominant top quark Yukawa coupling to the H does play a role in H production, however – gluon-gluon fusion is dominated by processes including a top loop.

The single H properties translate to HH production, with $HH \rightarrow b\bar{b}b\bar{b}$ accounting for around 34 % of all HH decays. The H H branching fractions are shown in Figure *TODO: add*.

2.2 Resonant HH Searches

Resonant di-Higgs production is predicted in a variety of extensions to the Standard Model. In particular, due to *TODO: constraints*, this thesis presents searches for both spin-0 and spin-2 resonances. Each are implemented in a particular theoretical context, but set up experimental results for generic searches.

The spin-2 signal considered is implemented within the bulk Randall-Sundrum (RS) model [1], which features spin-2 Kaluza-Klein gravitons, G_{KK}^*, that are produced via gluon-fusion and which may decay to a pair of Higgs bosons. This model was considered in the early Run 2 analysis *TODO: cite*, and was excluded across much of the relevant mass range.

The primary theoretical focus of this work is therefore the spin-0 result, which is implemented as a generic resonance with width below detector resolution. Scalar resonances are interesting, for instance, in the context of two Higgs doublet models [2], which posit the existence of a second Higgs doublet. This leads to the existence of five scalar particles in the Higgs sector – roughly, two complex doublets provide eight degrees of freedom, three of which are "eaten" by the electroweak bosons, leaving five degrees of freedom which may correspond to physical fields.

TODO: check out other theory motivation - there are some good HH talks

2.3 Non-resonant HH Searches

Non-resonant HH production is predicted by the Standard Model via the trilinear coupling discussed above, as well as via production in a fermion loop. More explicitly, after electroweak

symmetry breaking, we have *TODO: add Yukawa*

$$\mathcal{L}_{SM} \supset -\lambda v^2 h^2 - \lambda v h^3 - \frac{1}{4}\lambda h^4 \qquad (2.1)$$

$$= -\frac{1}{2}m_H^2 - \lambda_{HHH}^{SM} v h^3 - \lambda_{HHHH}^{SM} h^4 \qquad (2.2)$$

where $m_H = \sqrt{2\lambda v^2}$ so that

$$\lambda_{HHH}^{SM} = \frac{m_H^2}{2v^2}. \qquad (2.3)$$

The mass of the SM Higgs boson has been experimentally measured to be $125\,\text{GeV}$ *TODO: cite*, and the vacuum expectation value $v = 246\,\text{GeV}$ has a precise determination from the muon lifetime *TODO: cite*. This coupling is therefore precisely predicted in the Standard Model, such that an observed deviation from this prediction would be a clear sign of new physics.

The relevant diagrams for non-resonant HH production are shown in Figure *TODO: add diagrams*. Notably, the diagrams *interfere* with each other, which can be easily seen by counting the fermion lines. *TODO: Some good stuff in here https://arxiv.org/pdf/1504.05596.pdf*.

For the searches presented here, the quark couplings to the Higgs are considered to be consistent with the Standard Model value, with measurements of the dominant top Yukawa coupling left to more sensitive direct measurements *TODO: cite e.g. https://arxiv.org/pdf/2009.07123.pdf*. Variations of the trilinear coupling away from the Standard Model are considered, however. Such variations are parametrized via

$$\kappa_\lambda = \frac{\lambda_{HHH}}{\lambda_{HHH}^{SM}} \qquad (2.4)$$

where λ_{HHH} is a varied coupling, whereas λ_{HHH}^{SM} is the Standard Model prediction, given by As this variation only impacts the *triangle* diagram, significant and interesting effects are observed due to this interference. Examples of the impact of this tradeoff on the di-Higgs invariant mass are shown in *TODO: include plot*. Generally speaking, for positive values of κ_λ, more events are predicted at low mass, whereas for negative values of κ_λ, more events are predicted at high mass.

Chapter 3

EXPERIMENTAL APPARATUS

What machines must we build to examine the smallest pieces of the universe? The famous equation $E = m$ provides that to create massive particles, we need to provide enough energy. In order to give kinematic phase space to the types of processes that are examined in this thesis (and many others besides), a system must be created in which there is enough energy to (at bare minimum), overcome kinematic thresholds: if you want to search for HH decays, you should have at least $250\,\mathrm{GeV}$ ($= 2 \times m_H$) to work with. It is not enough to simply induce such processes, however. These processes need to be captured in some way, emitted energy and particles must be characterized and identified, and in the end all of this information must be put into a useful and useable form such that selections can be made, statistics can be run, and a meaningful statement can be made about the universe. In this chapter, we describe the machines behind the physics, namely the Large Hadron Collider and the ATLAS experiment.

3.1 The Large Hadron Collider

The Large Hadron Collider is a particle accelerator near Geneva, Switzerland, operating at a center of mass energy $\sqrt{s} = 13\,\mathrm{TeV}$. In broad scope, it is a ring with a 27 kilometer circumference. Hadrons (usually protons or heavy ions) move in two counter-circulating beams, which are made to collide at four collision points at various points on the ring. These four collision points correspond to the four detectors placed around the ring: two "general purpose" experiments: ATLAS and CMS; LHCb, focused primarily on flavor physics; and ALICE, focused primarily on heavy ions.

For proton-proton collisions, the focus of this thesis, the acceleration chain proceeds as follows: first, and electric field strips hydrogen of its electrons, creating protons. A linear

accelerator, LINAC 2, accelerates protons to $50\,\text{MeV}$. The resulting beam is injected into the Proton Synchrotron Booster (PSB), which pushes the protons to $1.4\,\text{GeV}$, and then the Proton Synchrotron, which brings the beam to $25\,\text{GeV}$.

Protons are then transferred to the Super Proton Synchrotron (SPS), which ramps up the energy to $450\,\text{GeV}$. Finally, the protons enter the LHC itself, bringing the beam up to $6.5\,\text{TeV}$. *TODO: cite: https://home.cern/science/accelerators/accelerator-complex*

While there is, of course, much that goes into the Large Hadron Collider development and operation, perhaps two of the most fundamental ideas are (1) how are the beams directed and manipulated and (2) what do we mean when we say "protons are accelerated". These questions both are directly answered by pieces of hardware, namely (1) magnets and (2) radiofrequency (RF) cavities.

One of fundamental components of the LHC is a large set of superconducting magnets *TODO: material?*. These are cooled by liquid helium to achieve superconducting temperatures, and there are several types with very specific purposes. The obvious first question with a circular accelerator is how to keep the particle beam moving around in that circle. This job is done via a set of dipole magnets placed around the *beam pipes*: the tubes containing the beam. These are designed such that the magnetic field in the center of the beam pipe runs perpendicular to the velocity of the charged particles, providing the necessary centripetal force for the synchrotron motion.

A proton beam is not made of a single proton, however, but of many protons, grouped into a series of *bunches*. As all of these are positively charged, if unchecked, these bunches would become diffuse and break apart. What we want is a stable beam with tightly clustered protons to maximize the chance of a high energy collision. Such clustering is done via a series of quadropole magnets, with field distributed as in *TODO: grab image from General Exam*. Alternating sets of quadropoles provide the necessary forces for a tight, stable beam. While these are the two major components of the LHC magnet system, it is not the full story – higher order magnets are used to correct for small imperfections in the beam *TODO: expand*.

Magnetic fields do no work, however, so the magnet system is unable to do the job of the

actual acceleration. This is accomplished via a set of radiofrequency (RF) cavities. Within these cavities, an electric field is made to oscillate (switch direction) at a precise rate. These rates interact with the beam via in RF *buckets*, with bunches corresponding to groups of protons that fill a given bucket. The timing is such that protons will always experience an accelerating voltage, corresponding to the 25 ns bunch spacing used at the LHC.

A nice property of this bucket/bunch configuration is that there is some self-correction – there is some finite spread in the grouping of particles. If a particle arrives too early, it will experience some decelerating voltage; if too late, it will experience a higher accelerating voltage.

3.2 The ATLAS Experiment
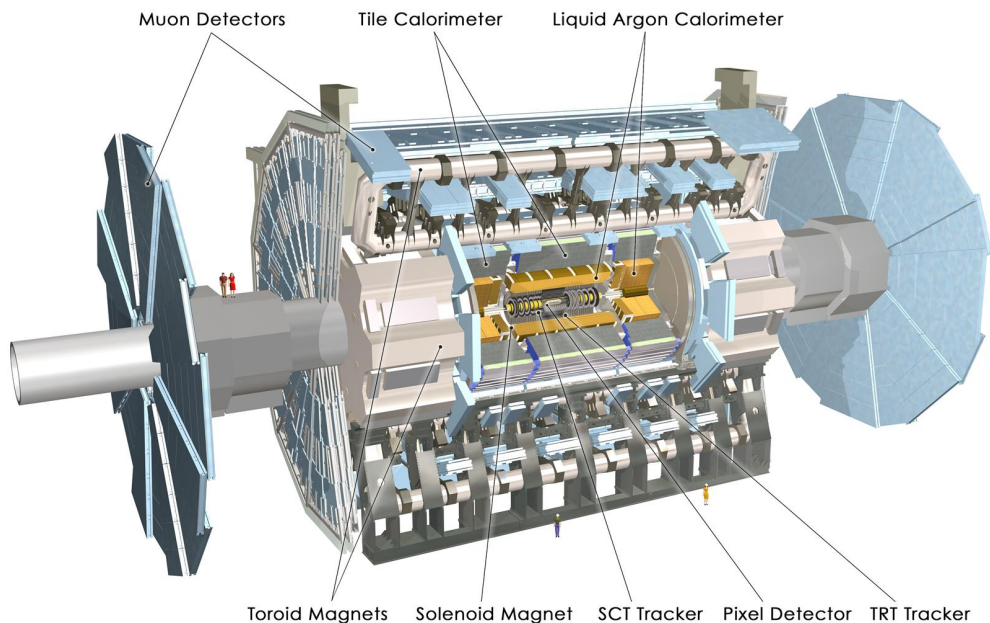
Figure 3.1: Diagram of the ATLAS detector [3]

This thesis focuses on searches done with the ATLAS experiment. As mentioned, this is one of two "general purpose" experiments at the LHC, by which we mean there is a very large and

broad variety of physics done within the experimental collaboration. This broad physics focus has a direct relation to the design of the ATLAS detector [4], pictured in Figure 3.1, which is composed of a sophisticated set of subsystems designed to fully characterize the physics of a given high energy particle collision. It consists of an inner tracking detector surrounded by a thin superconducting solenoid, electromagnetic and hadronic calorimeters, and a muon spectrometer incorporating three large superconducting toroidal magnets. The ATLAS detector covers nearly the entire solid angle around the collision point, fully characterizing the "visible" components of a collision and allowing for indirect sensitivity to particles that do not interact with the detector (e.g. neutrinos) via "missing" energy (roughly momentum balance). We will go through the design and physics contribution of each of the detector components in the following. A schematic of how various particles interact with the detector is shown in Figure 3.2.

3.2.1 ATLAS Coordinate System

Of relevance for the following discussion, as well as for the analysis presented in Chapter 7, is the ATLAS coordinate system. ATLAS uses a right-handed coordinate system with its origin at the nominal interaction point (IP) in the center of the detector and the z-axis along the beam pipe. The x-axis points from the IP to the centre of the LHC ring, and the y-axis points upwards. Cylindrical coordinates (r, ϕ) are used in the transverse plane, ϕ being the azimuthal angle around the z-axis. The pseudorapidity is defined in terms of the polar angle θ as $\eta = -\ln \tan(\theta/2)$. Angular distance is measured in units of $\Delta R \equiv \sqrt{(\Delta \eta)^2 + (\Delta \phi)^2}$. These coordinates are shown in Figure *TODO: add coordinate figure*

3.2.2 Inner Detector

The inner-detector system (ID) is immersed in a $2\,\mathrm{T}$ axial magnetic field and provides charged-particle tracking in the range $|\eta| < 2.5$. The high-granularity silicon pixel detector covers the vertex region and typically provides four measurements per track, the first hit normally being in the insertable B-layer (IBL) installed before Run 2 [6, 7]. It is followed by the silicon
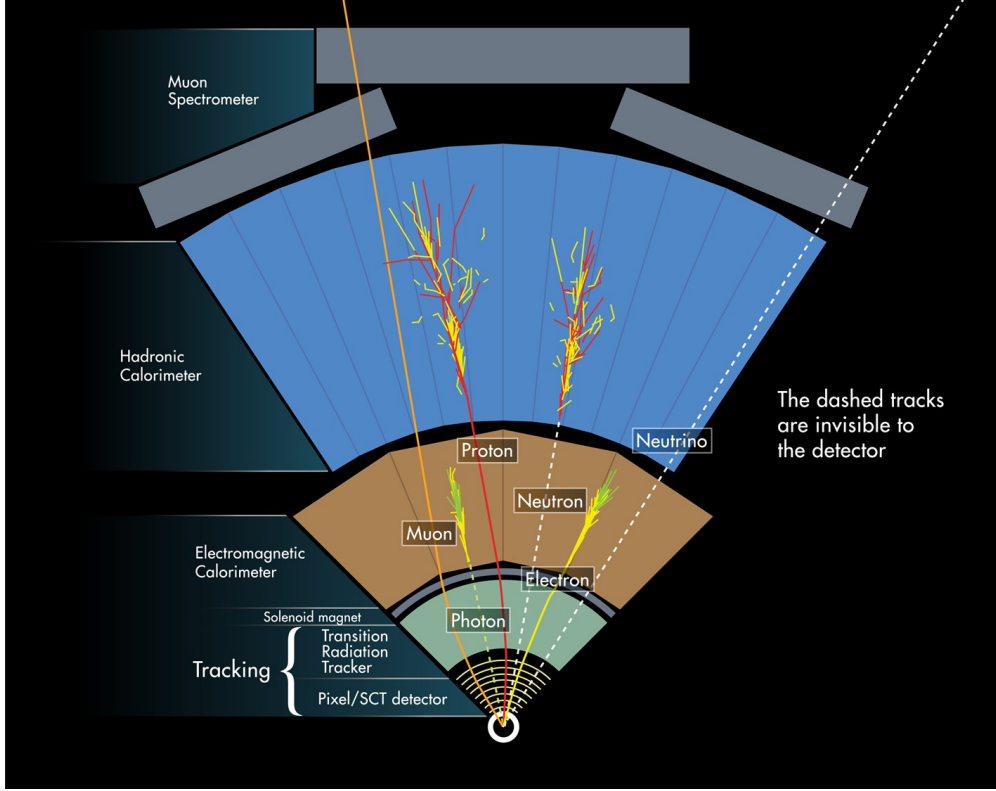
Figure 3.2: Cross section of the ATLAS detector showing how particles interact with various detector components [5]

microstrip tracker (SCT), which usually provides eight measurements per track. These silicon detectors are complemented by the transition radiation tracker (TRT), which enables radially extended track reconstruction up to $|\eta| = 2.0$. The TRT also provides electron identification information based on the fraction of hits (typically 30 in total) above a higher energy-deposit threshold corresponding to transition radiation.

3.2.3   Calorimeter

The calorimeter system covers the pseudorapidity range $|\eta| < 4.9$. Within the region $|\eta| < 3.2$, electromagnetic calorimetry is provided by barrel and endcap high-granularity lead/liquid-argon (LAr) calorimeters, with an additional thin LAr presampler covering $|\eta| < 1.8$ to correct

for energy loss in material upstream of the calorimeters. Hadron calorimetry is provided by the steel/scintillator-tile calorimeter, segmented into three barrel structures within $|\eta| < 1.7$, and two copper/LAr hadron endcap calorimeters. The solid angle coverage is completed with forward copper/LAr and tungsten/LAr calorimeter modules optimised for electromagnetic and hadronic energy measurements respectively.

3.2.4   Muon Spectrometer

The muon spectrometer (MS) comprises separate trigger and high-precision tracking chambers measuring the deflection of muons in a magnetic field generated by the superconducting air-core toroidal magnets. The field integral of the toroids ranges between 2.0 and 6.0 T m across most of the detector. A set of precision chambers covers the region $|\eta| < 2.7$ with three layers of monitored drift tubes, complemented by cathode-strip chambers in the forward region, where the background is highest. The muon trigger system covers the range $|\eta| < 2.4$ with resistive-plate chambers in the barrel, and thin-gap chambers in the endcap regions.

3.2.5   Triggering

Interesting events are selected by the first-level trigger system implemented in custom hardware, followed by selections made by algorithms implemented in software in the high-level trigger [8]. The first-level trigger accepts events from the 40 MHz bunch crossings at a rate below 100 kHz, which the high-level trigger further reduces in order to record events to disk at about 1 kHz.

An extensive software suite [9] is used for real and simulated data reconstruction and analysis, for operation and in the trigger and data acquisition systems of the experiment.

Chapter 4

SIMULATION

Simulated physics samples are a core piece of the physics output of the Large Hadron Collider, providing a map from a physics theory into what is observed in our detector. This is crucial for searches for new physics, where simulation is necessary to describe what a given signal model looks like, but also extremely valuable for describing the physics of the Standard Model, providing detailed predictions of background processes for use in everything from designing simple cuts to training multivariate discriminators. Broadly, simulation can be split into two stages: *event generation*, in which physics theory is used to generate a description of particles present after a proton-proton collision, and *detector simulation*, which passes this particle description through a simulation of the detector material, providing a view of the physics event as it would be seen in ATLAS data. Such simulation is often called Monte Carlo in reference to the underlying mathematical framework, which relies on random sampling.

4.1   Event Generation

A variety of tools are used to simulate various aspects of event generation. MADGRAPH [10] is commonly used for the generation of the "hard scatter" event, i.e., two protons collide and some desired physics process happens. In practice, this is not quite as simple as two quarks or gluons interacting. Protons are composed of three "valence" quarks with various momenta interacting with each other via exchange of gluons, but also a sea of virtual gluons which may decay into other quarks. A hard scatter event is therefore characterized by the corresponding particle level diagrams, but additionally by a set of *parton distribution functions* (PDFs), which describe the probablity to find constituent quarks or gluons at carrying various momenta at a given energy scale (often written Q^2). Such PDFs are measured

experimentally *TODO: cite* and the selection of a "PDF set" and a given physics process characterizes the hard scatter. Depending on the model being considered and the particular theoretical constraints, processes are often simulated at either leading (LO) or next to leading order (NLO), corresponding to the order of the perturbative expansion (i.e. tree level or 1 loop diagrams). Various additional tools are developed for such NLO calculations, including POWHEG BOX v2 [11–13], which is used for this thesis.

The hard scatter is not the only component of a given collider event, however. Incoming and outgoing particles are themselves very energetic and may radiate particles along their trajectory. In particular, gluons, which have a self-interaction term as described in Chapter 1, may be radiated, which subesquently themselves radiate gluons or decay to quarks which can also radiate gluons, in a whole mess of QCD that both contributes to the particle content of a collider event and is not directly described by the hard scatter. This cascade, called a *parton shower*, has a dedicated set of simulation tools, commonly HERWIG 7 [14][15] and PYTHIA 8 [16], which interface with tools such as MADGRAPH for simulation.

Due to color confinement (Chapter 1), quarks and gluons cannot be observed free particles, but rather undergo a process called hadronization, in which they are grouped into colorless hadrons (e.g. *mesons*, consisting of one quark and one antiquark). In simulation, this is also handled with HERWIG 7 and PYTHIA 8.

The physics of b-quarks is quite important for a variety of searches for new physics and measurements of the Standard Model, including this thesis work *TODO: ref flavor tagging sec?*. Correspondingly, the decay of "heavy flavor" particles (e.g. B and D mesons, containing b and c quarks respectively) has been very well studied, and a dedicated simulation tool, EVTGEN [17], is used for such processes.

TODO: add nice parton shower image

4.2   Detector Simulation

Event generation provides a full description of the particle content of a given collider event. In reality, however, we do not have access to such a description, and must rely on physical

detectors to collect information about said particle content. The design and components of the ATLAS detector are described in Chapter 3. Simulation of this detector quickly becomes complicated – there are a variety of different materials and subdetectors, each with particular configurations and resolutions. Interactions of particles with the detector materials can cause showering, and such showers must be simulated and characterized.

In ATLAS, the GEANT4 [18] simulation toolkit is used for detailed simulation of the ATLAS detector, often referred to as *full simulation*. The method can be thought of as proceeding step by step as a particle moves through the detector, simulating the interaction of the material at each stage, and following each branch of each resulting shower with a similarly detailed step by step simulation.

This type of simulation is very computationally intensive, especially in the calorimeter, which has a high density of material, leading to an extremely large set of material interactions to simulate. There is correspondingly a large effort within ATLAS to develop techniques to decrease the computational load – these techniques will be of increasing importance for Run 3 and the HL-LHC *TODO: include classic budget plot*.

The fast simulation used for this thesis, AtlFast-II [19], is one such technique, which uses a parametrized simulation of the calorimeter, called FastCaloSim, in conjunction with full simulation of the inner detector, to achieve an order of magnitude speed up in simulation time. This parametrized simulation uses a simplified detector geometry, in conjunction with a simulation of particle shower development based on statistical sampling of distributions from fully simulated events, to massively speed up simulation time and computational load.

Such a speed up comes at a bit of a cost in performance. In particular, the modeling of jet substructure (see Chapter 5) historically has been an issue for FastCaloSim. The ATLAS authorship qualification work supporting this thesis is an effort to improve such modeling, and is part of a suite of updates being considered for a new fast simulation targeting Run 3. We briefly describe this work in the following.

4.3   Correlated Fluctuations in FastCaloSim

A variety of developments have been made to FastCaloSim, improving on the version used for AtlFast-II. This new fast calorimeter simulation [20] is largely based on two components: one which describes the *total energy* deposited in each calorimeter layer as a shower moves from the interaction point outward, and one which describes the *shape*, i.e., the pattern of energy deposits, of a shower in each respective calorimeter layer. Both methods are parametrizations of the full simulation, and therefore are considered to be performing well if they are able to reproduce corresponding full simulation distributions. Of course, directly sampling from a library of showers would identically reproduce such distributions – however a statistical sampling of various shower *properties* provides much more generality in the simulation.

For the simulation of total energy in each given layer, the primary challenge is that such energy deposits are highly correlated. The new FastCaloSim thus relies on a technique called Principal Component Analysis (PCA) *TODO: cite https://root.cern.ch/doc/master/classTPrincipal.html* to de-correlate the layers, aiding parametrisation.

The PCA chain transforms N energy inputs into N Gaussians and projects these Gaussians onto the eigenvectors of the corresponding covariance matrix. This results in N de-correlated components, as the eigenvectors are orthogonal. The component of the PCA decomposition with the largest corresponding eigenvalue is then used to define bins, in which showers demonstrate similar patterns of energy deposition across the calorimeter layers. To further de-correlate the inputs, the PCA chain is repeated on the showers within each such bin. This full process is reversed for the particle simulation. A full description of the method can be found in [20].

Modeling of the lateral shower shape makes use of 2D histograms filled with GEANT4 hit energies in each layer and PCA bin. Binned in polar $\alpha - R$ coordinates in a local plane tangential to the surface of the calorimeter system, these histograms represent the spatial distribution of energy deposits for a given particle shower. Such histograms are constructed for a number of Geant4 events, and the histograms for each event are normalized to total

energy deposited in the given layer. The average of these histograms is then taken (what is called here the "average shape").

In simulation, these average shape histograms are used as probability distributions, from which a finite number of equal energy hits are drawn. This finite drawing of hits induces a statistical fluctuation about the average shape which is tuned to match the expected calorimeter sampling uncertainty.

As an example, the intrinsic resolution of the ATLAS Liquid Argon calorimeter has a sampling term of $\sigma_{\mathrm{samp}} \approx 10\%/\sqrt{E}$ [21]. The number of hits to be drawn for each layer, $N_{\mathrm{hits}}^{\mathrm{layer}}$, is thus taken from a Poisson distribution with mean $1/\sigma_{\mathrm{samp}}^2$, where the energy assigned to each hit is then just $E_{\mathrm{hit}} = \frac{E_{\mathrm{layer}}}{N_{\mathrm{hits}}^{\mathrm{layer}}}$. This induces a fluctuation of the order of $10\%/\sqrt{E_{\mathrm{bin}}}$ for each bin in the average shape.

Figure 4.1 shows a comparison of energy and weta2 [22], defined as the energy weighted lateral width of a shower in the second electromagnetic calorimeter layer, for 16 GeV photons simulated with the new FastCaloSim and with full GEANT4 simulation. The agreement is quite good, with FastCaloSim matching the Geant4 mean to within 0.3 and 0.03 percent respectively. Similar results are seen for other photon energies and η points.
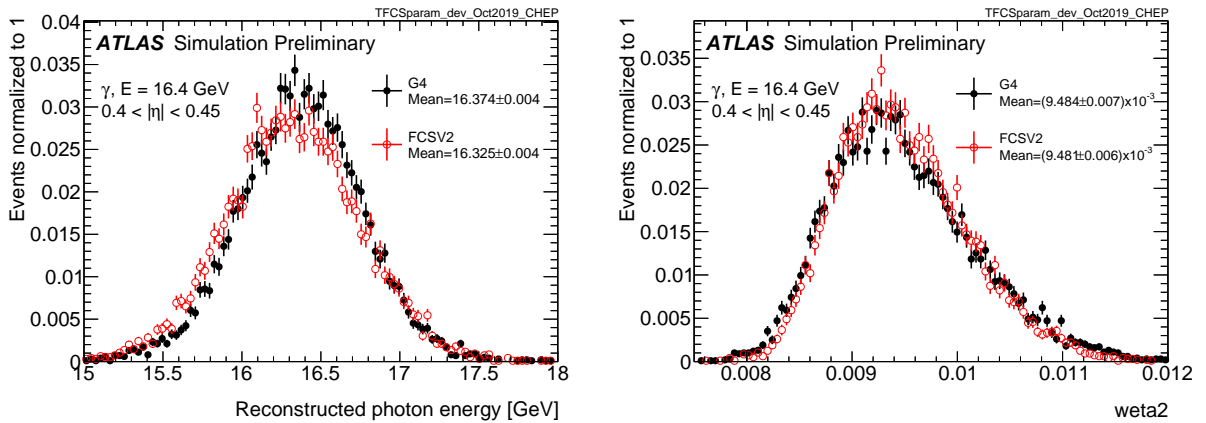
Figure 4.1: Energy and lateral shower width variable, weta2, for 16 GeV photons with full simulation (G4) and FastCaloSimV2 (FCSV2) [20].

4.3.1 Fluctuation Modeling

Figure 4.2 shows the ratio of calorimeter cell energies for single GEANT4 photon and pion events to the corresponding cell energies in their respective average shapes. While the photon event is quite close to the corresponding average, the pion event shows a deviation from the average which is much larger and has a non-trivial structure, reflecting the different natures of electromagnetic and hadronic showering.

While the shape parametrization described above is thus sufficient for describing electromagnetic showers, we will demonstrate below that it is not sufficient for describing hadronic showers (Figures 4.5 and 4.6). We therefore present and validate methods to improve this hadronic shower modeling.

Two methods for modeling deviations from the average shape have been studied: (1) a neural network based approach using a Variational Autoencoder (VAE) [23] and (2) a map through cumulative distributions to an n-dimensional Gaussian. With both methods, the shape simulation then proceeds as described in Section ??, with the drawing of hits according to the average shape. However, these hits no longer have equal energy, but have weights applied to increase or decrease their energy depending on their spatial position. This application of weights is designed to mimic a realistic shower structure and to encode correlations between energy deposits.

Both methods are trained on ratios of energy in binned units called voxels. This voxelization is performed in the same polar $\alpha - R$ coordinates as the average shape, with a 5 mm core in R and 20 mm binning thereafter. There are a total of 8 α bins from 0 to 2π and 8 additional R bins from 5 mm to 165 mm. The 5 mm core is filled with the average value of core voxels across the 8 α bins when creating the parametrisation. However, during simulation, each of these 8 core bins is treated independently. The outputs of both methods mimic these energy ratios and are used in the shape simulation as the weights described above. In contrast to an approach based on, e.g., calorimeter cells, using voxels allows for flexibility in tuning the binning used in creating the parametrisation. Further, due to their relatively large size, using
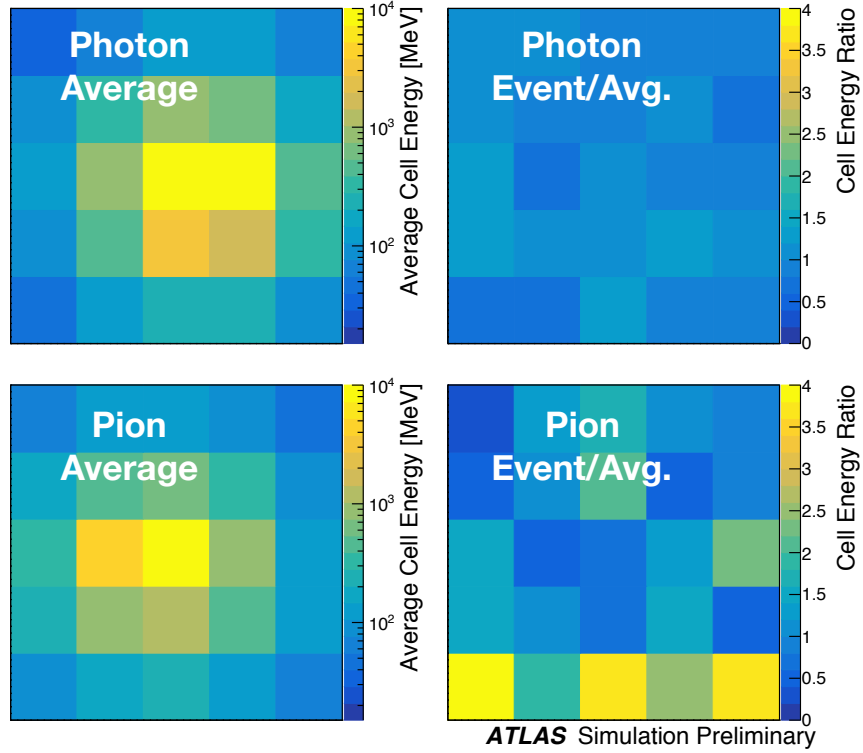
Figure 4.2: Example of photon and pion average shapes in 5×5 calorimeter cells. The left column shows the average shape over a sample of 10000 events, while the right column shows the energy ratio, in each cell, of single GEANT4 events with respect to this average. The photon ratios are all close to 1, while the pion ratios show significant deviation from the average.

calorimeter cells is subject to "edge effects", where the splitting of energy between cells has a non-trivial effect on the observed energy ratio. The binning used here is of the order of half of a cell size, mitigating this effect.

The Gaussian method operates by using cumulative distributions to map GEANT4 energy ratios to a multidimensional Gaussian distribution. New events are generated by randomly sampling from this Gaussian distribution.

For the VAE method, a system of two linked neural networks is trained to generate events.

The first "encoder" neural network maps input GEANT4 energy ratios to a lower dimensional latent space. A second "decoder" neural network then samples from that latent space and tries to reproduce the inputs. In simulation, events are generated by taking random samples from the latent space and passing them through the trained decoder.
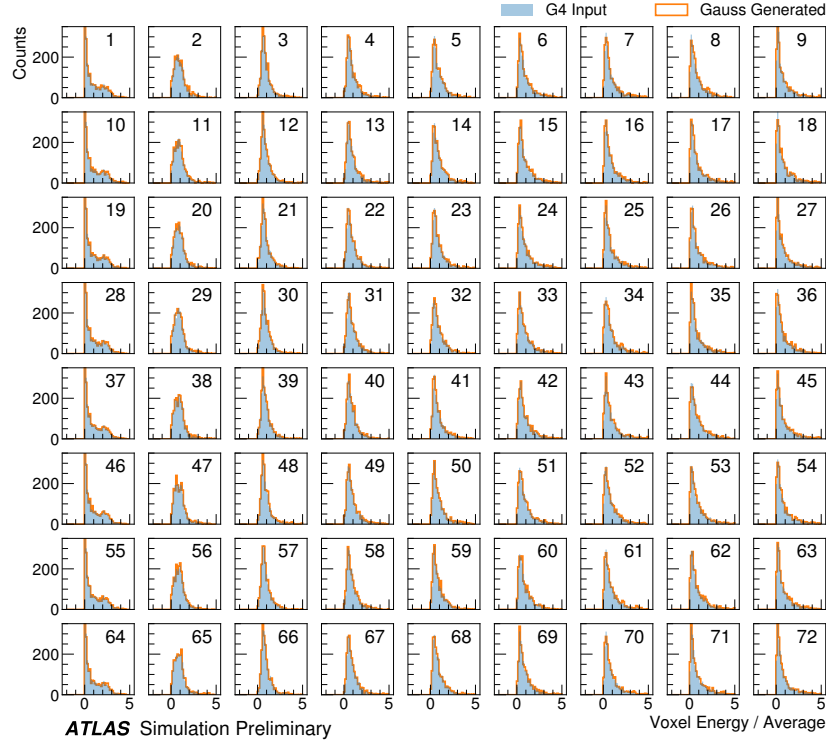
Figure 4.3: Distribution of the ratio of voxel energy in single events to the corresponding voxel energy in the average shape, with GEANT4 events in blue and Gaussian model events in orange, for 65 GeV central pions in EMB2. Moving top to bottom corresponds to increasing α, left to right corresponds to increasing R, with core voxels numbered 1, 10, 19, ... Agreement is quite good across all voxels. Results are similar for the VAE method.

Figure 4.3 shows the distributions of input GEANT4 and Gaussian method generated energy ratios in the grid of voxels. Figure 4.4 shows the correlation coefficient between the center voxel from $\alpha = 0$ to $2\pi/8$ for input GEANT4 and the Gaussian and VAE fluctuation
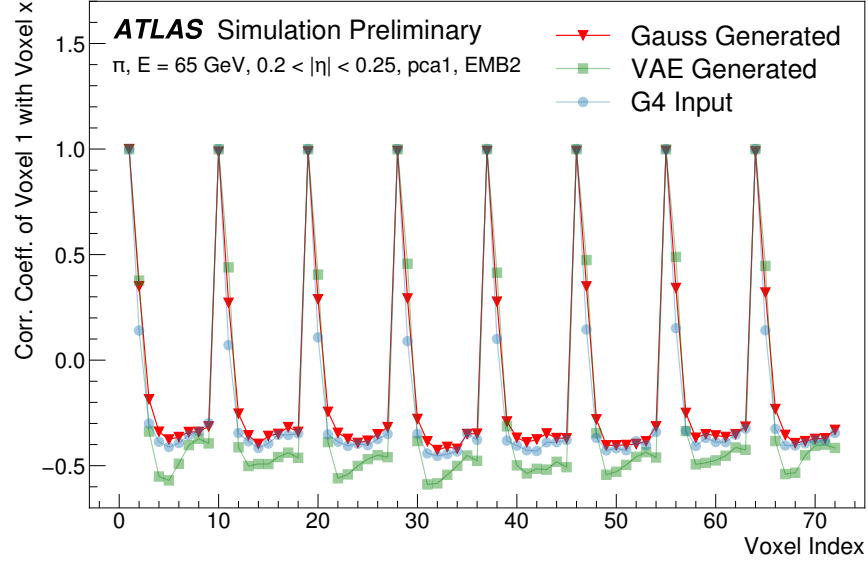
Figure 4.4: Correlation coefficient of ratios of voxel energy in single events to the corresponding voxel energy in the average shape, examined between the core bin from $\alpha = 0$ to $2\pi/8$ and each of the other voxels. The periodic structure represents the binning in α, and the increasing numbers in each of these periods correspond to increasing R, where the eight points with correlation coefficient 1 are the eight core bins. Both the Gaussian and VAE generated toy events are able to reproduce the major correlation structures for 65 GeV central pions in EMB2.

methods. Agreement is good throughout.

Validation of the Gaussian and VAE fluctuation methods was performed within FastCaloSimV2. Figure 4.5 shows the energy ratio of cells for a given simulation to the corresponding cells in the average shape as a function of the distance from the shower center. The mean for all simulation methods is expected to be around 1, with deviation from the average (the RMS fluctuation) shown by the error bars. The Gaussian method RMS (red) and VAE method RMS (green) both match the GEANT4 RMS (yellow) better than the case without correlated fluctuations (blue) for a variety of energies, η points, and layers, often reproducing $80-100\,\%$
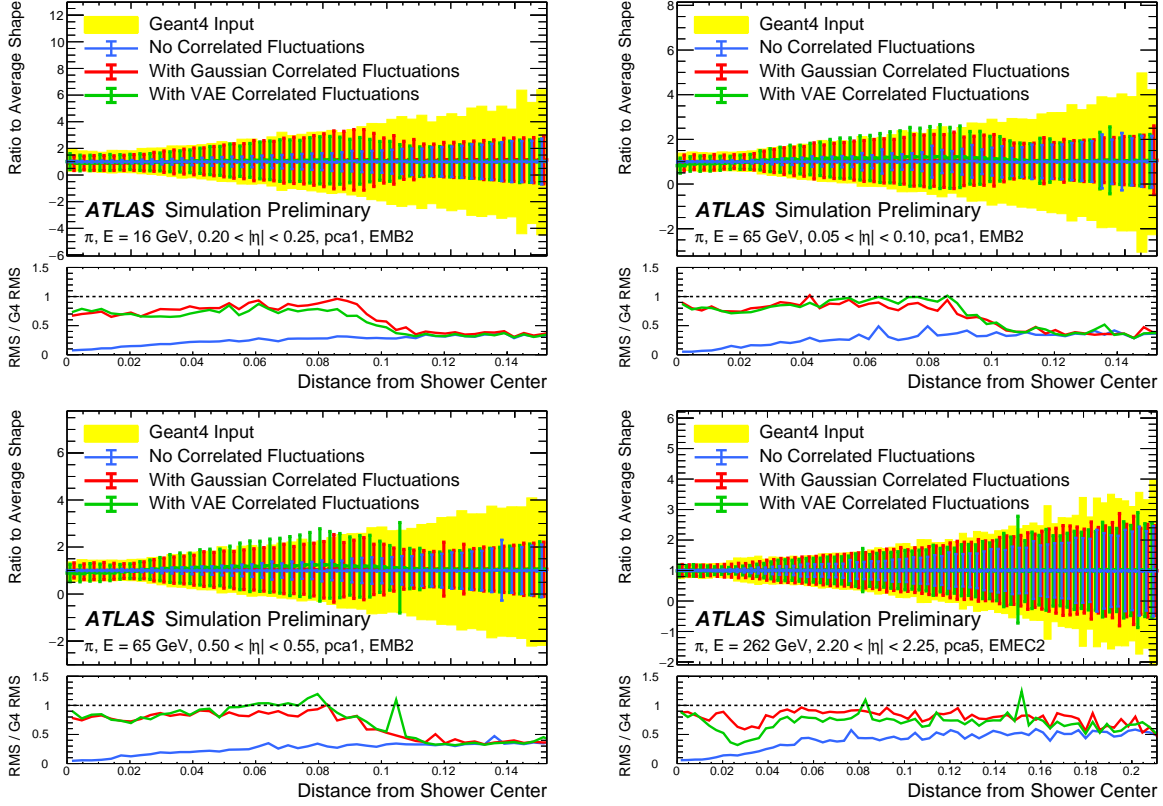
Figure 4.5: Comparison of the RMS fluctuations about the average shape with the Gaussian fluctuation model (red), the VAE fluctuation model (green), and without correlated fluctuations (blue) for a range of pion energies, η points, and layers.

of the GEANT4 RMS magnitude, compared to the $5 - 30\%$ observed in the no correlated fluctuations case.

Figure 4.6 shows the result of a simulation with full ATLAS reconstruction for 65 GeV central pions with the Gaussian fluctuation model. The simulation with the Gaussian fluctuation model demonstrates improved modeling of several shape variables relative to baseline FastCaloSimV2, reproducing the distributions of events simulated with GEANT4.

The new fast calorimeter simulation is a crucial part of the future of simulation for the ATLAS Experiment at the LHC. The per event simulation time of the full detector with GEANT4,
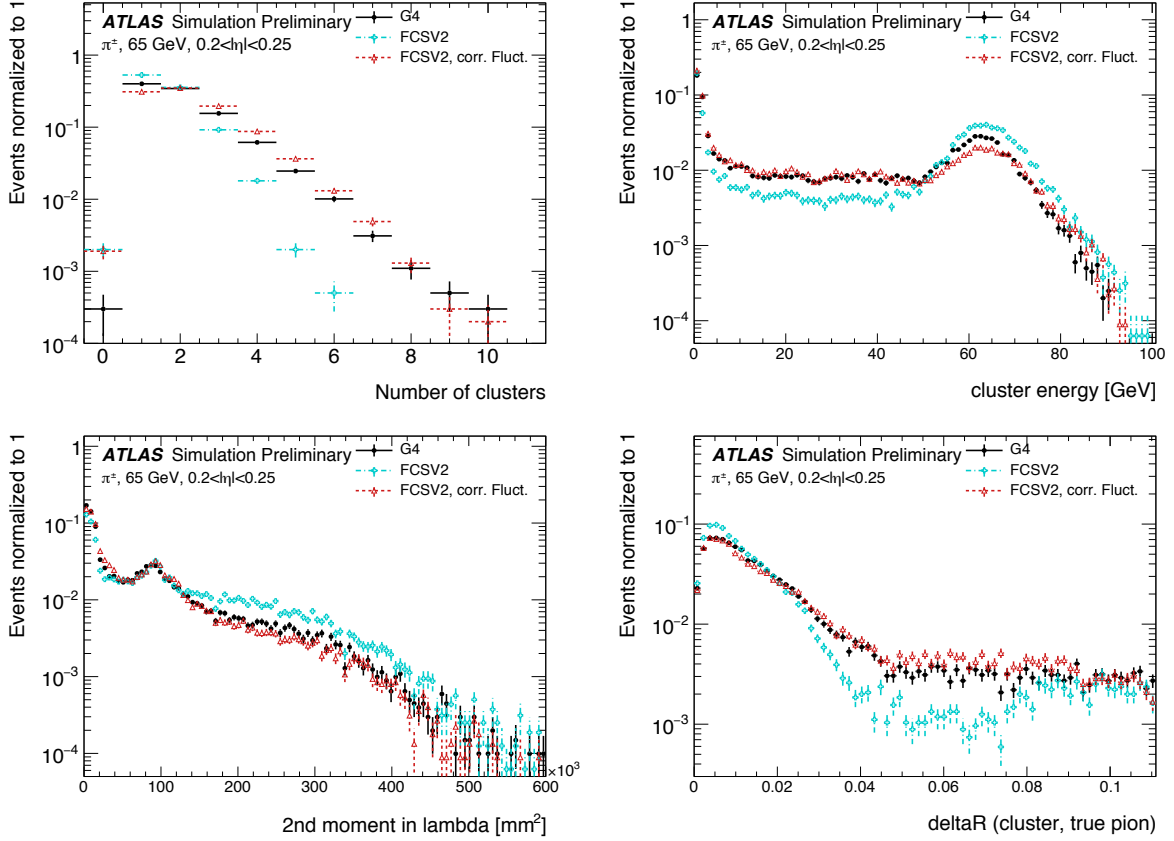
Figure 4.6: Comparison of the Gaussian fluctuation model to the default FCSV2 version and to G4 simulation, using pions of 65 GeV energy and $0.2 < |\eta| < 0.25$. With the correlated fluctuations, several shape variables demonstrate improved modeling.

calculated over 100 $t\bar{t}$ events, is 228.9 s. Using FastCaloSim for the calorimeter simulation reduces this to 26.6 s, of which FastCaloSim itself is only 0.015 s. Good physics modeling is achieved, the correlated fluctuations method shows good proof of concept improvement for the modeling of hadronic showers.

Chapter 5

RECONSTRUCTION

Chapter 3 discusses how a proton-proton collision may be captured by a physical detector and turned into data that may be stored and analyzed. Chapter 4 discusses the simulation of this same process. At this most basic level, however, the ATLAS detector is only a machine for turning particles into a set of electrical signals, albeit in a very sophisticated, physics motivated way. This chapter discusses the step of turning these electrical signals into objects which may be identified with the underlying physics processes, and therefore used to make statements about what occured within a given collision event. This process is termed *reconstruction*, and we will focus particularly on jets and flavor tagging, as the most relevant pieces for this thesis work.

5.1 Jets

As discussed in Chapters 3 and 4, the production of particles with color charge from a proton-proton interaction is complicated both by parton showering and by confinement: a quark produced from a hard scatter is not seen as a quark, but rather, as a spray of particles with a variety of hadrons in the final state, which subsequently shower upon interaction with the calorimeter in a complicated way.

For hard scatter electrons, photons, or muons on the other hand, the picture is much clearer: there is no parton showering, and each has a distinct signature in the detector: photons have no tracks and a very localized calorimeter shower, electrons are associated with tracks and are similarly localized in the calorimeter, and muons are associated with tracks, pass through the calorimeter due to their large mass, and leave signatures in the muon spectrometer.

Jets are a tool to deal with the messiness of quarks and gluons. The basic concept is to group the multitude of particles produced by a quark or gluon decay into a single object. Such an object then has associated properties, including a four-vector, which may be identified with the corresponding initial state particle. In practice a variety of information from the ATLAS detector is used for such a reconstruction. The analysis considered in this thesis uses particle flow jets [24], which combines information from both the tracker and the calorimeter, where the combined objects may be identified with underlying particles. However, jets built from clusters of calorimeter cells [25] as well as from charged particle tracks [26] have also been used very effectively.

A variety of algorithms are used to associate detector level objects to a given jet. The most commonly used in ATLAS is the anti-k_T algorithm [27], which is a successor to the k_T algorithm, among others [28], and develops as follows. Both algorithms are sequential recombination algorithms, which begin with the smallest distance, d_{ij} between considered objects (e.g. particles or intermediate groupings of particles). If d_{ij} is less than a parameter d_{iB} (B for "beam") object i is combined with object j, the distance d_{ij} is recomputed, and the process repeats. This proceeds until $d_{ij} \geq d_{iB}$, at which point the jet is "complete" and removed from the list of considered objects.

The definitional difference between k_T and anti-k_T is these distance parameters. In general form, these are defined as

$$d_{ij} = \min(p_{Ti}^{2p}, p_{Tj}^{2p})\frac{\Delta R_{ij}^2}{R^2} \tag{5.1}$$

$$d_{iB} = p_{Ti}^{2p} \tag{5.2}$$

where p_{Ti} is the transverse momentum of object i, ΔR_{ij} is the angular distance between objects i and j, R is a radius parameter, and p controls the tradeoff between the p_T and angular distance terms. For the k_T algorithm $p = 1$; for the anti-k_T algorithm, $p = -1$. This is a simple change, but results in significantly different behavior.

The anti-k_T algorithm can be understood as follows: for a single high p_T particle (p_{T1}) surrounded by a bunch of low p_T particles, the low p_T particles will be clustered with the

high p_T one if

$$d_{1j} = \frac{1}{p_{T1}^2} \frac{\Delta R_{1j}^2}{R^2} < \frac{1}{p_{T1}^2} \qquad (5.3)$$

$$\implies \Delta R_{1j} < R. \qquad (5.4)$$

Therefore, a single high p_T particle (p_{T1}) surrounded by a bunch of low p_T particles results in a perfectly conical jet. This shape may change with the presence of other high momentum particles, but the key feature of the dynamics is that the jet shape is determined by high p_T objects due to the $\frac{1}{p_T}$ nature of this definition. In contrast, the k_T algorithm results in jets influenced by low momentum particles, which results in a less regular shape. This property, of regular jet shapes determined by high momentum objects, as well as demonstrated good practical performance, makes the anti-k_T algorithm the favored jet algorithm in ATLAS.

Because jets are composed of multiple objects, a useful property of jets is jet *substructure*, that is, acknowledging that jets are composite objects, analyzing the structure of a given jet to infer physics information. This leads to the use of *subjets*; that is, after running jet clustering, often to create a "large-R", $R = 1.0$ anti-k_T jet, a smaller radius jet clustering algorithm is run within the jet. Subjets are often chosen using the k_T algorithm, which again is sensitive to lower momentum particles, with $R = 0.2$ or 0.3. For the boosted version of this thesis analysis, such a strategy is used, in which the subjets are *variable radius* and depend on the momentum of the (proto)jet in question. Beyond this thesis work, substructure is used in a large variety of analyses, with a set of associated variables and tools developed for exploiting this structure *TODO: Cite some?*.

5.2 Flavor Tagging

For this this thesis, the physics process being considered is $HH \to b\bar{b}b\bar{b}$. From the previous section, we know that the standard practice is to identify these b quarks (or, rather, the resulting B hadrons, due to confinement) with jets – in our case, these *b-jets* are R=0.4 anti-k_T particle flow jets (see Chapter 7). However, not all jets produced at the LHC are from B hadrons; rather, there are a variety of different types of jets corresponding to different

flavors of quarks. These are often classified as light jets (from u, d, or s quarks, or gluons) or as other *heavy flavor* jets, e.g. *c*-jets, involving c quarks. Distinguishing between these different categories is a very active area of work in ATLAS, termed *flavor tagging*, with much focus on *b-tagging* in particular, that is, the identification of jets from B hadron decays. We here briefly describe the techniques used for flavor tagging in ATLAS.

What distinguishes a *b*-jet from any other jet? This question is fundamental to the design of the various *b*-tagging algorithms, and has two major answers: (1) B hadrons have long lifetimes, and (2) B hadrons have large masses. It is most illustrative to compare the B hadron properties to a common light meson, e.g. π^0, the neutral pion, with quark content $\frac{1}{\sqrt{2}}(u\bar{u} - d\bar{d})$. B hadrons have lifetimes around 1.5 ps, corresponding to a decay length $c\tau \approx 0.45$mm. In contrast, π^0 has a lifetime of 8.4×10^{-5}ps, which is around 20,000 times shorter! Theoretically, this comes from CKM suppresion of the b to c transition *TODO: check*, which dominates the B decay modes. Experimentally, this difference pops up as shown in Figure 5.1 – light flavor initiated jets decay almost immediately at the proton-proton interaction point, whereas b-jets are distinguished by a displaced secondary vertex, corresponding to the 5 mm decay length calculated above. This displaced vertex falls short of the detector itself, but may be inferred from larger transverse (perpendicular to beam) and longitudinal (parallel to beam) impact parameters of the resulting tracks, termed d_0 and z_0 respectively.

Coming to the mass, B mesons have masses of around 5.2 GeV, whereas the π^0 mass is around 0.134 GeV, (around 40 times lighter). This higher mass gives access to a larger decay phase space, leading to a high multiplicity for *b*-jets (average of 5 charged particles per decay).

One final distinguishing feature of B hadrons is their *fragmentation function*, a function describing the production of an observed final state. For B hadrons, this is particularly "hard", with the B hadrons themselves contributing to an average of around 75 % of the *b*-jet energy. Thus, the identification of *b*-jets with B hadrons is, in some sense, descriptive.

We have contrasted *b*-jets and light jets, demonstrating that there are several handles available for making this distinction. *c*-jets are slightly more similar to *b*-jets, but the same

handles still apply – c-hadron lifetimes are between 0.5 and 1 ps, a factor of 2 smaller than B hadrons. Their mass is around 1.9 GeV, 2 to 3 times smaller than B hadrons, and c-hadrons contribute to an average of around 55 % of c-jet energy. Therefore, while the gap is slightly smaller, a distinction may still be made.

The ATLAS flavor tagging framework [30] relies on developing a suite of "low-level" taggers, which use a variety of information about tracks and vertices as inputs. The output of these lower level taggers are then fed into a higher level tagger, which aggregates these results into a high level discriminant. Each of these taggers is described below.
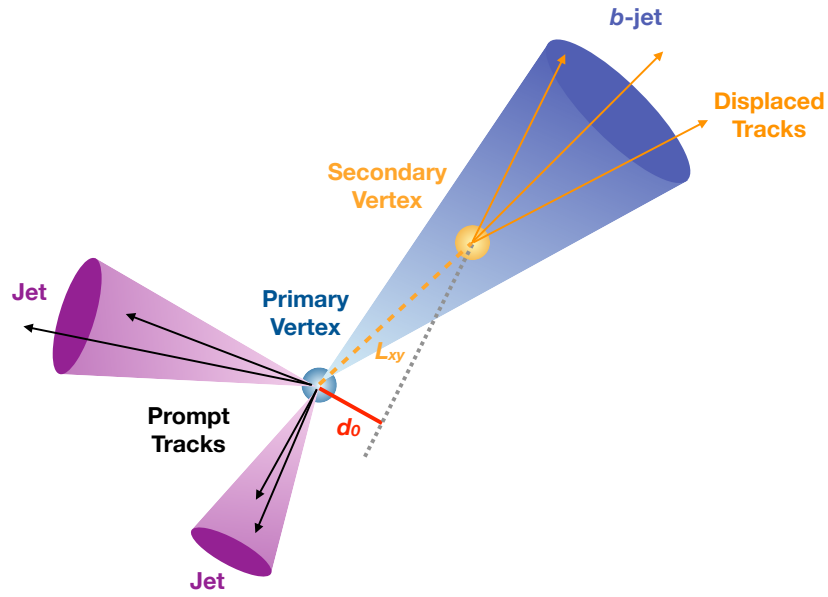
Figure 5.1: Illustration of an interaction producing two light jets and one b-jet in the transverse plane. While the light jets decay "promptly", coinciding with the primary vertex of the proton-proton interaction, the longer lifetime of B hadrons leads to a secondary decay vertex, displaced from the primary vertex by length L_{xy}. This is typically a few mm, and therefore is not directly visible in the detector, but leads to a large transverse impact parameter, d_0, for the resulting tracks. [29]

5.2.1 IP2D/3D

IP2D and IP3D are taggers based on the large track impact parameter (IP) nature of B hadron decays. Both are based on histogram templates derived from Monte Carlo simulation, which are used as probability density functions to construct log-likelihood discriminants. IP2D incorporates just the transverse impact parameter information using 1D histogram templates, whereas IP3D uses both transverse and longitudinal impact parameters in a 2D template, which accounts for correlations. Importantly, these are *signed* impact parameters, with sign based on the angle between the impact parameter and the considered jet – positive impact parameters are consistent with a track extrapolation in front of the jet (angle between impact parameter line and jet $< 90°$), and therefore more consistent with tracks originating from a displaced decay.

Rather than using the impact parameters directly, an impact parameter *significance* is used which incorporates an uncertainty on the impact parameter – tracks with a lower uncertainty but the same impact parameter will contribute more in the calculation. This signed significance is what is used to sample from the PDF templates, with the resulting discriminants the sum of probability ratios between given jet hypotheses over tracks associated to a given jet, namely $\sum_{i=1}^{N} \log \frac{p_b}{p_{light}}$ between b-jet and light jet hypotheses, where p_b and p_{light} are the per-track probabilities. Similar discriminants are defined between b- and c-jets and c and light jets. *TODO: show distributions?*

5.2.2 SV1

SV1 is an algorithm which aims to find a secondary vertex (SV) in a given jet. Operating on all vertices associated with a considered jet, the algorithm discards tracks based on a variety of cleaning requirements. It then proceeds to first construct all two-track vertices, and then iterates over all the tracks involved in these two track vertices to try to fit a single secondary vertex, which would then be identified with the secondary vertex from the b or c hadron decay. This fit proceeds by evaluating a χ^2 for the association of a track and vertex,

removing the track with the largest χ^2, and iterating until the χ^2 is acceptable and the vertex has an invariant mass of less than $6\,\mathrm{GeV}$ (for consistency with b or c hadron decay).

A variety of discriminating variables may then be constructed, including (1) invariant mass of the secondary vertex, (2) number of tracks associated with the secondary vertex, (3) number of two-track vertices, (4) energy fraction of the tracks associated to the secondary vertex (relative to all of the tracks associated to the jet), and various metrics associated with the secondary vertex position and decay length, including (5) transverse distance between the primary and secondary vertex, (6) distance between the primary and secondary vertex (7) distance between the primary and secondary vertex divided by its uncertainty, and (8) ΔR between the jet axis and the direction of the secondary vertex relative to the primary vertex.

While all eight of these variables are used as inputs to the higher level taggers, the number of two-track vertices, the vertex mass, and the vertex energy fraction are additionaly used with 3D histogram templates to evaluate flavor tagging performance by constructing log-likelihood discriminants, similar to the procedure for IP2D/3D.

5.2.3 JetFitter

Rather than focusing on a particular aspect of the B hadron or D hadron decay topology (e.g impact parameter or secondary vertex), the third low level tagger, JETFITTER [31], tries to reconstruct the full decay chain, including all involved vertices. This is structured around a Kalman filter formalism [32], and has the strong underlying assumption that all tracks which stem from B and D hadron decay must intersect a common flight path. This assumption provides significant constraints, allowing for the reconstruction of vertices from even a single track, reducing the number of degrees of freedom in the fit, and allowing the use of "downstream" information, e.g., compatibility of tracks with a $B \to D$-like decay. The constructed topology, including primary vertex location and B-hadron flight path, is iteratively updated over tracks associated to a given jet, and a variety of discriminating variables related to the resulting topology and reconstructed decay are used as inputs to the high level taggers.

5.2.4 RNNIP

The IP2D and IP3D algorithms rely on per-track probabilities, and the final discriminating variables (and inputs to the higher level taggers) are sums (products) over these independently considered quantities. In practice, however, the tracks are not independent – this is merely a simplifying assumption to allow for the use of a binned likelihood, as treatment of all of the interdependencies in such a framework quickly becomes intractable. To address this issue, a recurrent neural network-based algorithm, RNNIP [33], is used, which takes as input a variety of per-track variables, including the signed impact parameter significances (as in IP3D) as well as track momentum fraction relative to the jet and ΔR between the track and the jet. RNNs are sequence-based, and vectors of input variables corresponding to tracks for a given jet are ordered by magnitude of transverse impact parameter significance and then passed to the network, which outputs class probabilities corresponding to b-jet, c-jet, light-jet, and τ-jet hypotheses. Such a procedure allows the network to learn interdependencies between tracks, improving performance.

5.2.5 MV2 and DL1

Outputs from the above taggers are combined into high level taggers to aggregate all of the information and improve discriminating power relative to the respective individual taggers as, as shown in Figure 5.2. These high level taggers are primarily in two forms: MV2, which uses a Boosted Decision Tree (BDT) for this aggregation, and DL1, which uses a deep neural network. For the baseline versions of these taggers, only inputs from IP2D, IP3D, SV1, and JetFitter are used. The tagger used for this thesis analysis, DL1r, additionally incorporates RNNIP, demonstrating improved performance over the baseline DL1, as shown in Figure 5.3. All high level taggers also include jet p_T and $|\eta|$.

DL1 offers a variety of improvements over MV2. Rather than a single discriminant output, as with MV2, DL1 has a multidimensional output, corresponding to probabilities for a jet to be a b-jet, c-jet, or light jet. This allows the trained network to be used for both b- and c-jet

tagging. The final discriminant for b-tagging with DL1 correspondingly takes the form

$$D_{\text{DL1}} = \ln\left(\frac{p_b}{f_c \cdot p_c + (1 - f_c) \cdot p_{\text{light}}}\right) \tag{5.5}$$

where p_b, p_c, and p_{light} are the output b, c, and light jet probabilities, and f_c corresponds to an effective c-jet fraction, which may tuned to optimize performance.

DL1 further includes an additional set of JETFITTER input variables relative to MV2 which correspond to c-tagging – notably properties of secondary and tertiary vertices, as would be seen in a $B \rightarrow D$ decay chain.
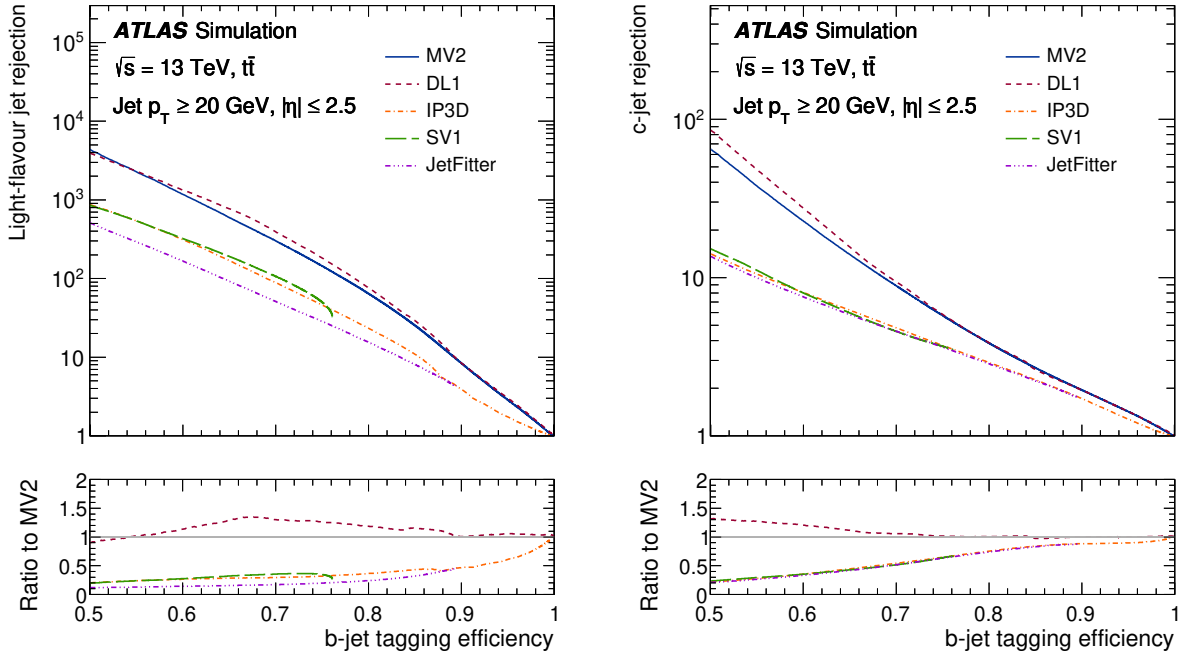
Figure 5.2: Performance of the various low and high level flavor tagging algorithms in $t\bar{t}$ simulation, demonstrating the tradeoff between b-jet efficiency and light and c-jet rejection. The high level taggers demonstrate significantly better performance than any of the individual low level taggers, with DL1 offering slight improvements over MV2 due to the inclusion of additional input variables.

Figure 5.2 shows a comparison of the performance of the various taggers. The b-tagging performance of DL1 and MV2 is found to be similar, with some improvements in light jet and c-jet rejection from the additional variables used in DL1. The performance of these high level taggers additionaly is seen to be significantly better than any of the individual low level ones, even in regimes where only a single low level tagger is relevant (such as high b-tagging efficiencies, where SV1 and JETFITTER are limited by selections on tracks entering the respective algorithms).

The inclusion of RNNIP offers a significant improvement on top of baseline DL1, as shown in Figure 5.3, strongly motivating the choice of DL1r for this thesis.
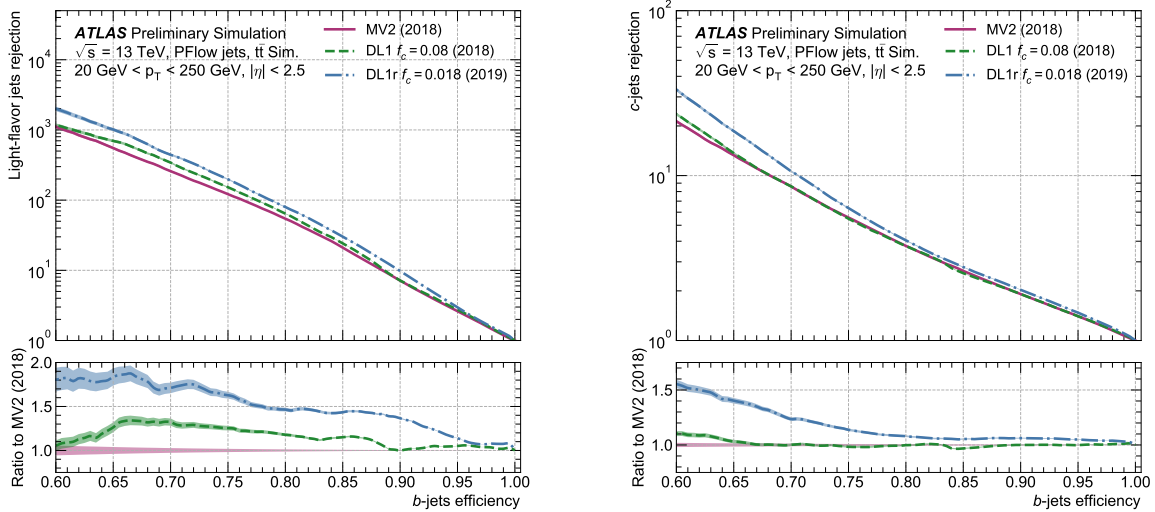
Figure 5.3: Performance of the MV2, DL1, and DL1r algorithms in $t\bar{t}$ simulation, demonstrating the tradeoff between b-jet efficiency and light and c-jet rejection. f_c controls the importance of c-jet rejection in the discriminating variable, and values shown have been optimized separately for each DL1 configuration. DL1r demonstrates a significant improvement in both light and c jet rejection over MV2 and DL1. [34]

5.2.6   Some Practical Notes

The b-tagging metrics presented in Figures 5.2 and 5.3 correspond to evaluating a tradeoff between b-jet efficiency and light jet and c-jet rejection. In this case, b-jet efficiency is defined such that, e.g. for a 77 % efficiency, 77 % of the real b-jets will be tagged as such. Somewhat counterintuitively, this means that a lower b-jet efficiency corresponds to a more aggressive ("tighter") selection on the discriminating variable, while a higher b-jet efficiency corresponds to a less aggressive ("looser") cut (100 % efficiency means no cut). Light and c jet efficiencies are defined similarly, with rejection defined as 1/ the corresponding efficiency.

In ATLAS, the respective b-tagging efficiencies are used to define various b-tagging working points. The working point used for the nominal b-jet identification in this thesis is 77 % with DL1r. A loosened (less aggressive) selection at the 85 % working point is additionally used. See Chapter 7 for further details.

Chapter 6

THE ANATOMY OF AN LHC SEARCH

In this thesis so far, we have set the theoretical foundation for the work carried out at the LHC. We have described how one may translate between this theoretical foundation and what we are actually able to observe with the ATLAS detector. We have further stepped through the process of simulating production of specific physics processes and their appearance in our detector, allowing us to describe how a hypothetical physics model would be seen in our experiment. The question then becomes: all of these pieces are on the table, what do we do with them? This chapter attempts to answer exactly that, setting up a roadmap for assembling these pieces into a statement about the universe.

6.1 Object Selection and Identification

As described in Chapter 5, there is a complicated set of steps for going from electrical signals in a detector to physics objects.

6.2 Defining a Signal Region

6.3 Background Estimation

6.4 Uncertainty Estimation

6.5 Hypothesis Testing

Chapter 7

SEARCH FOR PAIR PRODUCTION OF HIGGS BOSONS IN THE $b\bar{b}b\bar{b}$ FINAL STATE

This chapter presents two complementary searches for pair production of Higgs bosons in the final state. Such searches are separated based on the signal models being considered: resonant production, in which a new spin-0 or spin-2 particle is produced and decays to two Standard Model Higgs bosons, and non-resonant production, which is sensitive to the value of the Higgs self-coupling λ_{HHH}. Further information on the theory behind both channels can be found in Chapter *TODO: Fill in theory chapter.*

While the searches face many similar challenges and proceed (in broad strokes) in a very similar manner, separate optimizations are performed to maximize the respective sensitivities for these two very different sets of signal hypotheses. More particularly, resonant signal hypotheses are (1) very peaked in values of the mass of the HH candidate system near the value of the resonance mass considered and (2) considered across a very broad range of signal mass hypotheses. The resonant searches are therefore split into resolved and boosted topologies based on Lorentz boost of the decay products, with the resolved channel as one of the primary focuses of this thesis. Further, several analysis design decisions are made to allow for sensitivity to a broad range of masses – in particular, though sensitivity is limited at lower values of m_{HH} relative to other channels *TODO: Combination, bbyy* due to the challenging background topology, retaining and properly reconstructing these low mass events allows the $b\bar{b}b\bar{b}$ channel to retain sensitivity up until the kinematic threshold at $250\,\text{GeV}$.

In contrast, non-resonant signal hypotheses are quite broad in m_{HH}, and have a much more limited mass range, with Standard Model production peaking near $400\,\text{GeV}$, and the majority of the analysis sensitivity able to be captured with a resolved topology. Even for

Beyond the Standard Model signal hypotheses, which may have more events at low m_{HH}, the non-resonant nature of the production allows the $b\bar{b}b\bar{b}$ channel to retain sensitivity while discarding much of the challenging low mass background. Such freedom allows for decisions which focus on improved background modeling for the middle to upper HH mass regime, resulting in improved modeling and smaller uncertainties than would be obtained with a more generic approach.

Both searches are presented in the following, with emphasis on particular motivations for, and consequences of, the various design decisions involved for each respective set of signal hypotheses.

The analyses improve upon previous work *TODO: cite* in several notable ways. The resonant search leverages a Boosted Decision Tree (BDT) based pairing algorithm, offering improved HH pairing efficiency over a broad mass spectrum. The non-resonant adopts a different approach, with a simplified algorithm based on the minimum angular distance (ΔR) between jets in a Higgs candidate. Such an approach very efficiently discards low mass background events, resulting in an easier to estimate background with reduced systematic uncertainties.

A particular contribution of this thesis is the background estimation, which uses a novel, neural network based approach, offering improved modeling over previous methods, as well as the ability to model correlations between observables. While all aspects of the analysis of course contribute to the final result, the author of this thesis wishes to emphasize that the background estimate, with the corresponding uncertainties and all other associated decisions, really is the core of the $HH \to b\bar{b}b\bar{b}$ analysis – the development of this procedure, and all associated decisions, is similarly the core of this thesis work.

ATLAS has performed a variety of searches in complementary decay channels as well, notably in the $b\bar{b}\,W^+W^-$ [35], $b\bar{b}\tau^+\tau^-$ [36], $W^+W^-W^+W^-$ [37], $b\bar{b}\gamma\gamma$ [38], and $W^+W^-\gamma\gamma$ [39] final states, which were combined along with $b\bar{b}b\bar{b}$ in [40].

CMS has also performed searches for resonant production of Higgs boson pairs in the $b\bar{b}b\bar{b}$ final state (among others) at $\sqrt{s} = 8\,\text{TeV}$ [41] and $\sqrt{s} = 13\,\text{TeV}$ [42]. CMS have also

performed a combination of their searches in the $b\bar{b}b\bar{b}$, $b\bar{b}\tau^+\tau^-$, $b\bar{b}\gamma\gamma$, and $b\bar{b}VV$ channels in [43].

This analysis also benefits from improvements to ATLAS jet reconstruction and calibration, and flavour tagging [30]. In particular, this analysis benefits from the introduction of particle flow jets [24]. These make use of tracking information to supplement calorimeter energy deposits, improving the angular and transverse momentum resolution of jets by better measuring these quantities for charged particles in those jets.

The analysis also benefits from the new DL1r ATLAS flavour tagging algorithm. Whereas the flavour tagging algorithm used in the previous analysis (MV2) used a boosted decision tree (BDT) to combine the output of various low level algorithms, DL1r (and the baseline DL1 algorithm) uses a deep neural network to do this combination. In addition to the low level algorithms used as inputs to MV2, DL1 includes a variety of additional variables used for c-tagging. DL1r further incorporates RNNIP, a recurrent neural network designed to identify b-jets using the impact parameters, kinematics, and quality information of the tracks in the jets, while also taking into account the correlations between the track features.

The overall analysis sensitivity further benefits from a factor of ~4.6 increase in integrated luminosity.

7.1   Data and Monte Carlo Simulation

Both the resonant and non-resonant searches are performed on the full ATLAS Run 2 dataset, consisting of $\sqrt{s} = 13\,\mathrm{TeV}$ proton-proton collision data taken from 2016 to 2018 inclusive. Data taken in 2015 is not used due to a lack of trigger jet matching information and b-jet trigger scale factors. The integrated luminosity collected and usable in this analysis[1] was:

- $24.6\,\mathrm{fb}^{-1}$ in 2016

- $43.65\,\mathrm{fb}^{-1}$ in 2017

---

[1]approximately $9\,\mathrm{fb}^{-1}$ of data was collected but could not be used in this analysis due to an inefficiency in the b-jet triggers at the start of 2016 [44]

- $57.7\,\text{fb}^{-1}$ in 2018

This gives a total integrated luminosity of $126\,\text{fb}^{-1}$. This is lower than the $139\,\text{fb}^{-1}$ ATLAS collected during Run 2 [45] due to the inefficiency described in footnote 1 as well as the $3.2\,\text{fb}^{-1}$ of 2015 data which is unused due to the trigger scale factor issue mentioned above.

In this analysis, Monte Carlo samples are used purely for modelling signal processes. The background is strongly dominated by events produced by QCD multijet processes, which are difficult to correctly model in simulation. This necessitates the use of a data-driven background modelling technique, which is described in Section ??.

The scalar resonance signal model is simulated at leading order in α_s using MADGRAPH [10]. Hadronization and parton showering are done using HERWIG 7 [14][15] with EVTGEN [17], and the nominal PDF is NNPDF 2.3 LO. In practice this is implemented as a two Higgs doublet model where the new neutral scalar is produced through gluon fusion and required to decay to a pair of SM Higgs bosons. The heavy scalar is assigned a width much smaller than detector resolution, and the other 2HDM particles do not enter the calculation.

Scalar samples are produced at resonance masses between 251 and $900\,\text{GeV}$ and the detector simulation is done using AtlFast-II [19]. In addition the samples at $400\,\text{GeV}$ and $900\,\text{GeV}$ are also fully simulated to verify that the use of AtlFast-II is acceptable. For higher masses, as well as for the boosted analysis, samples are produced between 1000 and $5000\,\text{GeV}$, and the detector is fully simulated. As discussed in Chapter 4, an outstanding issue with AtlFast-II is the modeling of jet substructure. While such variables are not used for the resolved analysis, the boosted analysis begins at $900\,\text{GeV}$, motivating the different detector simulation in these two regimes.

The spin-2 resonance signal model is also simulated at LO in α_s using MADGRAPH. Hadronization and parton showering are done using PYTHIA 8 [16] with EVTGEN, and the nominal PDF is NNPDF 2.3 LO. In practice this is implemented as a Randall-Sundrum graviton with $c = 1.0$.

Spin-2 resonance samples are produced at masses between 251 and $5000\,\text{GeV}$, and these

samples are all produced with full detector simulation.

For the non-resonant search, samples are produced at values of $\kappa_\lambda = 1.0$ and 10.0, and are simulated using POWHEG BOX v2 generator [11–13] at next-to-leading order (NLO), with full NLO corrections with finite top mass, using the PDF4LHC [46] parton distribution function (PDF) set. Parton showers and hadronization are simulated with PYTHIA 8.

Alternative ggF samples are simulated at NLO using POWHEG BOX v2, but instead using HERWIG 7 [47] for parton showering and hadronization. The comparison between these two is used to assess an uncertainty on the parton showering.

7.2   Triggers and Object Definitions

To maximize analysis sensitivity, a combination of multi-b-jet triggers is used. Due to the use of events with two b-tagged jets in the background estimate, such triggers have a maximum requirement of two b-tagged jets. For the resonant analysis, a combination of triggers of various topologies is used, namely *TODO: describe*

- 2b + HT

- 2b + 2j

- 2b + 1j

- 1b

The non-resonant analysis uses a simplified strategy relying entirely on $2b + 1j$ and $2b + 2j$ triggers. *TODO: why?*

While the use of multiple triggers is beneficial for analysis sensitivity, it comes with some complications. Namely, a set of scale factors must be assigned to simulated events account for trigger inefficiencies in data *TODO: check*. Because these scale factors may differ between triggers, the use of multiple triggers becomes complicated: an event may pass more than one trigger, while trigger scale factors are only provided for individual triggers.

To simplify this calculation, a set of hierarchical offline selections is applied, closely mimicking the trigger selection. Based on these selections, events are sorted into categories (*trigger buckets*), after which the decision of a *single trigger* is checked.

The resonant search applies such categorization in the following way, with selections considered in order:

1. If the leading jet is b-tagged with $p_T > 325\,\text{GeV}$, the event is in the $1b$ trigger category.

2. Otherwise, if the leading jet is not b-tagged, but has $p_T > 168.75\,\text{GeV}$, the event is in the $2b + 1j$ trigger category.

3. If neither of the first two selections pass, if the scalar sum of jet p_Ts, $H_T > 900\,\text{GeV}$, the event falls into the $2b + HT$ trigger category.

4. Events that do not pass any of the above offline selections are in the $2b + 2j$ trigger category.

Corresponding triggers are then checked in each category, and the final set of events consists of those events that pass the trigger decision in their respective categories.

For the resonant search, the $2b + 1j$ and $2b + 2j$ triggers are the dominant categories, containing roughly 26 % and 49 % of spin-2 events, evaluated on MC16d samples with resonance masses between 300 and $1200\,\text{GeV}$. Notably, the $1b$ trigger efficiency is largest at high ($> 1\,\text{TeV}$) resonance masses.

For the non-resonant search, it was noted that the $1b$ trigger has minimal contribution, while the $2b + HT$ events are largely captured by the $2b + 2j$ trigger. Therefore, for, a simplified scheme is considered, with selections:

1. If the 1st leading jet has $p_T > 170\,\text{GeV}$ and the 3rd leading jet has $p_T > 70\,\text{GeV}$, the event is in the $2b + 1j$ trigger category.

2. Otherwise, the event is in the $2b + 2j$ trigger category.

7.3 Analysis Selection

After the trigger selections of Section 7.2, a variety of selections on the analysis objects are made, with the goal of (1) reconstructing a HH-like topology and (2) suppressing contributions from background processes.

Both analyses begin with a common pre-selection, requiring at least four $R = 0.4$ anti-k_T jets with $|\eta| < 2.5$ and $p_T > 40\,\mathrm{GeV}$. The $|\eta| < 2.5$ requirement is necessary for b-tagging due to the coverage of the ATLAS tracking detector (see Chapter 3) *TODO: check*, while the $p_T > 40\,\mathrm{GeV}$ requirement is motivated by the trigger thresholds *TODO: mention low pT*. At least two of the jets passing this pre-selection are required to be b-tagged, and additional b-tagging requirements are made to define the following regions:

- "2b Region": require exactly two b-tagged jets, used for background estimation

- "4b Region": require at least (but possibly more) four b-tagged jets, used as a signal region for both resonant and non-resonant searches

The non-resonant analysis additionally defines two 3b regions:

- "3b+1 loose Region": require exactly three b-tagged jets which pass the 77 % b-tagging working point (nominal) and one additional jet that fails the 77 % b-tagging working point but passes the *looser* 85 % b-tagging working point. Used as a signal region for the non-resonant search.

- "3b+1 fail Region": complement of 3b+1 loose. Require exactly three b-tagged jets which pass the 77 % b-tagging working point, but require that none of the remaining jets pass the 85 % b-tagging working point. Used as a validation region for the non-resonant search.

After these requirements, four jets are chosen, ranked first by b-tagging requirement and then by p_T (e.g. for the 2b region, the jets chosen are the two b-tagged jets and the two highest p_T

non-tagged jets; for the $4b$ region, the jets are the four highest p_T b-tagged jets). To match the topology of a $HH \to b\bar{b}b\bar{b}$ event, these four jets are then *paired* into *Higgs candidates*: the four jets are split into two sets of two, and each of these pairs is used to define a reconstructed object that is a proxy for a Higgs in a HH event. *TODO: Should pairAGraph go somewhere? Maybe a "future ideas" chapter*

For four jets there are three possible pairings. For signal events, a correct pairing can be identified (provided all necessary jets pass pre-selection) using the truth information of the Monte Carlo simulation, and such information may be used to design/select an appropriate pairing algorithm. This is only part of the story, however. The vast majority of the events in data do *not* include a real HH decay (this is a search for a reason!), either because the event originates from a background process (e.g. for $4b$ events), or because the selection is not designed to maximize the signal (e.g. $2b$ events). As the pairing is part of the selection, it must still be run on such events, such that various algorithms which achieve similar performance in terms of pairing efficiency may have vastly different impacts in terms of the shape of the background and the biases inherent in the background estimation procedure. The interplay between these two facets of the pairing is an important part of the choices made for this analysis.

A comparison of different shapes due to three different paring strategies is shown in Figure 7.1.

7.3.1 Resonant Pairing Strategy

For the resonant analysis, a Boosted Decision Tree (BDT) is used for the pairing. The boosted decision tree is given the total separation between the two jets in each of the two pairs (ΔR_1 and ΔR_2), the pseudo-rapidity separation between the two jets in each pair ($\Delta \eta_1$ and $\Delta \eta_2$), and the angular separation between the two jets in each pair in the $x - y$ plane ($\Delta \phi_1$ and $\Delta \phi_2$). The total separations (ΔRs) are provided in addition to the components in order to avoid requiring the boosted decision tree to reconstruct these variables in order to use them. For these variables, pair 1 is the pair with the highest scalar sum of jet p_Ts, and pair 2 the

other pair.

The boosted decision tree is also parameterized on the di-Higgs mass (m_{HH}) by providing this as an additional feature. Since the boosted decision tree is trained on correct and incorrect pairings in signal events, there will be exactly one correct pairing and two incorrect pairings in the training set for each m_{HH} value present in that set. As a result, this variable cannot, in itself, distinguish a correct pairing from an incorrect pairing, and therefore the inclusion of this variable simply serves to parameterize the BDT on m_{HH}[2].

The boosted decision tree was trained on one quarter of the total AFII simulated scalar MC statistics, using the Gradient-based One Side Sampling (GOSS) algorithm which allows rapid training with very large datasets. A preselection was applied requiring events to have four jets with a p_{T} of at least $35\,\mathrm{GeV}$. Note that this is a looser requirement than the $40\,\mathrm{GeV}$ used in the analysis selection, and is meant to increase the available statistics for events with low m_{HH} and to ensure a better performance as a function of that variable. Events were also required to have four distinct jets that could be geometrically matched (to within $\Delta R \leq 0.4$) to the b-quarks. The events used to train the BDT were not included when the analysis was run on these signal simulations. The boosted decision tree was constructed with the following hyperparameters:

```
min_data_in_leaf=50,
num_leaves=180,
learning_rate=0.01
```

These hyperparameters were optimized using a Bayesian optimization procedure [48]. Three fold cross-validation was used to perform this optimization without the need for an additional sample, while avoiding over-training on signal events.

---

[2]That is, the conditions placed on the other variables by the BDT vary with m_{HH}.

7.3.2   Non-resonant Pairing Strategy

For the non-resonant analysis, a simpler pairing algorithm is used, which proceeds as follows: in a given event, Higgs candidates for each possible pairing are sorted by the p_T of the vector sum of constituent jets. The angular separation, ΔR is computed between jets in the each of the leading Higgs candidates, and the pairing with the smallest separation (ΔR_{jj}) is selected. This method will be referred to as $\min \Delta R$ in the following.

The primary motivation for the use of this pairing in the non-resonant search is a *smooth mass plane*: by efficiently discarding low mass events, $\min \Delta R$ removes the background peak present in the resonant search while maintaining good pairing efficiency for the non-resonant signal. This facilitates a background estimate with small kinematic bias – the region in which the background estimate is derived is more similar to the signal region.

Along with discarding low mass background, there is a corresponding loss of low mass signal. In particular *TODO: insert plot*, for higher κ_λ points, in which the *TODO: check - I think it's triangle diagram?* dominates, there is a significant impact on the resulting signal distribution. *TODO: put in combination plot?* The $4b$ channel has the strongest contribution near the Standard Model, however, and is optimized as such. Further, because of the large low mass background, the loss of significance is mitigated. This approach is thus adopted for the non-resonant search.

(a) BDT pairing

(b) $\min \Delta R$ pairing

(c) D_{HH} pairing
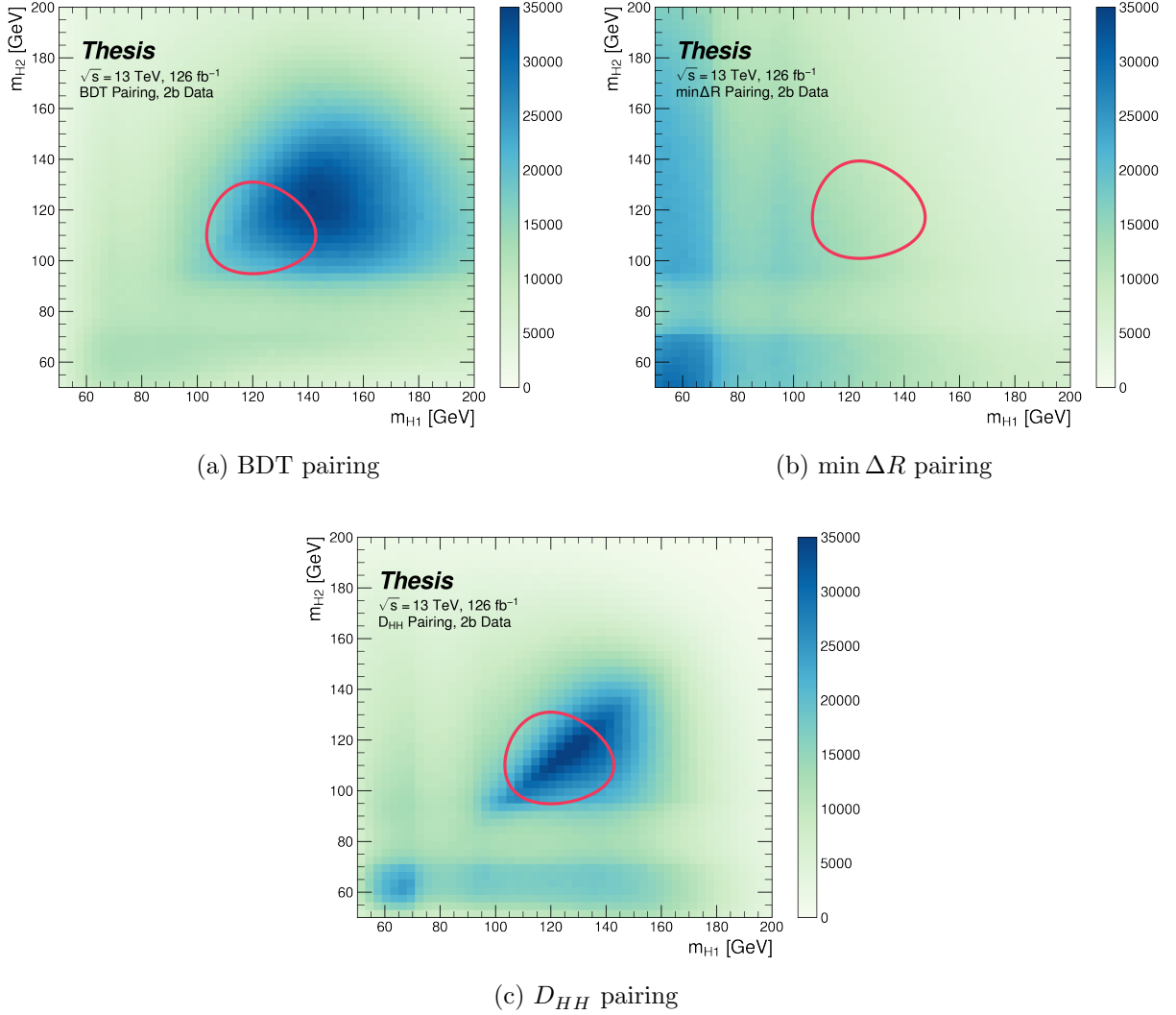
Figure 7.1: Comparison of m_{H1} vs m_{H2} planes for the full Run 2 2b dataset with different pairings. As evidenced, this choice significantly impacts where events fall in this plane, and therefore which events fall into the various kinematic regions defined in this plane (see Section 7.5). Respective signal regions are shown for reference, with the $\min \Delta R$ signal region shifted slightly up and to the right to match the non-resonant selection. Note that the band structure around $80\,\mathrm{GeV}$ in both m_{H1} and m_{H2} is introduced by the top veto described in Section 7.4.
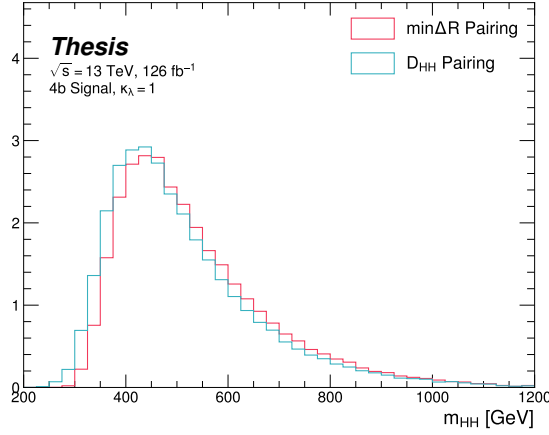
(a) $\kappa_\lambda = 1$ (SM)
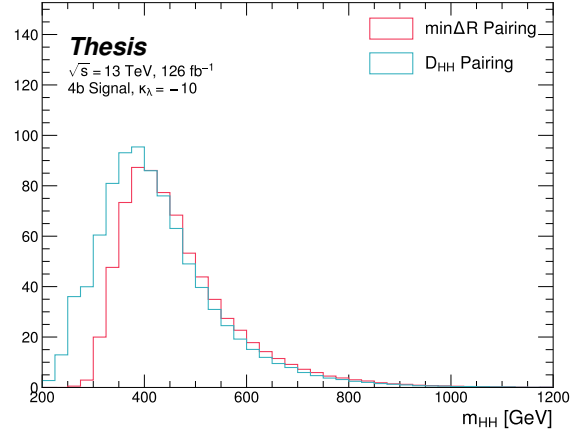
(b) $\kappa_\lambda = -10$
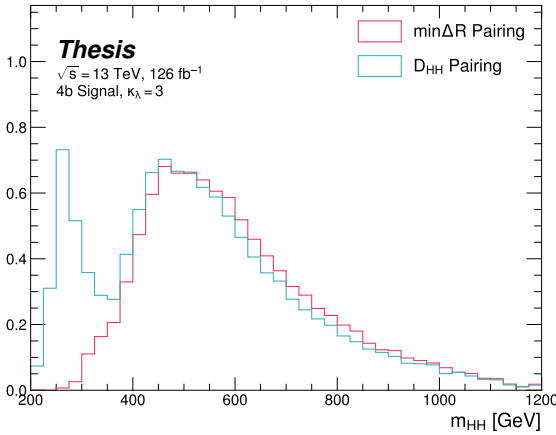
(c) $\kappa_\lambda = 3$
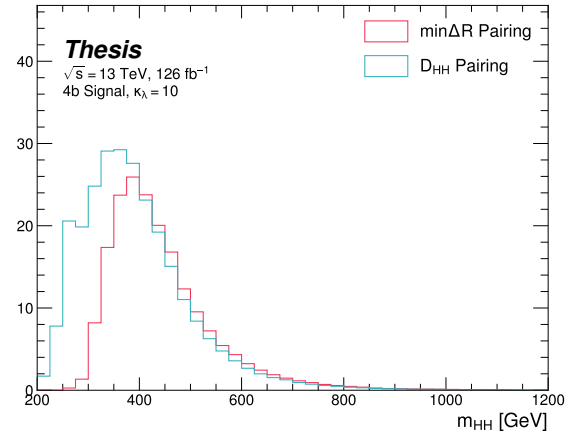
(d) $\kappa_\lambda = 10$

Figure 7.2: Comparison of signal distributions in the respective signal regions for the $\min \Delta R$ and D_{HH} pairing for various values of the Higgs trilinear coupling in the respective signal regions. The distributions are quite similar at the Standard Model point, but for other variations, $\min \Delta R$ does not pick up the low mass features.

7.4   Background Reduction and Top Veto

Choosing a pairing of the four b-tagged jets fully defines the di-Higgs candidate system used for each event in the remainder of the analysis chain. A requirement of $\left|\Delta\eta_{HH}\right| < 1.5$ on this di-Higgs candidate system mitigates QCD multijet background.

Figure **??** illustrates this variable in the validation region (see Section **??**). It demonstrates that this selection rejects only a small fraction of signal, but a significant fraction of data (which, in the validation region, is a good approximation of pure background).

In order to mitigate the hadronic $t\bar{t}$ background, a top veto is then applied, removing events consistent with a $t \to b(W \to q_1\bar{q}_2)$ decay.

The jets in the event are separated into *HC jets* which are the four jets used to build the Higgs candidates, and *non-HC jets*, the other jets (passing the p_T and $|\eta|$ requirements) in the event.

W candidates are built by forming all possible pairs of all jets in each event. With n jets, there are $\binom{n}{2}$ such pairs. t candidates are then built by pairing each W candidate with each HC jet (for $4\binom{n}{2}$ combinations). Note that all jets in a t candidate must be distinct (i.e. a HC jet may not be used both on its own and in a W candidate).

With m_t denoting the invariant mass of the t candidate, and m_W the invariant mass of the W candidate, the quantity

$$X_{Wt} = \sqrt{\left(\frac{10\left(m_W - 80.4\,\mathrm{GeV}\right)}{m_W}\right)^2 + \left(\frac{10\left(m_t - 172.5\,\mathrm{GeV}\right)}{m_t}\right)^2} \qquad (7.1)$$

is constructed for each combination.

Events are then vetoed if the minimum X_{Wt} over all combinations is less than 1.5.

The same definitions and procedures are used for both the resonant and non-resonant analyses. However, for the non-resonant search, the top candidates considered for X_{Wt} have the additional requirement that the jet used for the b is b-tagged. While this is identical to the resonant analysis by definition for 4b events, it does change the set of events considered in lower tag regions, in particular for the 2b events considered in the derivation of the background

estimate. Such a change is found to reduce the impact of background systematics by increasing $2b$ support in the high X_{Wt} kinematic region. *TODO: Insert plot*

7.5   Kinematic Region Definition

As has been mentioned, an important piece of the analysis is the plane defined by the two Higgs candidate masses (the *Higgs candidate mass plane*). After the selection described above, a signal region is defined by requiring $X_{HH} < 1.6$, where:

$$X_{HH} = \sqrt{\left(\frac{m(H_1) - c_1}{0.1 \cdot m(H_1)}\right)^2 + \left(\frac{m(H_2) - c_2}{0.1 \cdot m(H_2)}\right)^2} \tag{7.2}$$

with $m(H_1)$, $m(H_2)$ the leading and subleading Higgs candidate masses, c_1 and c_2 correspond to the center of the signal region, and the denominator provides a Higgs candidate mass dependent resolution of 10 %. For consistency with the HH decay hypothesis, c_1 and c_2 are nominally (125 GeV, 125 GeV). However, these are allowed to vary due to energy loss, with specific values chosen described below. The selection of these values is one of several significant differences between the regions defined for the resonant and non-resonant search. We describe both below.

7.5.1   Resonant Kinematic Regions

For the resonant analysis, the signal region is centered at (120 GeV, 110 GeV) to account for energy loss leading to the Higgs masses being under-reconstructed. *TODO: insert signal location plot?* Note that leading and subleading Higgs candidates are defined according to the *scalar sum* of constituent jet p_T.

For the background estimation, two regions are defined which are roughly concentric around the signal region: a *validation region* which consists of those events not in the signal region, but which do pass

$$\sqrt{(m(H_1) - 1.03 \times 120\,\text{GeV})^2 + (m(H_2) - 1.03 \times 110\,\text{GeV})^2} < 30\,\text{GeV} \tag{7.3}$$

and a *control region* whcih consists of those events not in the signal or validation regions, but which do pass

$$\sqrt{(m(H_1) - 1.05 \times 120\,\text{GeV})^2 + (m(H_2) - 1.05 \times 110\,\text{GeV})^2} < 45\,\text{GeV} \tag{7.4}$$

For simplicity, the *TODO: cite old paper* SR/VR/CR definitions were chosen for the resonant analysis, but were found to be close to optimal.

7.5.2 Non-resonant Kinematic Regions

For the non-resonant analysis the signal region is centered at $(124\,\text{GeV}, 117\,\text{GeV})$, corresponding to the means of *correctly paired* Standard Model signal events. The shape of the signal region (other than this change of center) was found to remain optimal.

For the non-resonant search, leading and subleading Higgs candidates are defined according to the *vector sum* of constituent jet p_T, more closely corresponding to the $1 \rightarrow 2$ decay assumption behind the $\min \Delta R$ pairing algorithm.

Two areas for improvement were identified in the resonant analysis, which will be discussed in more detail below: *signal contamination* of the validation region (which impacts the uncertainty assessed due to extrapolation) and *large nuisance parameter pulls* on this uncertainty, corresponding to a rough assumption that the validation region is closer to the signal region in the mass plane, and so offers a better estimate of the signal region.

To mitigate these two issues, a redesign of the control and validation regions was performed for the non-resonant analysis. The outer boundary defined by the shifted resonant control region:

$$\sqrt{\left(m(H_1) - 1.05 \times 124\,\text{GeV}\right)^2 + \left(m(H_2) - 1.05 \times 117\,\text{GeV}\right)^2} < 45\,\text{GeV} \qquad (7.5)$$

is kept, rougly corresponding to combining the regions used for the resonant analysis. In order to assess the variation of the background estimate, two sets of regions are desired, so this combined region is split into *quadrants*, that is, divided into four pieces along axes that intersect with the signal region center. To avoid kinematic bias, quadrants on opposite sides of the signal region are paired, with these pairs corresponding to the non-resonant control and validation regions.

The particular orientation of the regions is chosen such that region centers align with the leading and subleading Higgs candidate masses, corresponding to a set of axes rotated at

45°, with the "top" and "bottom" quadrants together comprising the control region, and the other set ("left" and "right") the validation region.

This design of regions includes a set of events closer to the signal region in the mass plane, leveraging the assumption that these events are more similar to signal region events, while also including events further away from the signal region, mitigating signal contamination. This region selection is found to have good performance in alternate validation regions. *TODO: add more studies probs*

7.5.3 Discriminating Variable

The discriminant used for the resonant analysis is *corrected* m_{HH}. This variable is calculated by re-scaling the Higgs candidate four vectors such that each $m_H = 125\,\mathrm{GeV}$. These re-scaled four-vectors are then summed, and their invariant mass is the corrected m_{HH}. These re-scaled four-vectors are not used for any other purpose. The effect of this correction, which sharpens the m_{HH} peak and correctly centres it, is shown in Figure **??**.

For the non-resonant analysis, due to the broad nature of the signal in m_{HH}, such a correction is not as motivated, and, indeed, is found to have very minimal impact. The uncorrected m_{HH} (just referred to as m_{HH}) is therefore used as a discriminant. To maximize sensitivity, the non-resonant analysis additionally uses two variables for categorization: $\Delta\eta_{HH}$, an angular variable which, along with m_{HH}, fully characterizes the HH system *TODO: ref costhetastar paper?*, and X_{HH}, the variable used for the signal region definition, which leverages the peaked structure of the signal in the $(m(H_1), m(H_2))$ plane to split the signal extraction fit into lower and higher purity regions (highest purity near $X_{HH} = 0$, the center of the signal region). Distributions of these variables are shown in *TODO: plots*

7.6 Background Estimation

After the event selection described in Section **??** there are two major backgrounds, QCD and $t\bar{t}$. A very similar approach is used for both the resonant and the non-resonant analyses, with some small modifications. This approach is notably fully data-driven, which is warranted due to the flexibility of the estimation method, as well as the high relative proportion of QCD background (> 90 %), and allows for the use of machine learning methods in the construction of the background estimate. However, it sacrifices an explicit treatment of the $t\bar{t}$ component. Performance of the background estimate on the $t\bar{t}$ component is checked explicitly *TODO: add plots*, and minimal impact due to $t\bar{t}$ mismodeling is seen.

TODO: Port over some checks Contributions of single Higgs processes to the background are checked in Appendix **??**. ZZ and HH backgrounds are checked in Appendix **??**. All are found to be negligible.

The foundation of the background estimate lies in the derivation of a reweighting function which matches the kinematics of events with exactly two b-tagged jets to those of events in the higher tagged regions (events with three or four b-tagged jets). The reweighting function and overall normalization are derived in the control region. Systematic bias of this estimate is assessed in the validation region.

For the resonant analysis, the systematic bias is a bias due to extrapolation: the validation region lies between the control and signal regions. For the non-resonant analysis, the bias instead comes from different possible interpolations of the signal region kinematics – given the choice of nominal estimate, the validation region is a conceptually equivalent, but maximally different, signal region estimate.

7.6.1 The Two Tag Region

Events in data with exactly two b-tagged jets are used for the data driven background estimate. The hypothesis here is that, due to the presence of multiple b-tagged jets, the kinematics of such events are similar to the kinematics of events in higher b-tagged regions (i.e.

events with three and four b-tagged jets, respectively), and any differences can be corrected by a reweighting procedure. The region with three b-tagged jets is split into two b-tagging regions, with the $3b + 1$ loose region used as an additional signal region (see Section *TODO: Add ref*). The lower tagged $3b$ component ($3b + 1$ fail, as described in Section **??**) is reserved for validation of the background modelling procedure. Events with fewer than two b-tagged jets are not used for this analysis, as they are relatively more different from the higher tag regions.

The nominal event selection requires at least four jets in order to form Higgs candidates. For the four tag region, these are the four highest p_T b-tagged jets. For the three tag regions, these jets are the three b-tagged jets, plus the highest p_T jet satisfying a loosened b-tagging requirement. Similarly, and following the approach of the resonant analysis, the two tag region uses the two b-tagged jets and the two highest p_T non-tagged jets to form Higgs candidates. Combinatoric bias from selection of different numbers of b-tagged jets is corrected as a part of the kinematic reweighting procedure through the reweighting of the total number of jets in the event. In this way, the full event selection may be run on two tagged events.

7.6.2 Kinematic Reweighting

The set of two tagged data events is the fundamental piece of the data driven background estimate. However, kinematic differences from the four tag region exist and must be corrected in order for this estimate to be useful. Binned approaches based on ratios of histograms (*TODO: Cite either 15+16 or full Run 2 VBF*) have been previously considered, but are limited in their handling of correlations between variables and by the "curse of dimensionality", i.e. the dataset becomes sparser and sparser in "reweighting space" as the number of dimensions in which to reweight increases, limiting the number of variables used for reweighting. This leads either to an unstable fit result (overfitting with finely grained bins) or a lower quality fit result (underfitting with coarse bins).

Note that even machine learning methods such as Boosted Decision Trees (BDTs), may suffer from this curse of dimensionality, as the depth of each decision tree used is limited

by the available statistics after each set of corresponding selections (cf. binning in a more sophisticated way), limiting the expressivity of the learned reweighting function.

To solve these issues, a neural network based reweighting procedure is used here, following the success of the method used for the resonant search [**Abbott:2708605**]. This is a truly multivariate approach, allowing for proper treatment of variable correlations. It further overcomes the issues associated with binned approaches by learning the reweighting function directly, allowing for greater sensitivity to local differences and helping to avoid the curse of dimensionality.

Neural Network Reweighting

Let $p_{4b}(x)$ and $p_{2b}(x)$ be the probability density functions for four and two tag data respectively across some input variables x. The problem of learning the reweighting function between two and four tag data is then the problem of learning a function $w(x)$ such that

$$p_{2b}(x) \cdot w(x) = p_{4b}(x) \tag{7.6}$$

from which it follows that

$$w(x) = \frac{p_{4b}(x)}{p_{2b}(x)}. \tag{7.7}$$

This falls into the domain of density ratio estimation, for which there are a variety of approaches. The method considered here is modified from [49, 50], and depends on a loss function of the form

$$\mathcal{L}(R(x)) = \mathbb{E}_{x \sim p_{2b}}[\sqrt{R(x)}] + \mathbb{E}_{x \sim p_{4b}}[\frac{1}{\sqrt{R(x)}}]. \tag{7.8}$$

where $R(x)$ is some estimator dependent on x and $\mathbb{E}_{x \sim p_{2b}}$ and $\mathbb{E}_{x \sim p_{4b}}$ are the expectation values with respect to the 2b and 4b probability densities. A neural network trained with such a loss function has the objective of finding the estimator, $R(x)$, that minimizes this loss. It is straightforward to show (Appendix **??**) that

$$\arg \min_R \mathcal{L}(R(x)) = \frac{p_{4b}(x)}{p_{2b}(x)} \tag{7.9}$$

which is exactly the form of the desired reweighting function.

In practice, to avoid imposing explicit positivity constraints, the substitution $Q(x) \equiv \log R(x)$ is made. The loss function then takes the equivalent form

$$\mathcal{L}(Q(x)) = \mathbb{E}_{x \sim p_{2b}}[\sqrt{e^{Q(x)}}] + \mathbb{E}_{x \sim p_{4b}}[\frac{1}{\sqrt{e^{Q(x)}}}], \tag{7.10}$$

with solution

$$\arg\min_Q \mathcal{L}(Q(x)) = \log \frac{p_{4b}(x)}{p_{2b}(x)}. \tag{7.11}$$

Taking the exponent then results in the desired reweighting function.

Note that similar methods for density ratio estimation are available *TODO: cite*, e.g. from a more standard binary cross-entropy loss. However, these were found to perform no better than the formulation presented here.

Variables and Results

The neural network is trained on a variety of variables sensitive to two vs. four tag differences. To help bring out these differences, the natural logarithm of some of the variables with a large, local change is taken. The set of training variables used for the resonant analysis is

1. $\log(p_T)$ of the 4th leading Higgs candidate jet

2. $\log(p_T)$ of the 2nd leading Higgs candidate jet

3. $\log(\Delta R)$ between the closest two Higgs candidate jets

4. $\log(\Delta R)$ between the other two Higgs candidate jets

5. Average absolute value of Higgs candidate jet η

6. $\log(p_T)$ of the di-Higgs system.

7. ΔR between the two Higgs candidates

8. $\Delta\phi$ between the jets in the leading Higgs candidate

9. $\Delta\phi$ between the jets in the subleading Higgs candidate

10. $\log(X_{Wt})$, where X_{Wt} is the variable used for the top veto

11. Number of jets in the event.

The non-resonant analysis uses an identical set of variables with two notable changes

1. The definition of X_{Wt} differs from the resonant definition (as described in Section *TODO: ref*)

2. An integer encoding of the two trigger categories is used as an input (variable which takes on the value 0 or 1 corresponding to each of the two categories). This was found to improve a mismodeling near the tradeoff in m_{HH} of the two buckets.

The neural network used for both resonant and non-resonant reweighting has three densely connected hidden layers of 50 nodes each with ReLU activation functions and a single node linear output. This configuration demonstrates good performance in the modelling of a variety of relevant variables, including m_{HH}, when compared to a range of networks of similar size.

In practice, a given training of the reweighting neural network is subject to variation due to training statistics and initial conditions. An uncertainty is assigned to account for this (Section **??**), which relies on training an ensemble of reweighting networks [51]. To increase the stability of the background estimate, the median of the predicted weight for each event is calculated across the ensemble. This median is then used as the nominal background estimate. This approach is indeed seen to be much more stable and to demonstrate a better overall performance than a single arbitrary training. Each ensemble used for this analysis consists of 100 neural networks, trained as described in Section **??**.

The training of the ensemble used for the nominal estimate is done in the kinematic Control Region. The prediction of these networks in the Signal Region is then used for

the nominal background estimate. In addition, a separate ensemble of networks is trained in the Validation Region. The difference between the prediction of the nominal estimate and the estimate from the VR derived networks in the Signal Region is used to assign a systematic uncertainty associated with extrapolating in the Higgs Candidate mass plane. Further details on this systematic uncertainty are shown in Section **??**. Note that although the same procedure is used for both Control and Validation Region trained networks, only the median estimate from the VR derived reweighting is used for assessing a systematic – no additional "uncertainty on the uncertainty" from VR ensemble variation is applied.

Each reweighted estimate is normalized such that the reweighted $2b$ yield matches the $4b$ yield in the corresponding training region. Note that this applies to each of the networks used in each ensemble, where the normalization factor is also subject to the procedure described in Section **??**. As the median over these normalized weights is not guaranteed to preserve this normalization, a further correction is applied such that the $2b$ yield, after the median weights are applied, matches the $4b$ yield in the corresponding training region. As no preprocessing is applied to correct for the class imbalance between $2b$ and $4b$ events entering the training, this ratio of number of $4b$ events ($n(4b)$) over number of $2b$ events ($n(2b)$) is folded into the learned weights. Correspondingly, the set of normalization factors described above is near 1 and the learned weights are centered around $n(4b)/n(2b)$ (roughly 0.01 over the full dataset). This normalization procedure applies for all instances of the reweighting (e.g. those used for validations in Section **??**), with appropriate substitutions of reweighting origin (here $2b$) and reweighting target (here $4b$).

Note that, due to different trigger and pileup selections during each year, the reweighting is trained on each year separately. An approach of training all of the years together with a one-hot encoding was explored *TODO: reference study*, but was found to have minimal benefit over the split years approach, and in fact to increase the systematic bias of the corresponding background estimate. Because of this, and because trigger selections for each year significantly impact the kinematics of each year, such that categorizing by year is expected to reflect groupings of kinematically similar events and to provide a meaningful degree of freedom in

the signal extraction fit, the split-year approach is kept.

7.7 Uncertainties

A variety of uncertainties are assigned to account for known biases in the underlying methods, calibrations, and objects used for this analysis. The largest such uncertainty is associated with the kinematic bias inherent in deriving the background estimate away from the signal region. However, a statistical biasing of this same estimate has an effect of a similar magnitude. Additionally, due to the use of Monte Carlo for signal modelling and b-tagging calibration, uncertainties related to mismodellings in simulation must also be accounted for. These components, and their impact on this analysis, are described here in detail. Relative magnitudes of the uncertainties for each year are shown in Tables **??**, **??**, and **??** along with an estimate of the impact of the statistics of 4b data in the signal region on the total error. Note that, while the Poisson error (from 2b data statistics) is negligible relative to the bootstrap error in the bulk of the distribution, it becomes relevant in the high m_{HH} tail. The final statistical uncertainty used for the limit setting is therefore the sum (in quadrature) of these two components.

7.7.1 Statistical Uncertainties and Bootstrapping

There are two components to the statistical error for the neural network background estimate. The first is standard Poisson error, i.e., a given bin, i, in the background histogram has value $n_i = \sum_{j \in i} w_j$, where w_j is the weight for an event j which falls in bin i. Standard techniques then result in statistical error $\delta n_i = \sqrt{\sum_{j \in i} w_j^2}$, which reduces to the familiar $\sqrt{N}$ Poisson error when all w_j are equal to 1.

However, this procedure does not take into account the statistical uncertainty on the w_j due to the finite training dataset. Due to the large size difference between the two tag and four tag datasets, it is the statistical uncertainty due to the four tag training data that dominates that on the background. A standard method for estimating this uncertainty is the bootstrap resampling technique [52]. Conceptually, a set of statistically equivalent sets is constructed by sampling with replacement from the original training set. The reweighting

network is then trained on each of these separately, resulting in a set of statistically equivalent background estimates. Each of these sets is below referred to as a replica.

In practice, as the original training set is large, the resampling procedure is able to be simplified through the relation $\lim_{n\to\infty} \text{Binomial}(n, 1/n) = \text{Poisson}(1)$, which dictates that sampling with replacement is approximately equivalent to applying a randomly distributed integer weight to each event, drawn from a Poisson distribution with a mean of 1.

Though the network configuration itself is the same for each bootstrap training, the network initialization is allowed to vary. It should therefore be noted that the bootstrap uncertainties implicitly capture the uncertainty due to this variation in addition to the previously mentioned training set variation.

The variation from this bootstrapping procedure is used to assign a bin-by-bin uncertainty which is treated as a statistical uncertainty in the fit. Due to practical constraints, a procedure for approximating the full bootstrap error band is developed which demonstrates good agreement with the full bootstrap uncertainty. This procedure is described below.

Calculating the Bootstrap Error Band

The standard procedure to calculate the bootstrap uncertainty would proceed as follows: first, each network trained on each bootstrap replica dataset would be used to produce a histogram in the variable of interest. This would result in a set of replica histograms (e.g. for 100 bootstrap replicas, 100 histograms would be created). The nominal estimate would then be the mean of bin values across these replica histograms, with errors set by the corresponding standard deviation.

In practice, such an approach is inflexible and demanding both in computation and in storage, in so far as we would like to produce histograms in many variables, with a variety of different cuts and binnings. This motivates a derivation based on event-level quantities. However, due to non-trivial correlations between replica weights, simple linear propagation of event weight variation is not correct.

We therefore adopt an approach which has been empirically found to produce results

(for this analysis) in line with those produced by generating all of the histograms, as in the standard procedure. This approach is described below. Note that, for robustness to outliers and weight distribution asymmetry, the median and interquartile range (IQR) are used for the central value and width respectively (as opposed to the mean and standard deviation).

The components involved in the calculation have been mentioned in Section **??** and are as follows:

1. Replica weight (w_i): weight predicted for a given event by a network trained on replica dataset i.

2. Replica norm (α_i): normalization factor for replica i. This normalizes the reweighting prediction of the network trained on replica dataset i to match the correponding target yield.

3. Median weight (w_{med}): median weight for a given event across replica datasets, used for the nominal estimate. Defined (for 100 bootstrap replicas) as

$$w_{med} \equiv \text{median}(\alpha_1 w_1, \ldots \alpha_{100} w_{100}) \tag{7.12}$$

4. Normalization correction (α_{med}): normalization factor to match the predicted yield of the median weights (w_{med}) to the target yield in the training region.

As mentioned in Section **??**, the *nominal estimate* is constructed from the set of median weights and the normalization correction, i.e. $\alpha_{med} \cdot w_{med}$.

For the bootstrap error band, a "varied" histogram is then generated by applying, for each event, a weight equal to the median weight (with no normalization correction) plus half the interquartile range of the replica weights: $w_{varied} = w_{med} + \frac{1}{2} \text{IQR}(w_1, \ldots, w_{100})$.

This varied histogram is scaled to match the yield of the nominal estimate. To account for variation of the nominal estimate yield, a normalization variation is calculated from the interquartile range of the replica norms: $\frac{1}{2} \text{IQR}(\alpha_1, \ldots, \alpha_{100})$. This variation, multiplied into the nominal estimate, is used to set a baseline for the varied histogram described above.

Denoting $H(\text{weights})$ as a histogram constructed from a given set of weights, $Y(\text{weights})$ as the predicted yield for a given set of weights, the final varied histogram is thus:

$$H(w_{med}+\frac{1}{2}\text{IQR}(w_1,\ldots,w_{100}))\cdot\frac{Y(\alpha_{med}w_{med})}{Y(w_{med}+\frac{1}{2}\text{IQR}(w_1,\ldots,w_{100}))}+\frac{1}{2}\text{IQR}(\alpha_1,\ldots,\alpha_{100})\cdot H(\alpha_{med}w_{med})$$

$$(7.13)$$

where the first term roughly describes the behaviour of the bootstrap variation across the distribution of the variable of interest while the second term describes the normalization variation of the bootstrap replicas.

The difference between the varied histogram and the nominal histogram is then taken to be the bootstrap statistical uncertainty on the nominal histogram.

Figure *TODO: include figure* demonstrates how each of the components described above contribute to the uncertainty envelope for the 2017 Control Region and compares this approximate band to the variation of histograms from individual bootstrap estimates. The error band constructed from the above procedure is seen to provide a good description of the bootstrap variation.

7.7.2   *Background Shape Uncertainties*

To account for the systematic bias associated with deriving the reweighting function in the control region and extrapolating to the signal region, an alternative background model is derived in the validation region. Because of the fully data-driven nature of the background model, this is an uncertainty assessed on the full background. The alternative model and the baseline are consistent with the observed data in their training regions and with each other, and differences between the alternative and baseline models are used to define a shape uncertainty on the m_{HH} spectrum, with a two-sided uncertainty defined by symmetrizing the difference about the baseline.

For the resonant analysis, this uncertainty is split into two components to allow for two independent variations of the m_{HH} spectrum: : a low-H_T and a high-H_T component, where H_T is the scalar sum of the p_T of the four jets constituting the Higgs boson candidates, and

serves as a proxy for m_{HH}, while avoiding introducing a sharp discontinuity. The boundary value is $300\,\text{GeV}$. The low-H_T shape uncertainty primarily affects the m_{HH} spectrum below $400\,\text{GeV}$ (close to the kinematic threshold) by up to around 5%, and the high-H_T uncertainty mainly m_{HH} above this by up to around 20% relative to nominal. These separate m_{HH} regimes are by design – the H_T split is introduced to prevent low mass bins from constraining the high mass uncertainty and vice-versa.

This was the *status quo* shape uncertainty decomposition from the Early Run 2 analysis. A decomposition in terms of orthogonal polynomials, which would provide increased flexibility, was also evaluated. This study revealed that both decompositions are able to account for the systematic deviations between four tag data and the background estimate (evaluated in the kinematic validation region), and produce almost identical limits. This study is fully described in Appendix **??**.

The simpler *status quo* decomposition is therefore kept, with the technical ability to use the alternative decomposition for validation if necessary.

For the non-resonant analysis, the quadrant nature of the background estimation leads to a natural breakdown of the nuisance parameters: quadrants are defined in the signal region along the same axes as those used for the control and validation region definitions. Variations are then assessed in each of these signal region quadrants, corresponding to regions that are "closer to" and "further away from" the nominal and alternate estimate regions, fully leveraging the power of the two equivalent but systematically different estimates.

7.7.3 Detector Modelling and Reconstruction Uncertainties

Detector modelling and reconstruction uncertainties account for Monte Carlo simulation not being a faithful representation of real data as a result of mismodelling of the detector and differential performance of algorithms on simulation compared to data. In this analysis they consist of uncertainties related to jet properties, and uncertainties stemming from the flavour tagging procedure. The background modelling in this analysis is fully data-driven. As a result, these uncertainties are applied only to the signal simulation.

The jet uncertainties are implemented as variations of the jet properties themselves. The category reduction (with ~30 nuisance parameters) is used for jet energy scale uncertainties and the `FullJER` configuration is used for jet energy resolution uncertainties (14 nuisance parameters). This is to preserve the ability to meaningfully statistically combine the results of this analysis with other di-Higgs analyses. The flavour tagging uncertainties meanwhile are implemented as scale factors applied to the Monte Carlo event weights.

A systematic related to the PtReco b-jet energy correction has been studied in the $HH \rightarrow \gamma\gamma b\bar{b}$ analysis [53] and found to be negligible compared to `JER`. Following this example, such a systematic is therefore neglected here.

7.7.4 Trigger Uncertainties

Trigger uncertainties stem from imperfect knowledge of the ratio between the efficiency of a given trigger in data to its efficiency in Monte Carlo simulation. This ratio is applied as a scale factor to all simulated events (as described in Section **??**), with the systematic variations produced by varying the scale factor up or down by one sigma.

7.7.5 Theoretical Uncertainties

The theoretical uncertainties on the acceptance times efficiency ($A \times \varepsilon$) are evaluated by analysis of specially-generated, particle-level signal samples. The generation of these samples follows the configuration of the baseline samples, but with modifications to probe the following theoretical uncertainties: uncertainties in the parton density functions (PDFs); uncertainties due to missing higher order terms in the matrix elements; and uncertainties in the modelling of the underlying event, which includes multi-parton interactions, of hadronic showers and of initial and final state radiation.

Uncertainties due to modelling of the parton shower and the underlying event (including multi-parton interactions) are evaluated by switching the MC generator used. For the scalar samples, this means switching from Herwig7.7.1.3 to Pythia 8.235. Figure **??** shows the impact of these variations on the signal acceptance for two resonance masses: $500\,\mathrm{GeV}$ and

1 TeV, covering the range of the resolved analysis. No significant dependence on the variable of interest, m_{HH}, is observed. The disagreement observed in the tails of $p_T(hh)$ and the number of jets multiplicities is negligible with respect to the final signal acceptance. A 5% flat systematic uncertainty is assigned to all signal samples, extracted from the acceptance comparison for the full 4-tag selection, as seen in Figs. **??** and **??**.

To evaluate the potential effect of missing higher order terms in the matrix element, the renormalization and factorization scales used in the signal generation were varied coherently by factors of $0.5\times$ and $2\times$ for the signals. The alternative weights were generated as described on the TWiki here, applying on-the-fly variations using the ATLAS MadGraphControl framework. These weights correspond to variations of the scales either together or separately up and down by a factor of two. Seven-point scale variations are considered: $(\mu_R, \mu_F) = (0.5, 0.5), (1, 0.5), (0.5, 1), (1, 1), (2, 1), (1, 2), (2, 2)$. The scale uncertainties are combined by taking an envelope of all of the uncertainties. These uncertainties are evaluated to be less than $\pm 1\%$, thus neglected.

PDF uncertainties are evaluated using the PDF4LHC15_nlo_mc set, which combined CT14, MMHT14 and NNPDF3.0 PDF sets. The uncertainty is evaluated by calculating the acceptance for each PDF replica. The standard deviation of these acceptance values divided by the baseline acceptance is taken as the PDF uncertainty. For each mass point the distribution of their corresponding ration is compatible with a Gaussian centered one. The measured uncertainty in acceptance due to PDF uncertainties is less than $\pm 1\%$ across the full mass range considered for the analysis. For this reason, it is neglected in the statistical analysis described in Section **??**.

These uncertainties are implemented in the final statistical analysis as normalization uncertainties on the signals, with the value taken from the polynomial fit. This smooths out statistical fluctuations and allows interpolation between the generated mass points, if needed.

TODO: add non-res ones

7.8   Background Validation

In addition to checking the performance of the background estimate in the control and validation regions, a variety of alternative selections are defined to allow for a full "dress rehearsal" of the background estimation procedure.

Both the resonant and non-resonant analyses make use of a *reversed* $\Delta\eta$ region, in which the kinematic cut on $\Delta\eta_{HH}$ is reversed, so that events are required to have $\Delta\eta_{HH} > 1.5$. This is orthogonal to the nominal signal region and has minimal sensitivity, allowing for the comparison of the background estimate $4b$ data in the corresponding "signal region". For this validation, a new reweighting is trained following nominal procedures, but entirely in the $\Delta\eta_{HH} > 1.5$ region.

The non-resonant analysis additionally makes use of the $3b + 1$ fail region mentioned above, which again is orthogonal to the nominal signal regions and has minimal sensitivity. The reweighting in this case is between $2b$ and $3b + 1$ fail events rather than between $2b$ and $3b + 1$ loose or $2b$ and $4b$. However, the kinematic selections of signal region events are otherwise identical, allowing for a complementary test of the background estimate.

TODO: Add shifted regions if they're ready

Results are shown in *TODO: add figures*

7.9 Overview of Other $b\bar{b}b\bar{b}$ Channels

The results discussed above have been developed in conjunction with (1) a boosted channel for the resonant search and (2) a vector boson fusion (VBF) channel for the non-resonant search. Detailed discussions of these two channels are beyond the scope of this thesis. However, a combined set of results is presented below (*TODO: or will be combined for VBF?*). We therefore briefly summarize the analyses here.

7.9.1 Resonant: Boosted Channel

The boosted analysis selection targets resonance masses from $900\,\mathrm{GeV}$ to $5\,\mathrm{TeV}$. In such events, H decays have a high Lorentz boost, such that the $b\bar{b}$ decays are very collimated. The resolved analysis fails to reconstruct such HH events, as the $R = 0.4$ jets start to overlap.

The boosted analysis instead reconstructs H decays as large radius, $R = 1.0$ jets, with corresponding b-quarks identified with variable radius subjets, that is jets with a radius that scales as ρ/p_T, the p_T is that of the jet in question, and ρ is a fixed parameter, here chosen to be $30\,\mathrm{GeV}$, which is optimized to maintain truth-level double b-labelling efficiency across the full range of Higgs jet p_T *TODO: cite: https://cds.cern.ch/record/2268678*.

Due to limited boosted b-tagging efficiency *TODO: cite* and to maintain sensitivity even when b-jets are highly collimated, the boosted analysis is divided into three categories based on the number of b-tagged jets associated to each large radius jet:

- $4b$ category: two b-tagged jets in each

- $2b - 1$ category: two b-tagged jets in one, one in the other

- $1b - 1$ category: one b-tagged jet in each

The analysis then proceeds in each of these categories. *TODO: what other boosted details?*

The resolved and boosted channels are combined for resonance masses from $900\,\mathrm{GeV}$ to $1.5\,\mathrm{TeV}$ inclusive. To keep the channels statistically independent, the boosted channel vetos

events passing the resolved analysis selection.

7.9.2   Non-resonant: VBF Channel

The vector boson fusion channel is only considered for the non-resonant search. While the sensitivity is in general much more limited than the gluon-gluon fusion analysis due to the much smaller production cross section, VBF is sensitive to a variety of Beyond the Standard Model physics, both complementary and orthogonal to the theoretical scope of gluon-gluon fusion. *TODO: I'll probably mention more details in the pheno section*

The VBF channel proceeds very similarly to the ggF, with the primary differences being the kinematic selections and the categorization.

TODO: fill in kinematics

Note that the background estimation is inherited from the resonant and ggF analyses, an ancillary, but significant, contribution of this thesis work.

7.10 Statistical Analysis

The resonant analysis is used to set a 95% confidence level upper limit on the $pp \to X \to HH \to b\bar{b}b\bar{b}$ and $pp \to G^*_{KK} \to HH \to b\bar{b}b\bar{b}$ cross-sections, while the non-resonant analysis is used to set a 95% confidence level upper limit on the $pp \to HH \to b\bar{b}b\bar{b}$ cross sections for a variety of values of the trilinear Higgs coupling.

The upper limit is extracted using the $\mathrm{CL_s}$ method [54]. The test statistic used is q_μ [55], where μ is the signal strength, and θ represents the nuisance parameters. Due to the use of signals normalized to 1 fb, μ is also the signal cross-section in fb. A single hat represents the maximum likelihood estimate of a parameter, while $\hat{\hat{\theta}}(x)$ represents the conditional maximum likelihood estimate of the nuisance parameters if the signal cross-section is fixed at x.

$$
q_\mu = \begin{cases} -2\ln\left(\dfrac{\mathcal{L}\left(\mu,\hat{\hat{\theta}}(\mu)\right)}{\mathcal{L}\left(\hat{\mu},\hat{\theta}\right)}\right) & \hat{\mu} \le \mu \\ 0 & \hat{\mu} > \mu \end{cases} \tag{7.14}
$$

$\mathrm{CL_s}$ for some test value of μ is then defined by

$$
\mathrm{CL_s} = \frac{\mathrm{CL_{s+b}}}{\mathrm{CL_b}} = \frac{p\left(q_\mu \ge q_{\mu,\,\mathrm{obs}}|s+b\right)}{p\left(q_\mu \ge q_{\mu,\,\mathrm{obs}}|b\right)}, \tag{7.15}
$$

where the p-values are calculated in the asymptotic approximation [55], which is valid in the large sample limit.

The signal cross-section μ fb is excluded at the 95% confidence level if $\mathrm{CL_s} < 0.05$.

7.11   Results

Chapter 8

FUTURE IDEAS FOR $HH \rightarrow b\bar{b}b\bar{b}$

The searches presented in this thesis make use of a large suite of sophisticated techniques, selected through careful study and validation. During this process, a variety of interesting directions for the $HH \rightarrow b\bar{b}b\bar{b}$ analysis were explored by this thesis author, in collaboration with a few others[1], but were not used due to a variety of constraints. We present two such interesting directions here, with the hope of encouraging further exploration of these techniques in future work.

8.1 *pairAGraph: A New Method for Jet Pairing*

As discussed in Chapter 7, one of the main problems to solve is the pairing of b-jets into Higgs candidates. Figure 7.1 demonstrates that the choice of the pairing method, while important for achieving good reconstruction of signal events, also significantly impacts the structure of non-HH events, leading to various biases in the background estimate. Evaluation of the pairing method therefore must take both of these factors into account. While we have presented some advantages in respective contexts for the pairing methods considered here, we of course would like to explore further improvements to this important component of the analysis.

To that end, we note that all of the pairing methods considered here share a common feature: four jets are selected, and the pairing is some discrimination between the available three pairings of these four jets. For the methods used in this analysis, the jet selection proceeds via a simple p_T ordering, with b-tagged jets recieving a higher priority than non-

---

[1]Notably Nicole Hartman (SLAC), who spearheaded much of the development and proof of concept work, in collaboration with Michael Kagan and Rafael Teixeira De Lima.

tagged jets.

With the advent of a variety of machine learning methods for dealing with a variable number of inputs *TODO: cite: RNNs, Deep Sets, GNNs, Transformers*, a natural place to improve on the pairing is to consider more than just four jets. The pairing and jet selection is then performed simultaneously, allowing for the incorporation of more event information in the pairing decision and the incorporation of jet correlation structure in the jet selection.

In practice, the majority of $HH \rightarrow b\bar{b}b\bar{b}$ events have either four or five jets which pass the kinematic preselection, and any gain from this additional freedom would come from events with greater than or equal to five jets. However, this five jet topology is particularly exciting for scenarios such as events with initial state radiation (ISR), in which the $HH->4b$ jets are offset by a single jet with p_T similar in magnitude to that of the $HH->4b$ system. Such events have explicit event level information which is not encoded with the inclusion of only the $HH->4b$ jets, and are pathological if the ISR jet happens to pass b-tagging requirements.

Additionally, with the use of lower tagged regions for background estimation and alternate signal regions, this extra flexibility in jet selection may provide a very useful bias – since the algorithm is trained on signal, the selected jets for the pairing will be the most "4b-like" jets available in the considered set.

For the studies considered here, a transformer *TODO: cite Attention* based architecture is used. This is best visualized by considering the event as a graph with jets corresponding to nodes and edges corresponding to potential connections – for this reason, we term this algorithm "pairAGraph". The approach is as follows: each jet, i, is represented by some vector of input variables, $\vec{x}_i$, in our case the four-vector information, (p_T, η, ϕ, E) of each jet, plus information on the b-tagging decision. A multi-layer perceptron (MLP) is used to create a latent embedding, $\mathbf{h}(\vec{x}_i)$, of this input vector.

To describe the relationship between various jets in the event, we then define a vector $\vec{z}_i$

for each jet as

$$\vec{z}_i = \sum_j w_{ij} \mathbf{h}(\vec{x}_j) \tag{8.1}$$

where j runs over all jets in the event (including $i = j$), the w_{ij} can be thought of as edge weights, and $\mathbf{h}(\vec{x}_j)$ is the latent embedding for jet j mentioned above.

Within this formula, both $\mathbf{h}$ and the w_{ij} are learnable. To learn an appropriate latent mapping and set of edge weights, we define a similarity metric corresponding to each possible jet pairing:

$$\vec{z}_{1a} \cdot \vec{z}_{1b} + \vec{z}_{2a} \cdot \vec{z}_{2b} \tag{8.2}$$

where subscripts $1a$ and $1b$ correspond to the two jets in pair 1, $2a$ and $2b$ to the jets in pair 2 for a given pairing of four distinct jets.

This similarity metric is calculated for all possible pairings, which are then passed through a softmax *TODO: cite* activation function, which compresses these scores to between 0 and 1 with sum of 1, lending an interpretation as probability of each pairing.

In training, the ground truth pairing is set by *truth matching* jets to the b-jets in the HH signal simulation – a jet is considered to match if it is < 0.3 in ΔR away from a b-jet in the simulation record. Given this ground truth, a cross-entropy loss *TODO: cite* is used on the softmax outputs, and w_{ij} and $\mathbf{h}$ are updated correspondingly. Training in such a way corresponds to updating w_{ij} and $\mathbf{h}$ to maximize the similarity metric for the correct pairing.

In evaluation, the pairings with a higher score (and therefore higher softmax output) given the trained h and w_{ij} therefore correspond to the pairings that are most "HH-like". The maximum over these scores is therefore the pairing used as the predicted result from the algorithm.

Because the majority of $HH \rightarrow b\bar{b}b\bar{b}$ events have either four or five jets, it was found to be sufficient to only consider a maximum of 5 jets. Consideration of more is in principle possible, but the quickly expanding combinatorics leads to a rapidly more difficult problem. The jets considered are the five leading jets in p_T. Notably, this set of jets may include jets which are not b-tagged, even for the nominal $4b$ region – therefore events with 4 b-jets are

not required to use all of them in the construction of Higgs candidates, in contrast to the other algorithms used in this thesis.

8.2 Background Estimation with Mass Plane Interpolation

The choice of a pairing algorithm that results in a smooth mass plane (such as $\min \Delta R$) opens up a variety of options for the background estimation. While the method based on reweighting of $2b$ events used for this thesis performs well and has been extensively studied and validated, it also relies on several assumptions. In particular, the reweighting is derived between e.g., $2b$ and $4b$ events *outside* of the signal region and then applied to $2b$ events *inside* the signal region, with the assumption that the $2b$ to $4b$ transfer function will be sufficiently similar in both regions of the mass plane. An uncertainty is assigned to account for the bias due to this assumption, but the extrapolation in the mass plane is never explicitly treated in the nominal estimate. While the approach of reweighting $2b$ events within the signal region does have the advantage of incorporating explicit signal region information (that is, the $2b$ signal region events), the importance of the extrapolation bias motivates consideration of a method that operates within the $4b$ mass plane. This additionally removes the reliance on lower b-tagging regions, allowing for the use of, e.g. $3b$ triggers, and future-proofing the analysis against trigger bandwidth constraints in the low tag regions.

The method considered here relies on the following: for a given vector of input variables (event kinematics, etc), $\vec{x}$, the joint probability in the HH mass plane may be written as:

$$p(\vec{x}, m_{H1}, m_{H2}) = p(\vec{x}|m_{H1}, m_{H2})p(m_{H1}, m_{H2}) \tag{8.3}$$

by the chain rule of probability. This means that the full dynamics of events in the HH mass plane may be described by (1) the conditional probability of considered variables $\vec{x}$, given values of m_{H1} and m_{H2}, and (2) the density of the mass plane itself.

We present here an approach which uses normalizing flows *TODO: cite* to model the conditional probabilities of events in the mass plane and Gaussian processes to model the mass plane density. These models are trained in a region around, but not including, the

signal region, and the trained models are then used to construct an *interpolated* estimate of the signal region kinematics. This approach therefore explicitly treats event behavior within the mass plane, avoiding the concerns associated with a reweighted estimate. Validation of such a method, as well as assessing of closure and biases of the method, may be done in alternate b-tagging or kinematic regions, notably the now unused $2b$ region, results of which are shown below.

8.2.1 *Normalizing Flows*

Normalizing flows model observed data $x \in X$, with $x \sim p_X$, as the output of an invertible, differentiable function $f : X \to Z$, with $z \in Z$ a latent variable with a simple prior probability distribution (often standard normal), $z \sim p_Z$. From a change of variables, given such a function, we may write

$$p_X(x) = p_Z(f(x)) \left| \det \left(\frac{d(f(x))}{dx} \right) \right| \tag{8.4}$$

where $\left(\frac{d(f(x))}{dx} \right)$ is the Jacobian of f at x.

The problem of normalizing flows then reduces to (1) choosing sets of f which are both tractable and sufficiently expressive to describe observed data, and (2) optimizing associated sets of functional parameters on observed data via maximum likelihood esitmation using the above formula. Sampling from the learned density is done by drawing from the latent distribution $z \sim p_Z$ (cf. inverse transform sampling) – the corresponding sample is then $x \sim p_X$ with $x = f^{-1}(z)$.

A standard approach to the definition of these f is as a composition of affine transformations (e.g. RealNVP *TODO: cite*), that is, transformations of the form $\alpha z + \beta$, with α and β learnable parameter vectors. This can roughly be though of as shifting and squeezing the input input prior density in order to match the data densitiy. However, this has somewhat limited expressivity, for instance in the case of a multi-modal density.

This work thus instead relies on neural spline flows *TODO: cite: https://arxiv.org/pdf/1906.04032.pdf* in which the functions considered are monotonic rational-quadratic splines, which have an

analytic inverse. A rational quadratic function has the form of a quotient of two quadratic polynomials, namely,

$$f_j(x_i) = \frac{a_{ij}x_i^2 + b_{ij}x_{ij} + c_{ij}}{d_{ij}x_i^2 + e_{ij}x_i + f_{ij}} \tag{8.5}$$

with six associated parameters (a_{ij} through f_{ij}) per each piecewise bin j of the spline and each input dimension i. This is explicitly more flexible and expressive than a simple affine transformation, allowing, e.g., the treatment of multi-modality via the piecewise nature of the spline.

The rational quadratic spline is defined on an set interval. The transformation outside of this interval is set to the identity, with these linear tails allowing for unconstrained inputs. The boundaries between bins of the spline are set by coordinates scalled *knots*, with $K + 1$ knots for K bins – the two endpoints for the spline interval plus the $K - 1$ internal boundaries. The derivatives at these points are constrained to be positive for the internal knots, and boundary derivatives are set to 1 to match the linear tails.

The bin widths and heights are learnable ($2 \cdot K$ parameters) as are the internal knot derivatives ($K - 1$ parameters), and these $3K - 1$ ouputs of the neural network are sufficient to define a monotonic rational-quadratic spline which passes through each knot and has the given derivative value at each knot.

In the context of the $HH \to 4b$ analysis, a neural spline flow is used to model the four vector information of each Higgs candidate, conditional on their respective masses. The resulting flow is therefore five dimensional, with inputs $x = (p_{T,H1}, p_{T,H2}, \eta_{H1}, \eta_{H2}, \Delta\phi_{HH})$, where the ATLAS ϕ symmetry has been encdoded by assuming $\phi_{H1} = 0$. Conditional variables m_{H1} and m_{H2} are not modeled by the flow, but "come along for the ride". A standard normal distribution in 5 dimensions is used for the underlying prior. Modeling of the four vectors was chosen in order to reduce bias from modeling m_{HH} directly.

The trained flow model then gives a model for $p(x|m_{H1}, m_{H2})$ which may be sampled from to reconstruct distributions of HH kinematics given values of m_{H1} and m_{H2}.

8.2.2 Gaussian Processes

The second piece of this background estimate is the modeling of the mass plane density, $p(m_{H1}, m_{H2})$. This is done using Gaussian process regression – note that a similar procedure is used to define a systematic in the boosted $4b$ analysis. Generally, Gaussian processes are a collection of random variables in which every finite collection of said variables is distributed according to a multivariate normal distribution. For the context of Gaussian process regression, what we consider is a Gaussian process over function space, that is, for a collection of points, $x_1, \ldots, x_N$, the space of corresponding function values, $(f(x_1), \ldots, f(x_N))$ is Gaussian process distributed, that is, described by an N dimensional normal distribution with mean μ, covariance matrix Σ.

For a single point, this would correspond to a function space described entirely by a normal distribution, with various samples from that distribution yielding various candidate functions. For multiple points, a covariance matrix describes the relationship between each pair of points – correspondingly, it is represented via a *kernel function*, $K(x, x')$. As, in practice, μ may always be set to 0 via a centering of the data, the kernel function fully defines the considered family of functions.

The considered family of functions describes a Bayesian *prior* for the data. This prior may be conditioned on a set of training data points $(X_1, \vec{y}_1)$. This conditional *posterior* may then be used to make predictions $\vec{y}_2 = f(X_2)$ at a set of new points X_2. Because of the Gaussian process prior assumption, $\vec{y}_1$ and $\vec{y}_2$ are assumed to be jointly Gaussian. We may therefore write

$$\begin{pmatrix} \vec{y}_1 \\ \vec{y}_2 \end{pmatrix} \sim \mathcal{N} \left(\begin{pmatrix} 0 \\ 0 \end{pmatrix}, \begin{pmatrix} K(X_1, X_1) & K(X_1, X_2) \\ K(X_1, X_2) & K(X_2, X_2) \end{pmatrix} \right) \tag{8.6}$$

where we have used that the kernel function is symmetric and assumed prior mean 0.

By standard conditioning properties of Gaussian distributions,

$$\vec{y}_2 | \vec{y}_1 \sim \mathcal{N}(K(X_2, X_1)K(X_1, X_1)^{-1}\vec{y}_1, K(X_2, X_2) - K(X_2, X_1)K(X_1, X_1)^{-1}K(X_1, X_2)) \tag{8.7}$$

which is the sampling distribution for a Gaussian process given kernel K. In practice, the mean of this sampling distribution is used as the function estimate, with an uncertainty from the predicted variance at a given point.

The choice of kernel function has a very strong impact on the fitted curve, and must therefore be chosen to express the expected dynamics of the data. A common such choice is a radial basis function (RBF) kernel, which takes the form

$$K(x, x') = \exp\left(-\frac{d(x, x')^2}{2l^2}\right) \tag{8.8}$$

where $d(\cdot, \cdot)$ is the Euclidean distance and $l > 0$ is a length scale parameter. Conceptually, as distances $d(x, x')$ increase relative to the chosen length scale, the kernel smoothly dies off – further away points influence each other less.

Coming back to our case of the mass plane, the procedure runs as follows:

1. A binned 2d histogram of the blinded mass plane is created in a window around the "standard" analysis regions. Bins which have any overlap with the signal region are excluded.

2. A Gaussian process is trained using the bin centers, values as training points. The scikit-learn *TODO: cite* implementation is used, with RBF kernel with anisotropic length scale (l is dimension 2). The length scale is initialized to $(50, 50)$ to cover the signal region, and optimized by minimizing the negative log-marginal likelihood on the training data, $-\log p(\vec{y}|\theta)$. Training data is centered and scaled to mean 0, variance 1, and a statistical error is included in the fit.

3. The Gaussian process is then used to predict the density $p(m_{H1}, m_{H2})$ in the signal region. This may then be sampled from via an inverse transform sampling to generate values (m_{H1}, m_{H2}) according to the density (specifically, according to the mean of the Gaussian process posterior). Though in principle the Gaussian process sampling is not limited to bin centers, this is kept for simplicity, with a uniform smearing applied within

each sampled bin to approximate the contiuous estimate, namely, if a bin is sampled from, the returned value is drawn uniformly at random within the sampled bin.

4. The sampling in the previous step can be arbitrary – to set the overall normalization, a Monte Carlo sampling of the Gaussian process is done to approximate the relative fraction of events predicted both inside (f_{in}) and outside (f_{out}) of the signal region, within the training box. The number of events outside of the signal region (n_{out}) is known, therefore, the number of events inside of the signal region, n_{in}, may be estimated as

$$n_{in} = \frac{n_{out}}{f_{out}} \cdot f_{in}. \tag{8.9}$$

Note that the Monte Carlo sampling procedure is simply a set of samples of the Gaussian process from uniformly random values of m_{H1}, m_{H2}, and is the most convenient approach given the irregular shape of the signal region.

This procedure results in a generated set of predicted m_{H1}, m_{H2} values for signal region, background events, along with an overall yield prediction.

8.2.3   The Full Prediction

Given the normalizing flow parametrization of $p(x|m_{H1}, m_{H2})$ and the Gaussian process generation of $(m_{H1}, m_{H2}) \sim p(m_{H1}, m_{H2})$ and prediction of the signal region yield, all of the pieces are in place to construct an interpolation background estimate. Namely

1. Gaussian process sampled (m_{H1}, m_{H2}) values are provided to the normalizing flow to predict the other variables for the Higgs candidate four-vectors. These are used to construct the HH system (notably $m_{HH}, \cos \theta^*$).

2. These final distributions are normalized according to the predicted background yield.

8.2.4   Outstanding Points

While good performance is demonstrated from the nominal interpolated background estimate, various uncertainties must be assigned according to the various stages of the estimate. These notably include

- Assessing a statistical uncertainty on the normalizing flow training (cf. bootstrap uncertainty).

- Propagation of the Gaussian process uncertainty through the sampling procedure.

- Validation of the resulting estimate and assessment of necessary systematic uncertainties (e.g. from validation region non-closure).

These are all quite tractable, but some, especially the choice of an appropriate systematic uncertainty, are certainly not obvious and require detailed study. In this respect, the reweighting validation work of the non-resonant analysis is certainly quite useful as a starting place in terms of the available regions and their correspondence to the nominal $4b$ signal region.

BIBLIOGRAPHY

[1] K. Agashe, H. Davoudiasl, G. Perez, and A. Soni, *Warped gravitons at the CERN LHC and beyond*, Phys. Rev. D **76** (3 2007) 036006, URL: https://link.aps.org/doi/10.1103/PhysRevD.76.036006 (cit. on p. 25).

[2] G. Branco et al., *Theory and phenomenology of two-Higgs-doublet models*, Physics Reports **516** (2012) 1, Theory and phenomenology of two-Higgs-doublet models, ISSN: 0370-1573, URL: http://www.sciencedirect.com/science/article/pii/S0370157312000695 (cit. on p. 25).

[3] J. Pequenao, "Computer generated image of the whole ATLAS detector", 2008, URL: https://cds.cern.ch/record/1095924 (cit. on p. 29).

[4] ATLAS Collaboration, *The ATLAS Experiment at the CERN Large Hadron Collider*, JINST **3** (2008) S08003 (cit. on p. 30).

[5] J. Pequenao and P. Schaffner, "How ATLAS detects particles: diagram of particle paths in the detector", 2013, URL: https://cds.cern.ch/record/1505342 (cit. on p. 31).

[6] ATLAS Collaboration, *ATLAS Insertable B-Layer: Technical Design Report*, ATLAS-TDR-19; CERN-LHCC-2010-013, 2010, URL: https://cds.cern.ch/record/1291633 (cit. on p. 30), Addendum: ATLAS-TDR-19-ADD-1; CERN-LHCC-2012-009, 2012, URL: https://cds.cern.ch/record/1451888.

[7] B. Abbott et al., *Production and integration of the ATLAS Insertable B-Layer*, JINST **13** (2018) T05008, arXiv: 1803.00844 [physics.ins-det] (cit. on p. 30).

[8] ATLAS Collaboration, *Performance of the ATLAS trigger system in 2015*, Eur. Phys. J. C **77** (2017) 317, arXiv: 1611.09661 [hep-ex] (cit. on p. 32).

[9] ATLAS Collaboration, *The ATLAS Collaboration Software and Firmware*, ATL-SOFT-PUB-2021-001, 2021, URL: https://cds.cern.ch/record/2767187 (cit. on p. 32).

[10] J. Alwall et al., *The automated computation of tree-level and next-to-leading order differential cross sections, and their matching to parton shower simulations*, Journal of High Energy Physics **2014** (2014), URL: https://doi.org/10.1007/jhep07(2014)079 (cit. on pp. 33, 60).

[11] P. Nason, *A New method for combining NLO QCD with shower Monte Carlo algorithms*, JHEP **11** (2004) 040, arXiv: hep-ph/0409146 [hep-ph] (cit. on pp. 34, 61).

[12] S. Frixione, P. Nason and C. Oleari, *Matching NLO QCD computations with parton shower simulations: the POWHEG method*, JHEP **11** (2007) 070, arXiv: 0709.2092 [hep-ph] (cit. on pp. 34, 61).

[13] S. Alioli, P. Nason, C. Oleari, and E. Re, *A general framework for implementing NLO calculations in shower Monte Carlo programs: the POWHEG BOX*, JHEP **06** (2010) 043, arXiv: 1002.2581 [hep-ph] (cit. on pp. 34, 61).

[14] J. Bellm et al., *Herwig 7.0/Herwig++ 3.0 release note*, The European Physical Journal C **76** (2016), URL: https://doi.org/10.1140/epjc/s10052-016-4018-8 (cit. on pp. 34, 60).

[15] M. Bähr et al., *Herwig++ physics and manual*, The European Physical Journal C **58** (2008) 639, URL: https://doi.org/10.1140/epjc/s10052-008-0798-9 (cit. on pp. 34, 60).

[16] T. Sjöstrand et al., *An introduction to PYTHIA 8.2*, Computer Physics Communications **191** (2015) 159, ISSN: 0010-4655, URL: https://www.sciencedirect.com/science/article/pii/S0010465515000442 (cit. on pp. 34, 60).

[17] D. J. Lange, *The EvtGen particle decay simulation package*, Nucl. Instrum. Meth. A **462** (2001) 152 (cit. on pp. 34, 60).

[18] S. Agostinelli et al., *Geant4—a simulation toolkit*, Nuclear Instruments and Methods in Physics Research Section A: Accelerators, Spectrometers, Detectors and Associated Equipment **506** (2003) 250, ISSN: 0168-9002, URL: https://www.sciencedirect.com/science/article/pii/S0168900203013688 (cit. on p. 35).

[19] ATLAS Collaboration, *The ATLAS Simulation Infrastructure*, Eur. Phys. J. C **70** (2010) 823, arXiv: 1005.4568 [physics.ins-det] (cit. on pp. 35, 60).

[20] ATLAS Collaboration, *The new Fast Calorimeter Simulation in ATLAS*, ATL-SOFT-PUB-2018-002, 2018, URL: https://cds.cern.ch/record/2630434 (cit. on pp. 36, 37).

[21] M. Aharrouche et al., *Energy linearity and resolution of the ATLAS electromagnetic barrel calorimeter in an electron test-beam*, Nuclear Instruments and Methods in Physics Research Section A: Accelerators, Spectrometers, Detectors and Associated Equipment **568** (2006) 601, ISSN: 0168-9002, URL: http://dx.doi.org/10.1016/j.nima.2006.07.053 (cit. on p. 37).

[22] ATLAS Collaboration, *Evidence for prompt photon production in pp collisions at $\sqrt{s} = 7$ TeV with the ATLAS detector*, ATLAS-CONF-2010-077, 2010, URL: https://cds.cern.ch/record/1281368 (cit. on p. 37).

[23] D. P. Kingma and M. Welling, *Auto-Encoding Variational Bayes*, 2014, arXiv: 1312.6114 [stat.ML] (cit. on p. 38).

[24] ATLAS Collaboration, *Jet reconstruction and performance using particle flow with the ATLAS Detector*, Eur. Phys. J. C **77** (2017) 466, arXiv: 1703.10485 [hep-ex] (cit. on pp. 45, 59).

[25] ATLAS Collaboration, *Topological cell clustering in the ATLAS calorimeters and its performance in LHC Run 1*, Eur. Phys. J. C **77** (2017) 490, arXiv: 1603.02934 [hep-ex] (cit. on p. 45).

[26] ATLAS Collaboration, *Variable Radius, Exclusive-k_T, and Center-of-Mass Subjet Reconstruction for Higgs($\to b\bar{b}$) Tagging in ATLAS*, ATL-PHYS-PUB-2017-010, 2017, URL: https://cds.cern.ch/record/2268678 (cit. on p. 45).

[27] M. Cacciari, G. P. Salam, and G. Soyez, *The anti-kt jet clustering algorithm*, Journal of High Energy Physics **2008** (2008) 063, ISSN: 1029-8479, URL: http://dx.doi.org/10.1088/1126-6708/2008/04/063 (cit. on p. 45).

[28] G. P. Salam, *Towards jetography*, The European Physical Journal C **67** (2010) 637, ISSN: 1434-6052, URL: http://dx.doi.org/10.1140/epjc/s10052-010-1314-6 (cit. on p. 45).

[29] A. Collaboration, *Configuration and performance of the ATLAS b-jet triggers in Run 2*, 2021, arXiv: 2106.03584 [hep-ex] (cit. on p. 49).

[30] ATLAS Collaboration, *ATLAS b-jet identification performance and efficiency measurement with $t\bar{t}$ events in pp collisions at $\sqrt{s} = 13\,TeV$*, Eur. Phys. J. C **79** (2019) 970, arXiv: 1907.05120 [hep-ex] (cit. on pp. 48, 59).

[31] ATLAS Collaboration, *Topological b-hadron decay reconstruction and identification of b-jets with the JetFitter package in the ATLAS experiment at the LHC*, ATL-PHYS-PUB-2018-025, 2018, URL: https://cds.cern.ch/record/2645405 (cit. on p. 51).

[32] R. Frühwirth, *Application of Kalman filtering to track and vertex fitting*, Nuclear Instruments and Methods in Physics Research Section A: Accelerators, Spectrometers, Detectors and Associated Equipment **262** (1987) 444, ISSN: 0168-9002, URL: https://www.sciencedirect.com/science/article/pii/0168900287908874 (cit. on p. 51).

[33] ATLAS Collaboration, *Identification of Jets Containing b-Hadrons with Recurrent Neural Networks at the ATLAS Experiment*, ATL-PHYS-PUB-2017-003, 2017, URL: https://cds.cern.ch/record/2255226 (cit. on p. 52).

[34] *Expected performance of the 2019 ATLAS b-taggers*, http://atlas.web.cern.ch/Atlas/GROUPS/PHYSICS/PLOTS/FTAG-2019-005/, Accessed: 2021-07-14 (cit. on p. 54).

[35] ATLAS Collaboration, *Search for Higgs boson pair production in the $b\bar{b}WW^*$ decay mode at $\sqrt{s} = 13\,TeV$ with the ATLAS detector*, JHEP **04** (2019) 092, arXiv: 1811.04671 [hep-ex] (cit. on p. 58).

[36] ATLAS Collaboration, *A search for resonant and non-resonant Higgs boson pair production in the $b\bar{b}\tau^+\tau^-$ decay channel in pp collisions at $\sqrt{s} = 13\,TeV$ with the ATLAS detector*, Phys. Rev. Lett. **121** (2018) 191801, arXiv: 1808.00336 [hep-ex] (cit. on p. 58), Erratum: Phys. Rev. Lett. **122** (2019) 089901.

[37] ATLAS Collaboration, *Search for Higgs boson pair production in the $WW^{(*)}WW^{(*)}$ decay channel using ATLAS data recorded at $\sqrt{s} = 13\,TeV$*, JHEP **05** (2019) 124, arXiv: 1811.11028 [hep-ex] (cit. on p. 58).

[38] ATLAS Collaboration, *Search for Higgs boson pair production in the $\gamma\gamma b\bar{b}$ final state with $13\,TeV$ pp collision data collected by the ATLAS experiment*, JHEP **11** (2018) 040, arXiv: 1807.04873 [hep-ex] (cit. on p. 58).

[39] ATLAS Collaboration, *Search for Higgs boson pair production in the $\gamma\gamma WW^*$ channel using pp collision data recorded at $\sqrt{s} = 13\,TeV$ with the ATLAS detector*, Eur. Phys. J. C **78** (2018) 1007, arXiv: 1807.08567 [hep-ex] (cit. on p. 58).

[40] ATLAS Collaboration, *Combination of searches for Higgs boson pairs in pp collisions at $\sqrt{s} = 13\,TeV$ with the ATLAS detector*, Phys. Lett. B **800** (2020) 135103, arXiv: 1906.02025 [hep-ex] (cit. on p. 58).

[41] CMS Collaboration, *Search for heavy resonances decaying to two Higgs bosons in final states containing four b quarks*, Eur. Phys. J. C **76** (2016) 371, arXiv: 1602.08762 [hep-ex] (cit. on p. 58).

[42] CMS Collaboration, *Search for production of Higgs boson pairs in the four b quark final state using large-area jets in proton–proton collisions at $\sqrt{s} = 13\,TeV$*, JHEP **01** (2019) 040, arXiv: `1808.01473 [hep-ex]` (cit. on p. 58).

[43] CMS Collaboration, *Combination of Searches for Higgs Boson Pair Production in Proton–Proton Collisions at $\sqrt{s} = 13\,TeV$*, Phys. Rev. Lett. **122** (2019) 121803, arXiv: `1811.09689 [hep-ex]` (cit. on p. 59).

[44] G. Bartolini et al., *Performance of the ATLAS b-jet trigger in p p collisions at $\sqrt{s} = 13\,TeV$*, tech. rep. ATL-COM-DAQ-2019-150, CERN, 2019, URL: `https://cds.cern.ch/record/2688819` (cit. on p. 59).

[45] ATLAS Collaboration, *Luminosity determination in pp collisions at $\sqrt{s} = 13\,TeV$ using the ATLAS detector at the LHC*, ATLAS-CONF-2019-021, 2019, URL: `https://cds.cern.ch/record/2677054` (cit. on p. 60).

[46] J. Butterworth et al., *PDF4LHC recommendations for LHC Run II*, J. Phys. G **43** (2016) 023001, arXiv: `1510.03865 [hep-ph]` (cit. on p. 61).

[47] M. Bahr et al., *Herwig++ Physics and Manual*, Eur. Phys. J. **C58** (2008) 639, arXiv: `0803.0883 [hep-ph]` (cit. on p. 61).

[48] T. Head et al., *scikit-optimize/scikit-optimize: v0.5.2*, version v0.5.2, 2018, URL: `https://doi.org/10.5281/zenodo.1207017` (cit. on p. 65).

[49] G. V. Moustakides and K. Basioti, *Training Neural Networks for Likelihood/Density Ratio Estimation*, 2019, arXiv: `1911.00405 [eess.SP]` (cit. on p. 76).

[50] T. Kanamori, S. Hido, and M. Sugiyama, *A Least-Squares Approach to Direct Importance Estimation*, J. Mach. Learn. Res. **10** (2009) 1391, ISSN: 1532-4435 (cit. on p. 76).

[51] S. Fort, H. Hu, and B. Lakshminarayanan, *Deep Ensembles: A Loss Landscape Perspective*, 2020, arXiv: `1912.02757 [stat.ML]` (cit. on p. 78).

[52] B. Efron, *Bootstrap Methods: Another Look at the Jackknife*, Ann. Statist. **7** (1979) 1, URL: `https://doi.org/10.1214/aos/1176344552` (cit. on p. 81).

[53] J. Adelman et al., *Search for Higgs boson pair production in the $b\bar{b}\gamma\gamma$ final state with the full Run 2 13 TeV pp collision data collected by the ATLAS Experiment Supporting note.*, tech. rep., CERN, 2020, URL: https://cds.cern.ch/record/2711865 (cit. on p. 86).

[54] A. L. Read, *Presentation of search results: the CLs technique*, Journal of Physics G: Nuclear and Particle Physics **28** (2002) 2693, ISSN: 0954-3899 (cit. on p. 91).

[55] G. Cowan, K. Cranmer, E. Gross, and O. Vitells, *Asymptotic formulae for likelihood-based tests of new physics*, The European Physical Journal C **71** (2011), ISSN: 1434-6052 (cit. on p. 91).